DNA Dynamics during Electrophoreis in Microfabricated Post Arrays

A DISSERTATION
SUBMITTED TO THE FACULTY OF THE GRADUATE SCHOOL
OF THE UNIVERSITY OF MINNESOTA
BY

Daniel Wayne Olson

IN PARTIAL FULFILLMENT OF THE REQUIREMENTS
FOR THE DEGREE OF
DOCTOR OF PHILOSOPHY

Kevin D. Dorfman

September 2012

Acknowledgements

I would like to thank my advisor, Kevin Dorfman, for giving me the opportunity to work in his lab and for teaching me how to succeed in scientific research.

I am grateful to the members of the Dorfman research group: Nabil Laachi, Maggie Linak, Noritoshi Araki, Joel Thomas, Scott King, Doug Tree, Sarit Dutta, Abhiram Muralidhar, Mark Joswiak, Barry Badeau, Mingwei Tian, Julian Sheats, Zhicheng Long, Sung-Gyu Park, Martin Kenward, Jaeseol Cho, and especially Jia Ou who mentored me when I first joined the group.

I am also grateful for the support I have received from my family and friends.

Financial support was provided by the National Science Foundation (Grant No. CBET-0642794), the David and Lucile Packard Foundation, a Dreyfus New Faculty Award, and the National Institute of Health (Grant 1R01 HG005216). Much of the device fabrication and characterization was performed in the University of Minnesota Nanofabrication Center, which receives partial support from the National Science Foundation though the National Nanotechnology Infrastructure Network, and in the Institute of Technology Characterization Facility, University of Minnesota, a member of the National Science Foundation funded Materials Research Facilities Network (www.mrfn.org).

Contents

List of Tables

List of Figures

Statement of the Author's Contributions

Much of the research presented here has already been published in peer reviewed journals. Because many of the journal articles list multiple authors, I would like to state my specific contributions to the research.

Portions of Chapter 2 will appear in section 6.1.1 of "Beyond gel electrophoresis: Microfluidic separations, fluorescence burst analysis, and DNA stretching," K. D. Dorfman, S. B. King, D. W. Olson, J. D. P. Thomas, and D. R. Tree; which is awaiting publication in *Chemical Reviews*. I wrote this section of the review paper.

Chapter 3 is based on "DNA electrophoresis in a sparse ordered post array," J. Ou, J. Cho, D. W. Olson, and K. D. Dorfman; *Physical Review E* **79** (2009) 061904. For this publication, I fabricated microfluidic devices and performed electrophoresis experiments with Jia Ou. I also wrote Matlab code to calculate electrophoretic mobility and dispersion coefficient from the experimental data.

Chapter 4 is based on "Continuous Time Random Walk Models of DNA Electrophoresis in a Post Array: I. Evaluation of Existing Models," D. W. Olson, J. Ou, M. Tian, and K. D. Dorfman; *Electrophoresis* **32** (2011) 573-580. Part one of this two part series involves experiments on the dynamics of DNA in micropost arrays. I performed the experiments and extracted relevant data from them. I supervised an undergraduate, Minwei Tian, who applied my data analysis method to Brownian dynamics simulation data.

Chapter 5 is based on "Continuous Time Random Walk Models of DNA Electrophoresis in a Post Array: II. Mobility and Sources of Band Broadening," D. W. Olson, S. Dutta, N. Laachi, M. Tian, and K. D. Dorfman; *Electrophoresis* **32** (2011) 581-587. In part two, we proposed a model for DNA transport and analyzed a large amount of simulation data. I developed the transport model along with Nabil Laachi. I chose the simulations pa-

rameters and analyzed the results using the data analysis method from part one.

Chapter 6 is based on "DNA Electrophoresis in a Nanofence Array," S.-G. Park, D. W. Olson, and K. D. Dorfman; *Lab on a chip* **12** (2012) 1463-1470. The Nanofence is a prototype device with promise to improve DNA separation. For this publication, I assisted Sung-Gyu Park in performing the single molecule observations. I then analyzed the single molecule data in the context of the two state transport model.

Chapter 7 is based on "Experimental study of the effect of disorder on DNA dynamics in post arrays during electrophoresis," D. W. Olson and K. D. Dorfman; which has been accepted by *Phys. Rev. E*. I designed and fabricated the experimental devices used in this project. I performed all experiments and analysis.

Chapter 1

Introduction

Electrophoretic separation of DNA is important in many areas of science and medicine. While the separation of short DNA molecules is fast and inexpensive, there is still room for improving the separation of long DNA. Many new methods relying on microfabrication have emerged that are able to separate long DNA molecules orders of magnitude faster than traditional methods. One of the more promising methods utilizes arrays of posts with diameters in the micrometer to nanometer range. The research described here explores the interaction of DNA molecules with the micofabricated post array geometry through single molecule videomicroscopy experiments. Information gathered from these experiments guides simulation methodology and ultimately leads to very good agreement between experiments and simulation of DNA transport in microfabricated post arrays. A new theoretical model is proposed that accurately predicts bulk transport properties from the micro-scale physics of the DNA-post array interactions. Analysis of this new model led to the design of a new post array separation device, the nanofence, whose separation properties are discussed in in the context of the proposed theoretical model.

1.1 DNA Mapping and Sequencing

Deoxyribonucleic acid (DNA) is a polymer that contains genetic information. DNA consists of a phosphate group attached to deoxyribose and one of four nucleotide bases: adenine, cytosine, guanine, or thymine. A single strand of these bases attaches to a second complementary strand by hydrogen bonding to form the familiar double stranded DNA double helix. Genome sequencing is the process by which the order of these base pairs is identified. The completion of the human genome project opened up many possibilities for DNA sequencing in medicine [1]. Genes and other genetic markers can indicate a predisposition to certain diseases, or give doctors a clue to a specific patient's drug response.

Sequencing currently has many applications including forensics, genealogy, medical diagnosis, and biotechnology research. Most DNA size separation required during Sanger sequencing involves relatively short ($<$1000 base pair) single stranded DNA. However, separation of long double stranded DNA is required for restriction mapping. Figure 1.1 shows the restriction mapping process. Because restriction enzymes cut DNA only at specific sequences, a restriction map provides information about the number of cleavage sites and their location. This information is useful in determining the order of the randomly placed, sequenced $\sim$700 bp regions resulting from Sanger sequencing.

Restriction mapping is also a simple and cost-effective method for disease screening [2] compared to whole-genome sequencing. Scientists can culture an unknown pathogen, then extract its DNA. After cutting the DNA with a restriction enzyme, the results of a size separation (Fig. 1.1) can be compared to known restriction maps. The Centers for Disease Control and Prevention maintains a database of the restriction maps for many known pathogens. This process, which relies on long DNA separation, rapidly identifies biolog-

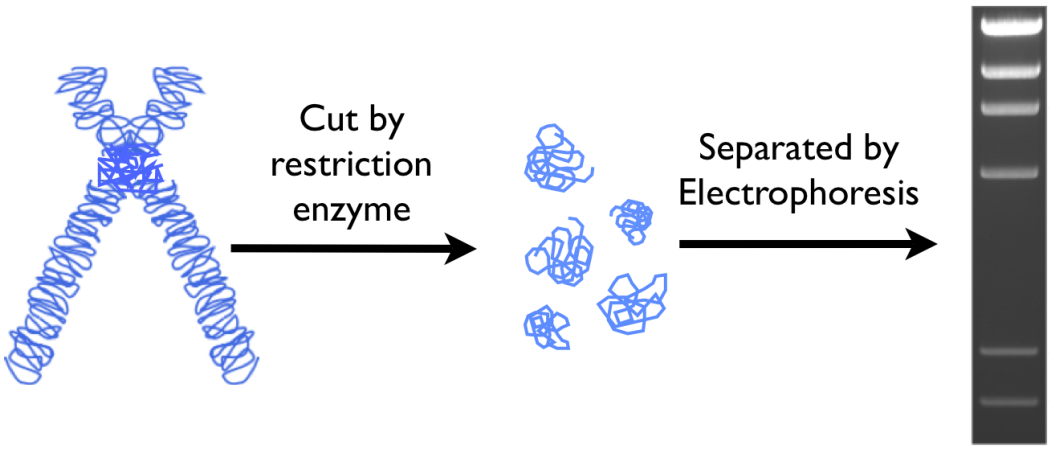

Figure 1.1: Schematic of the restriction mapping process. A chromosome is cut by one or more restriction enzymes. The smaller strands of DNA that result make up a restriction map of the chromosome.

ical threats to human well-being. Restriction maps are also very important for analyzing eukaryotic genomes, which contain areas that are difficult to sequence by DNA strand extension.

1.2 Electrophoresis of DNA

In addition to the utility of long DNA size separation, the dynamics of these large biopolymers is an interesting fundamental problem. DNA is a model polymer for studying polymer dynamics [3]. DNA is suited to single molecule microscopy studies because (i) it is large enough to be imaged by optical microscopy; (ii) there are several very bright DNA dyes; and (iii) its small diffusion coefficient allows video frame rates. DNA is separated in solution by the application of an external electric field in a process called electrophoresis. The following discussion of DNA as a polymer and of electrophoresis is primarily based on the book *Polymer Chemistry* [4] and a review article by J. L. Viovy [3].

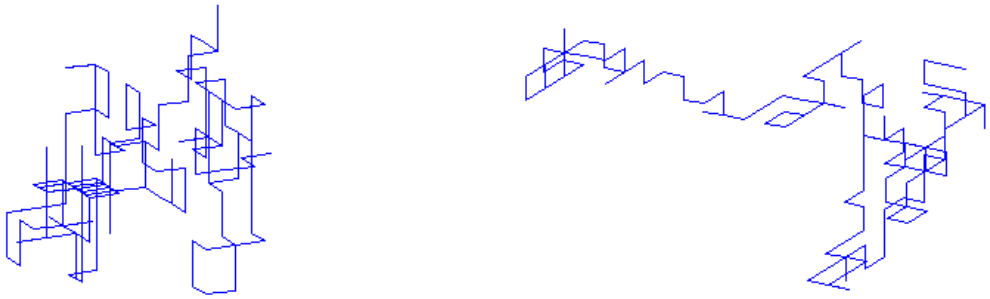

Figure 1.2: Two random walks of $N_k = 160$ steps on a three dimensional lattice. λ DNA is ∼160 Kuhn steps long and has 48500 base pairs.

1.2.1 DNA in solution

Small DNA in a good solvent behaves as a random walk with end to end distance $R = l_k N_k^{1/2}$, where l_k is the Kuhn length of double stranded DNA (dsDNA) and N_k is the number of Kuhn lengths. The DNA molecule behaves as a random walk of N_k steps. Kuhn length is dependent on the solution conditions; for typical DNA buffer solutions $l_k \approx 120$ nm.

The random walk model breaks down for longer DNA because the molecule cannot fold back upon itself. The excluded volume of the DNA increases the size of the molecule. The end to end distance of an excluded volume chain (R_v) in an athermal solvent is

$$R_v = \frac{l_k^2}{d}\left(\frac{N_k}{N_v}\right)^v . \tag{1.1}$$

In Eq. 1.1 d is the diameter of the Kuhn segment, N_v is the size of the polymer where excluded volume effects become important (∼10 kilobase pairs for dsDNA [3]), and v is the Flory exponent (approximately 3/5). In addition to the end to end distance, another useful measure of the size of a polymer is the radius of gyration, $R_g = R_v/\sqrt{6}$. The radius of gyration is the root mean squared distance from the center of mass of the polymer to

its monomers.

In solution, DNA dissociates into a large negatively charged macroion and counterions, as shown in Fig. 1.3. The phosphate backbone of the DNA molecule carries negative charges. Charges interact strongly over the Bjeruum length (l_B). Beyond this length thermal forces dominate electrostatic interactions. Bjeruum length is defined as

$$l_B = \frac{e^2}{4\pi\epsilon_0\epsilon k_B T}, \tag{1.2}$$

and has a value of 0.7 nm in water at room temperature. Electrostatics lead to a layer of counterions permanently adsorbed to the surface of the DNA polyelectrolyte. This layer is called the Stern layer and its thickness is roughly given by the Bjeruum length (l_B) in Eq. 1.2 [3]. Outside of the Stern layer, counterions are attracted to the polyelectrolyte strongly enough to cause a higher concentration of counterions than coions. This layer of charges is the Debye layer. The length of the Debye layer (κ^{-1}) is

$$\kappa^{-1} = \sqrt{\frac{\epsilon_0\epsilon k_B T}{2e^2\mathcal{I}}}. \tag{1.3}$$

In Eq. 1.3, the permittivity of free space $\epsilon_0 = 8.854\times10^{-12}$ F/m, ϵ is the bulk solution permittivity, the Boltzmann constant $k_B = 1.381\times10^{-23}$ J/K, T is the temperature, and the fundamental charge $e = 1.602\times10^{-19}$ C. The ionic strength $\mathcal{I} = \frac{1}{2}\sum_i z_i^2 c_i$ where z_i is the valence of ion i and c_i is the concentration of ion i. Beyond the Debye layer, the solution is electrically neutral. In common biological buffers, the Debye length is 1-10 nm.

DNA has an ionizable phosphate group in each base, and these bases are separated by only 0.34 nm. Charges along the polyelectrolyte chain interact and would repel each other strongly over lengths less than l_B; however, Manning showed that counterions condense onto the chain such that the effective

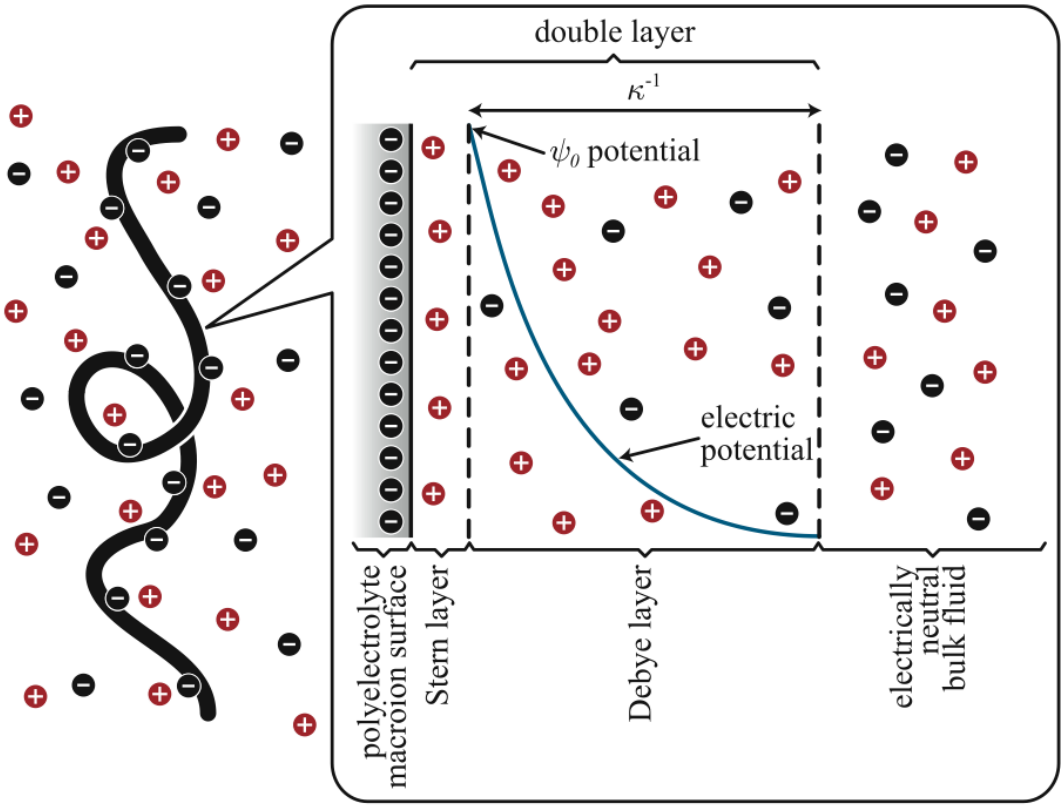

Figure 1.3: A polyelectrolyte in solution is surrounded by ions. In the Stern layer counterions are strongly bound to the polyelectrolyte. The Debye layer defines the region where the charges are non-uniformly distributed. Figure courtesy of Michel Gauthier.

charge spacing is equal to l_B [5].

1.2.2 Electrophoresis in Free Solution

Under the influence of an externally applied electric field, a charged particle will experience an electrophoretic force. Using the Rouse model, which assumes the polymer chain is freely draining, each chain segment acts independently. Rouse dynamics are applicable to electrical forces where the

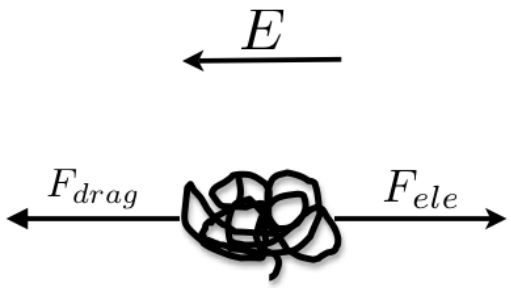

Figure 1.4: Polyelectrolyte dynamics in free solution under an applied electric field are dominated by two forces: electrophoretic force (F_{ele}) and drag force opposing motion (F_{drag}). Because DNA is negatively charged, it is driven in the opposite direction of the electric field.

interaction length is the Debye length. The chain is not free draining for non-electrical forces. The electrophoretic force is $F_{ele} = q_k N_k E$, where q_k is the charge on a Kuhn segment and E is the applied electric field. The motion due to this force is opposed by a drag force defined as

$$F_{drag} = U N_k \xi_k, \tag{1.4}$$

here U is the velocity of the polyelectrolyte and ξ_k is the friction coefficient of a Kuhn segment. Writing these forces in terms of the number of Kuhn steps is valid for long polyelectrolytes with many Kuhn steps. Because the velocity is strongly dependent on the electric field, electrophoretic mobility (defined in Eq. 1.5) is a more relevant parameter than the velocity. Mobility is given by

$$\mu = \frac{U}{E}. \tag{1.5}$$

The free solution mobility can be calculated from a force balance on the molecule. Equating the electrophoretic force and the drag force to solve for

velocity and using Eq. 1.5 we get

$$\mu_0 = \frac{q_k}{\xi_k} \sim N^0. \tag{1.6}$$

This free solution mobility does not depend on the size of the molecule if the polyelectrolyte has constant charge per length. Therefore, long DNA molecules cannot be separated by size in free solution.

1.2.3 Sieving Media

To separate a polyelectrolyte such as DNA by size, some type of geometry is required that will lend the mobility a size dependence. In practice, polymeric gels are used to act as obstacles to the electrophoresis of DNA. Convection is limited in a gel so that only the electrophoretic force and drag force are acting on the DNA. The two most common gels are agarose and polyacrylamide with average pore sizes of 200 nm to 500 nm and 5 nm to 100 nm, respectively [3].

Large globular particles traveling through a gel cannot sample all of the pores in the gel due to size restrictions. Smaller particles can move through smaller pores, and thus pass through the gel more quickly. DNA with radius of gyration smaller than the pore size does not need to deform to pass through the gel, and it can be treated as a globular particle. DNA with R_g greater than the mean pore size can also pass through the gel, but it must deform slightly and pay an entropic cost. This potential barrier slows DNA based on its size.

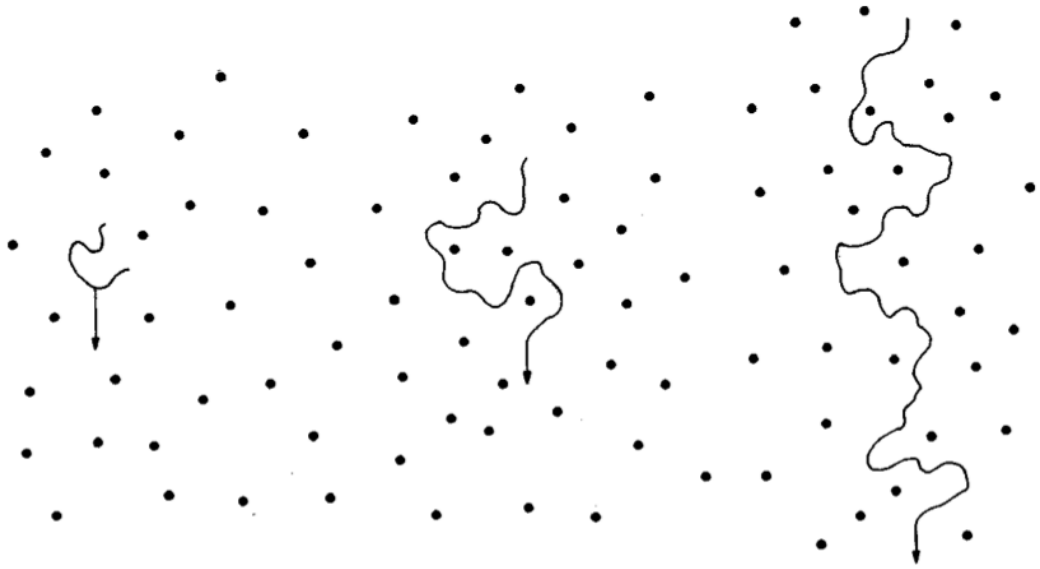

Figure 1.5: Different modes of DNA transport in gel electrophoresis. The left chain is small enough not to deform while moving from pore to pore. The center chain moves by repatation without orientation, and the right chain moves by reptation with orientation. Figure reproduced from [3].

1.2.4 Reptation

As the DNA polymer increases in length it encounters more obstacles in the gel matrix. The chain is forced to thread its way through the gel fibers as shown in Fig. 1.5. The gel fiber obstacles form a tube through which the polymer travels. We can describe the chain as containing multiple blobs that act as ideal Gaussian chains. The number of these blobs (N_{blob}) depends on the pore size a,

$$N_{blob} = N_k \left(\frac{l_k}{a} \right)^2 . \tag{1.7}$$

Sections of the polymer move from one blob to the next, and only exit the tube at either end. P. G. de Gennes called this mechanism reptation [6].

To find the mobility of a chain moving by reptation in a gel, we need to find the electrophoretic force acting on the chain in the direction of the electric field. Written in terms of the total charge of the chain (Q), end-to-end distance in the direction of the field (h_x), and contour length (L), this force becomes

$$F = QE\left(\frac{h_x}{L}\right). \tag{1.8}$$

Relating the electrophoretic force to the drag force and substituting $\mu_0 = Q/\xi$, we can solve for the the tube velocity and obtain

$$U_{tube} = \frac{\mu_0 E h_x}{L}. \tag{1.9}$$

To find the mobility of the molecule in the field-direction (x), we need to find the velocity in that direction. This velocity is simply the fractional extension of the chain in the x direction times the tube velocity, $U_x = U_{tube}(h_x/L)$. Substituting Eq. 1.9 for the tube velocity and taking the average extension over many tubes we obtain

$$\mu = \mu_0 \left\langle \frac{h_x^2}{L^2} \right\rangle. \tag{1.10}$$

A separation requires that mobility is dependent on molecular size in some way. Whether Eq. 1.10 yields a size dependence is determined by the extent to which the chain is stretched in the direction of the field. For small forces and relatively small molecules, the chain is not extended much in the direction of the field and behaves as an ideal chain: $\langle h_x^2 \rangle \sim L$. This case is known as biased reptation without orientation and gives a size dependent mobility: $L \sim N$ and thus $\mu \sim 1/N$. If the force on the chain is large, the chain will be almost completely extended in the direction of the field, $\langle h_x \rangle \sim L$

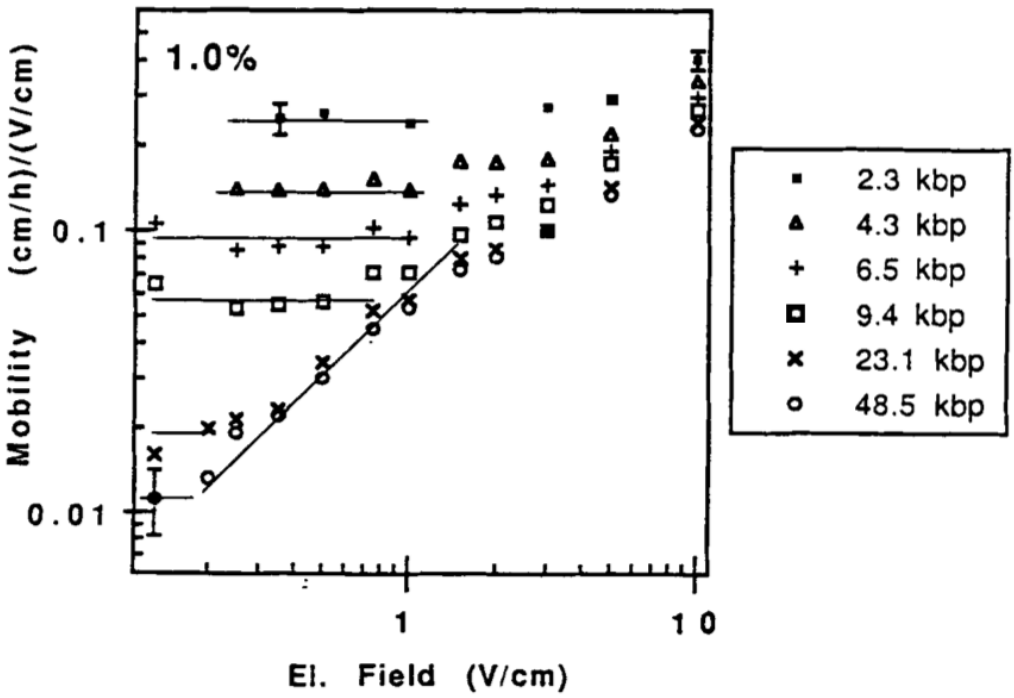

Figure 1.6: Mobility dependence on electric field in a 1.0% agarose gel. The mobility becomes independent of size for higher electric fields in agreement with Eq. 1.12. Figure reproduced from [7].

and $\mu \sim \mu_0$. This case, called biased reptation with orientation, gives no separation based on size.

In a weak applied field, defined by the dimensionless electric field, $\epsilon = q_k Ea/k_B T \ll 1$, orientation per segment is small. Short chains are unoriented, and long chains are oriented in the direction of the field. If we define N^* as the cross over size for orientation, we have:

$$\frac{\mu}{\mu_0} \sim 1/N, \quad N < N^* \tag{1.11}$$

$$\frac{\mu}{\mu_0} \sim \epsilon^2, \quad N > N^* \tag{1.12}$$

The reptation model correctly predicts that above a certain size ($N^* \sim \epsilon^{-2}$), continuous field electrophoresis cannot separate DNA. This model is extended by the biased reptation with fluctuations model [8], which gives the correct scaling of $N^* \sim \epsilon^{-1}$, as shown by the experimental data in Fig. 1.6.

1.2.5 Pulsed-Field Gel Electrophoresis

Because long DNA molecules become oriented in the direction of the field, a very low electric field must be used for separation. Fig. 1.6 shows that λ DNA (48.5 kbp) has no mobility dependence for E $>$ 0.1 V/cm. The time required for such a separation makes the experiments impractical. Gel electrophoresis can separate long DNA in a timely fashion, but the electric field cannot be applied in a constant unidirectional manner as it is for short DNA. Altering the direction or duration of the electric field is called pulsed-field electrophoresis and was introduced by Schwartz and Cantor [9] and Carle and Olson [10]. The mobility of DNA is not dependent on its size, but the time it takes to become oriented in the field direction is size dependent.

Cross field electrophoresis requires changing the direction of the electric field to drive DNA in a direction in which it is not oriented. Once the molecule is re-oriented, the field is switched again. During reorientation, the molecule is not moving forward through the gel. Shorter molecules re-orient faster and thus move faster through the gel. The separation time is very long, with a single separation requiring 4 to 72 hours [11]. Figure 1.7 shows a single molecule during cross field electrophoresis.

Field inversion electrophoresis changes the direction of the electric field by 180°. The pulse time and pulse strength are different in each direction. The

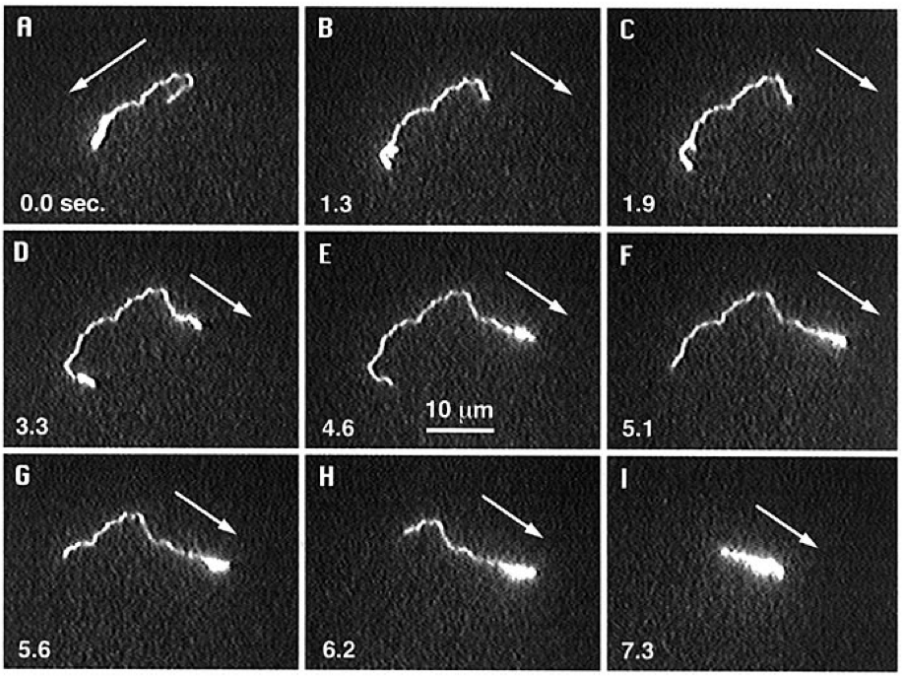

Figure 1.7: T2 DNA (164 base pairs) is originally oriented with the field and moving to the lower left (frame A). The field direction is then changed by 120^o and the chain reorients in the new field direction. Figure reproduced from [12].

reverse pulse allows the DNA molecule to relax. It is then driven forward by the forward pulse. This method requires only two electrodes to apply the field, while cross field electrophoresis requires more complex equipment to apply a field at various angles. Field inversion has a mobility minimum for certain sizes of DNA depending on the experimental parameters [13]. The occurrence of a mobility minimum is a serious drawback to field inversion electrophoresis.

1.2.6 Capillary Electrophoresis

Capillary electrophoresis is the current industry standard for separating short DNA molecules. It uses a thin capillary (inner diameter 50-100 μm) filled with an entangled polymer solution [3]. DNA interacts with the polymer in a similar way to how it interacts with a gel. Capillary electrophoresis is advantageous because it suppresses convection, can be easily automated, and dissipates heat from the electrical resistance of the fluid allowing the use of high electric fields which shorten separation times [3]. Capillary electrophoresis devices use either UV-absorbance or laser induced fluorescence at a small window to detect the DNA in the capillary. Because of the small detection window, this method does not need to separate DNA by a large physical distance to detect a size difference.

Direct current capillary electrophoresis has difficulty resolving DNA larger than 40 kbp [14] for the same reason that slab gel electrophoresis breaks down. Pulsed-field capillary electrophoresis has been used to separate longer DNA (48.5 kbp to 1 Mbp) in three hours [15]. This is much faster than in slab gel PFGE owing mostly to the increase in electric field. PFGE uses a maximum electric field of 10 V/cm [12], while capillary electrophoresis can use an electric field of 100 V/cm [15].

1.3 Microfabricated separation devices

The difficulties in separating long DNA motivate the search for a more efficient, faster method. Many of the emerging methods rely on microfabrication techniques pioneered by the microelectronics industry. These new methods have the potential to form a DNA size separation component in integrated lab-on-a-chip devices. Miniaturization of the required lab equipment also reduces the the amount of DNA sample necessary for sizing. Below, we

summarize several of these emergent microfluidic methods of long DNA separation.

In free solution DNA exists in a coiled conformation to maximize its entropy. The entropic recoil method uses an electric field to drive the coil of DNA from a region of high entropy to a region of lower entropy [16]. The low entropy region can be constructed from an array of nanopillars fabricated using electron beam lithography and reactive ion etching of a sacrifical polysilicon layer. The etched portion of the polysilicon is filled in with silicon nitride, and the polysilicon is dissolved away leaving only the silicon nitride. The final device had 80 nm pillars with 135 nm between pillars [16]. These nanopillars are roughly the same size as the Kuhn length of DNA, thus they sterically limit the conformations that the DNA polymer is allowed to adopt.

A time varying electric field is applied in the device to drive DNA into the low entropy region as shown in Fig. 1.8. When the posts are very densely spaced, the DNA needs to pay an entropic penalty when it unravels and beings to reptate through the post array. If the electric field is turned off and the DNA is only partially inserted into the post array, it will recoil back to the entrance of the array to maximize its entropy [17]. Since the time to completely unravel and enter the post array is a function of molecular weight, gradually increasing the duration and/or strength of the "Drive" pulse of the electric field should produce a separation as a function of molecular weight [16]. During the shorter pulses, the short DNA will be injected into the array and thus not feel the entropic recoil effect. As the pulse time increases, the short DNA will continue to move through the array but the long DNA will still remain outside the array until the pulse time is sufficient for complete injection. While the entropic recoil effect does lead to a separation via this mechanism [16], the resulting bands are very broad. Because DNA in a hairpin formation are injected at a different time than the same sized DNA that enter the array head-first they contribute to the high observed dispersion.

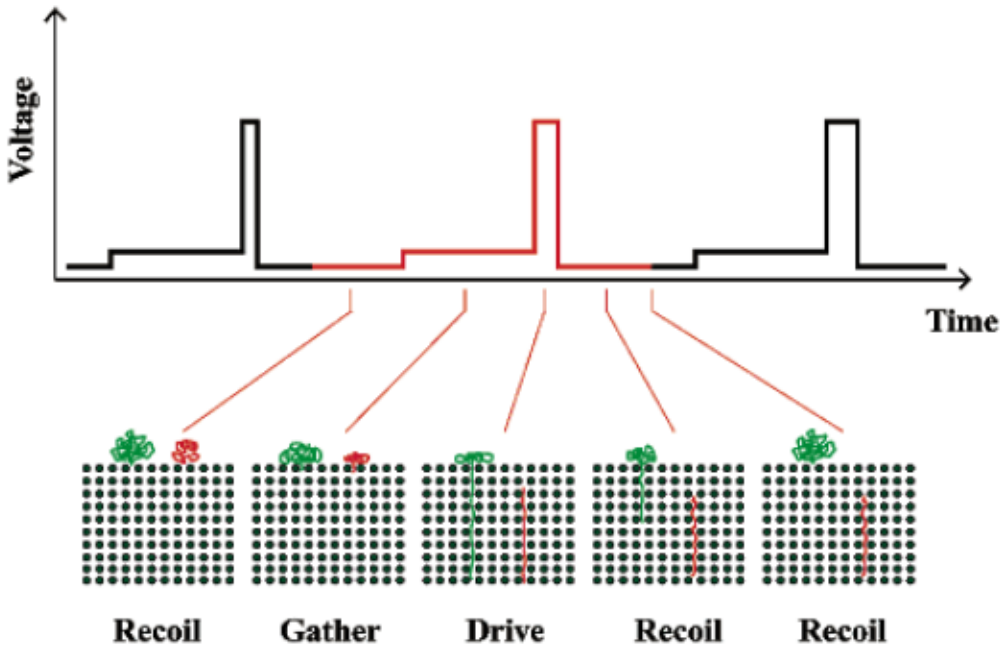

Figure 1.8: Scheme used to separate DNA by length using entropic recoil method. DNA is driven to the interface of high and low entropy regions during the **Gather** phase. A stronger field then drives the DNA into the pillar array - **Drive** phase. DNA not completely driven into the array recoils during the **Recoil** phase. Figure reproduced from [16].

Biomolecule separation based on Brownian motion was first proposed by Duke and Austin [19] and Ertaş [20]. Charged molecules are driven by an electric field through a two-dimensional array of asymmetric obstacles. The molecules diffuse by Brownian motion while traveling through the array. The array is designed such that the molecule can deflect to one direction with a much higher probability than the other direction as shown in Fig. 1.9. High molecular weight DNA with a small diffusion coefficient is less likely to diffuse to the next row of the array than a smaller molecule with a large diffusion coefficient. Cabodi et al. [18] used 3 μm by 12 μm obstacles in oxidized silicon to separate T7 and T4 DNA. The separation can be further improved by

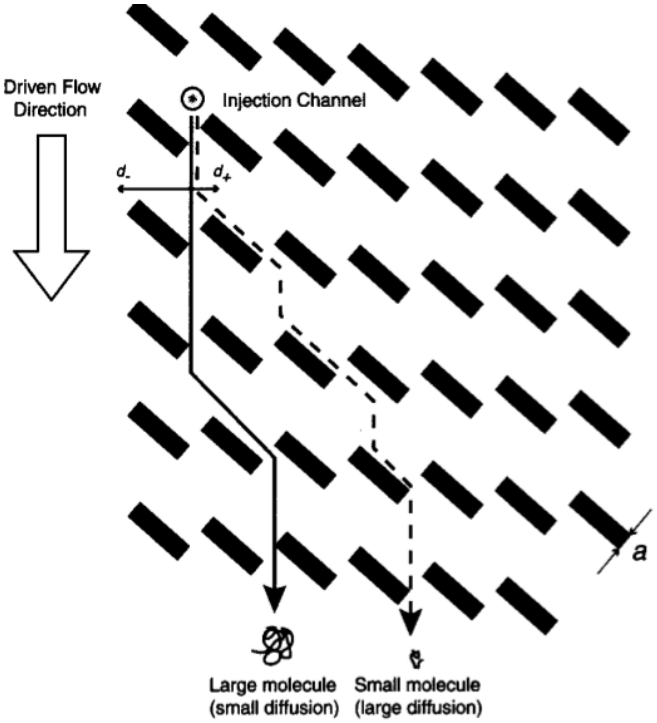

Figure 1.9: Principle of Brownian ratchet. Molecules are driven by an electric field, larger molecules have a lower diffusion coefficient than smaller molecules, and are more likely to continue in a straight line. Figure reproduced from [18].

tilting the direction of the applied electric field with respect to the array [21]. The tilted Brownian ratchet [21] increases the probability that a molecule will jump to a new row of the array. This method continuously separates DNA because it moves the DNA laterally rather than using a mobility difference in a one dimensional channel.

Arrays of large non-conducting polymer (PDMS) pillars with diameter of 15 μm, similar to the contour length of dyed λ DNA ($L \sim 22\mu m$), have been used to separate λ and T4 DNA [22]. These posts are too large for the DNA to wrap around the pillar; instead, the DNA is forced to shoot through the 1 μm gaps in between the posts. The entropic barrier for passing through

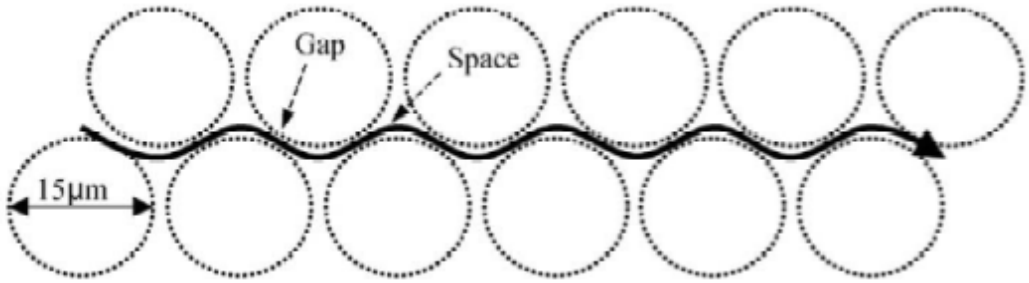

Figure 1.10: Path of DNA through an array of large PDMS posts. DNA can relax in the spaces between posts, then must squeeze between the next set of posts. Figure reproduced from [22].

these narrow gaps is larger for longer DNA molecules [22]. The 1 μm gap falls between the radius of gyration for λ DNA ($R_g = 650$ nm) and T4 DNA ($R_g = 1.2$ μm). Spaces between the pillars allow the DNA to relax to its coil conformation. Since a pulsed field is not required for this separation mechanism, the separation time is significantly reduced. The separation mechanism in this case is the entropic penalty for DNA motion through the narrow gaps between pillars.

A more direct use of the entropic trapping separation method utilizes a channel with alternating thin and thick regions as shown schematically in Fig. 1.11. In the thick regions the channel thickness (t_d) is larger than the radius of gyration of the DNA, the DNA can relax to its maximum entropy coiled form. In the thin regions, channel thickness (t_s) is smaller than radius of gyration, the molecule must flatten out to a more or less two-dimensional conformation. This entropic trap delays the motion of the DNA molecule through the channel.

Experiments in these devices show that longer DNA has higher mobility [23], in contrast to the large PDMS pillars [22]. These results have been confirmed by Monte Carlo [24] and Brownian dynamics [25–27] simulations. The molecule passes the low entropy region based on three time scales: approach

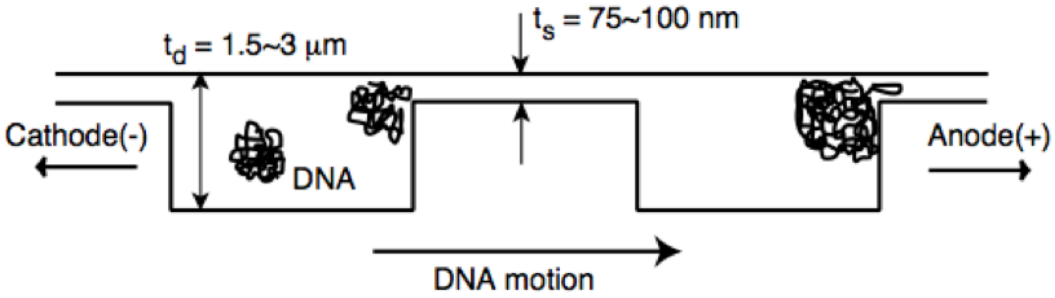

Figure 1.11: Side view of the entropic trapping device used by Han and Craighead [23]. DNA relaxes in large wells, while the thin regions are entropic barriers to DNA migration. Figure reproduced from [23].

to the entrance of the thin channel, entry of the thin channel, and crossing the thin channel [26]. The approach and entry times are smaller for long DNA while the crossing time is larger. In the Han and Craighead experiments [23], longer DNA showed higher mobility because approach time dominated crossing time [26]. Activation time dominates the total passage time for long DNA [26]. The activation time increases for larger molecules because the large molecule has more monomers that can enter the low entropy region.

While there are many more ideas for microfluidic based DNA separation, the methods have been reviewed elsewhere [3, 28]. The research presented here focuses on microfabricated post arrays, which are discussed in detail in the following chapter.

1.4 Research Outline

The remainder of this dissertation discusses advances the post array separation method through the use of experiments, Brownian dynamics simulations, and theory. A brief description of each of the chapters is given below.

Chapter 2

We describe the prior work on DNA separation in post array devices. This discussion includes the techniques developed to fabricate posts with diameters from hundreds of nanometers up to a few microns over centimeter long separation channels. We summarize the separation resolution achieved in experiments to date. This chapter also contains a discussion of the modeling of DNA dynamics during electrophoresis in post arrays.

Chapter 3

We present a study of the electrophoresis of long DNA in a strong electric field through a hexagonal array of cylindrical microscale posts spaced such that the pore size is commensurate with equilibrium coil size of the DNA. Experimental mobility, dispersivity, and videomicroscopy data indicate that the DNA frequently collide with the posts, contradicting previous Brownian dynamics studies using a uniform electric field. We demonstrate via simulations that the frequent collisions, which are essential to separations in these devices, are due to the nonuniform electric field, highlighting the importance of accounting for electric-field gradients when modeling DNA transport in microfluidic devices.

Chapter 4

Several continuous-time random walk models exist to predict the dynamics of DNA in micropost arrays, but none of them quantitatively describes the separation seen in experiments or simulations. In this chapter, we examine the assumptions underlying these models by observing single molecules of λ DNA during electrophoresis in a regular, hexagonal array of oxidized silicon posts. Our analysis takes advantage of a combination of single-molecule

videomicroscopy and Brownian dynamics simulations. Using a custom tracking program, we automatically identify DNA-post collisions and thus study a large ensemble of events. Our results show that the hold-up time and the distance between collisions for consecutive collisions are uncorrelated. The distance between collisions is a random variable, but it can be smaller than the prediction of existing models of DNA transport in post arrays. The current continuous-time random walk models correctly predict the exponential decay in the probability density of the collision hold-up times, but they fail to account for the influence of finite sized posts on short hold-up times. The shortcomings of the existing models identified here motivate the development of a new continuous-time random walk approach.

Chapter 5

Using the two-state, continuous-time random walk model, we develop expressions for the mobility and the plate height during DNA electrophoresis in an ordered post array that delineate the contributions due to (i) the random distance between collisions and (ii) the random duration of a collision. These contributions are expressed in terms of the means and variances of the underlying stochastic processes, which we evaluate from a large ensemble of Brownian dynamics simulations performed using different electric fields and molecular weights in a hexagonal array of 1 μm posts with a 3 μm center-to-center distance. If we fix the molecular weight, we find that the collision frequency governs the mobility. In contrast, the average collision duration is the most important factor for predicting the mobility as a function of DNA size at constant Péclet number. The plate height is reasonably well-described by a single post rope-over-pulley model, provided that the extension of the molecule is small. Our results only account for dispersion inside the post array and thus represent a theoretical lower bound on the plate height in an actual device.

Chapter 6

We present the design and implementation of an oxidized silicon "nanofence array" for long DNA electrophoresis. The device consists of a periodic array of post-filled regions (the nanofences) alternating with empty channel regions. Even in this prototype version, the nanofence array provides the resolving power of a hexagonal nanopost array without requiring any direct-write nanopatterning steps such as electron-beam lithography. Through detailed single molecule investigations, we demonstrate that the origin of the resolving power of the nanofence array is not a reduction in band broadening, which might be expected from the theories for DNA electrophoresis in post arrays. Rather, the enhanced stretching of the hooked DNA by the uniform electric field between nanofences increases the efficiency of the collisions.

Chapter 7

We used top-down fabrication techniques to create both an ordered hexagonal array and a disordered array of 1 μm diameter cylindrical posts in a silicon dioxide microchannel with the same number of posts per unit area. The electrophoretic mobility and dispersion coefficient of λ DNA in each of the arrays were obtained as a function of the electric field using ensembles of DNA molecules in a double channel device that minimizes experimental artifacts. To deepen our understanding of the transport, we also used fluorescence microscopy to examine the dynamics of single DNA molecules as they interact with the arrays at a fixed value of the electric field. Based on the results of these two types of experiments, we conclude that the electrophoretic mobility is not dependent on the array order but that band broadening in the device is greater in the disordered array.

Chapter 2

Microfabricated Post Arrays

Microfabricated post arrays contain many posts with diameters in the micron or hundreds of nanometers range. A typical videomicroscopy image of DNA collisions in a post array is shown in Fig. 2.1. While moving through the post array, the DNA molecules collide with a post, unravel, and disengage by a rope-over-pulley mechanism in a time that depends on the length of the molecule [29,30]. An electric field strength of at least 10 V/cm is required to significantly stretch the DNA molecule to form a hooking collision [31, 32], and the nature of the collision depends strongly on the relative distance between the center of mass of the DNA and the post (the impact parameter) [31, 33–35]. Since the electric field dominates diffusive motion, unhooking from the post is effectively a deterministic process even when the lengths of the two arms of the chain extending from the post are relatively similar [36]. During a collision DNA forms the four types of collisions (U, J, X, W) observed in Fig. 2.2 [37,38]. These only represent the types of collisions with a single isolated obstacle; there is a veritable alphabet soup of shapes are observed in the collision with multiple obstacles [39–41].

The DNA-post collisions are the basic unit of the electrophoretic separation

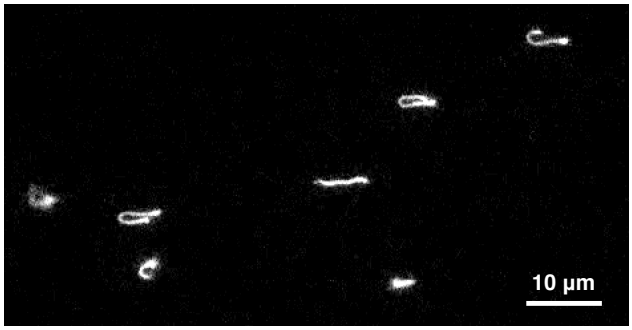

Figure 2.1: Epifluorescence microscopy image of dyed λ DNA molecules interacting with a hexagonal array of 1 μm diameter oxidized silicon posts. The electrophoretic motion is from left-to-right under an applied electric field of 10 V/cm.

in post arrays, and many collisions are required to yield a separation [30]. There are two ways to quantify the time that the DNA interacts with the post. From a modeling standpoint, the **unhooking time** is a convenient quantity. Indeed, most of the data for the collisions in Fig. 2.2 (except for the W collisions) collapses onto a simple model expressed in terms of the length of the short arm during the collision [37,42]. However, the unhooking time overestimates the contribution of a collision to the separation because it fails to account for the translation of the center of mass of the molecule during the collision [37]. Rather, the relevant parameter for separations is the **hold-up time**, defined as the delay in the center of mass motion due to a post collision [43].

The electrophoretic mobility of DNA in a post array depends on the frequency of collisions and the hold-up time of the collisions. Since the collision frequency is independent of the electric field [44] and the hold-up time is inversely proportional to electric field [37], the mobility is independent of electric field [44]. The holdup time itself depends on the molecular weight [29,30], which is the mechanism behind the separation [28]. In contrast to these hooking collisions, roll-off collisions resulting in little DNA deformation do

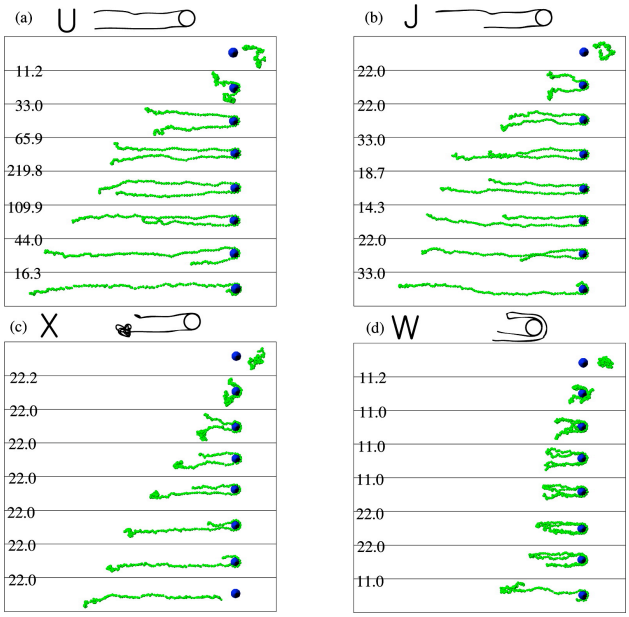

Figure 2.2: Examples of (a) U, (b) J, (c) X, (d) W collisions of T4-DNA (166 kbp) with an isolated 1.6 μm diameter post during Brownian dynamics simulations. The numbers on the left side of the images correspond to the dimensionless time between two successive snapshots. Figure reproduced from [38].

not significantly contribute to a sized based separation [43].

2.1 Artificial Gels

The protocols for making post array devices have matured through the years, with Fig. 2.3 showing the evolution of nanopost array technology from the first device [45] in 1992 to a very impressive high aspect ratio device [46] in 2006. In the devices used for separations, the channel widths are typically around 25 to 50 μm, with depths in the 4 to 10 μm range. The array itself extends along the axis of the channel. When electron beam lithography is used to pattern the array, which is common for densely packed nanoposts

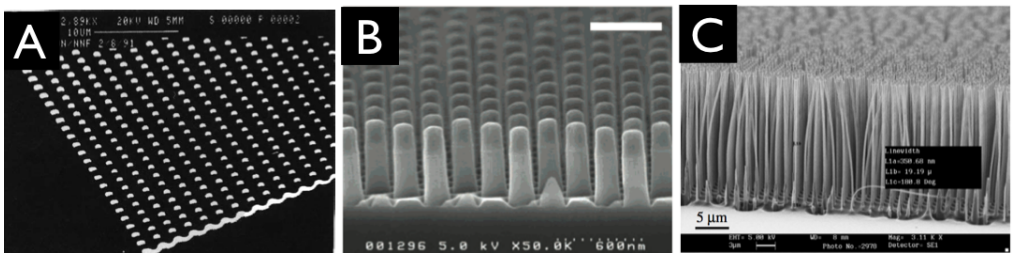

Figure 2.3: SEM images of microfabricated post arrays showing improvements in the fabrication process. (A) 1 μm diameter, 150 nm tall posts appearing in 1992 [45]; (B) 200 nm diameter, 600 nm tall posts appearing in 2004 [48]; and (C) 300 nm diameter, 15 μm tall posts appearing in 2006 [46]. Figures reproduced from [45], [48], [46]

[47–52], the array of posts with diameters in the hundreds of nanometers typically spans a millimeter in length. Moreover, electron beam lithography allows the posts to be patterned with very small gaps between them. These length scales can be reduced to such a small scale that nanopost arrays have also been used to filter out large DNA by a simple filtration process [53]. While the gel fibers of an agarose gel are much smaller that the nanoposts used in these arrays, the pore size in the device can be tuned to match the pore size of agarose gels. Indeed, the first post array device highlighted the potential for these systems to act as models for gel electrophoresis [45]. In contrast to the random, disordered fiber placement of a gel, nanopost arrays are highly ordered sieving matrices.

Note that electron beam lithography is not the only method for creating nanopost arrays. It is also possible to create densely spaced posts using nanosphere lithography, where a colloidal crystal serves as the etch mask [54] or soft UV nano-imprint lithography to produce high density, high aspect ratio nanopillars [52]. Yet another technique involves the removal of a sacrificial layer resulting in an insulating silicon nitride device [55]. Zinc oxide nanowires also create a dense array of very thin nanoposts [34]. While these nanowires are easily grown via solution chemistry and much thinner than the

silicon-based posts, the arrays are not ordered. Moreover, the experiments need to be performed at a pH near the isoelectric point of ZnO to avoid charging of the wires [34]. Although ZnO nanowires have been used successfully to study the physics of DNA collisions with isolated small posts [34], they have not yet been used as a separation medium.

2.2 Sparse Post Arrays

Arrays created by conventional photolithography techniques, which can pattern micron sized posts [29, 45, 56–60] as well as sub-micron posts [46, 61–63] are capable of producing centimeter long separation channels. Moreover, projection lithography permits access to sub-micron sized posts while maintaining a reasonably large area pattern [46,61,63]. If one desires a wafer-scale pattern of sparse nanoposts, it is possible to first pattern an array of micron sized posts in photoresist and then thin the post diameter down to several hundred nanometers using an oxygen plasma [35, 62].

The final device must be electrically insulating to allow electrophoretic motion of DNA through the channel. Fabricating the device in an insulating material such as quartz [48, 49] or fused silica [52] accomplishes this. An alternate approach is to build the channel geometry in silicon, and then grow an insulating layer on the silicon using thermal oxidation [46]. The growth of an oxide layer significantly increases the post diameter; however, Fig. 2.3c shows posts with a final diameter of 300 nm fabricated with this technique [46]. It is important to remember that the device fabrication often includes an undercut of the mask during reactive ion etching [63], so the diameter of the bare silicon posts pattern prior to etching is smaller than the original mask.

An alternative technique to produce sparse post arrays relies on the self-assembly of super-paramagnetic bead suspensions [44, 64–66]. In this ap-

proach, a solution containing super-paramagnetic beads with size around 600 nm is pumped into a PDMS microchannel. After the hydrodynamic flow is stopped, an external magnetic field of approximately 10 mT is applied with a magnetic coil, trapping the beads into a metastable quasi-hexagonal array of columns. Different array structures can be formed by washing the beads with different surfactants [44]. Due to aggregation of the columns as they form, the resulting array has micron sized posts with several microns between the posts. These arrays are considered only quasi-ordered due to this aggregation effect as well as defects introduced by the shape of the channel boundaries [67,68]. The order of the magnetic bead array can be increased by placing nickel dots on a glass substrate that act as seed points for magnetic bead self assembly [69].

2.3 Post Array Separations

The quality of a separation is measured by the separation resolution. This dimensionless group is defined for two species by the ratio of the peak-to-peak distance $(X_2 - X_1)$ and the sum of the peak widths $(\sigma_1 + \sigma_2)$ as shown below:

$$R_s = \frac{X_2 - X_1}{2\,(\sigma_1 + \sigma_2)}. \tag{2.1}$$

As a general limit, $R_s = 0.5$ is the limit for the detection of two peaks [70]; while $R_s = 1.5$ is considered baseline resolved.

Table 2.1 summarizes the separation data obtained in the various devices described here. Several trends are immediately clear from these results. First, the bands in the devices are usually resolved but not always baseline resolved in several minutes. Since the resolution should increase with the separation time, it should be possible to increase the resolution simply by increasing the

Table 2.1: Experimentally realized separation resolutions in post arrays.

Description	E (V/cm)	DNA sizes (kbp)	Time (s)	R_s	Ref.
500 nm, dense	10	1 and 10.1	130	1.45	[48]
500 nm, dense	10	10.1 and 38.4	170	2.69	[48]
500 nm, dense	10	4.4 and 6.6	520	1.08	[48]
500 nm, dense	10	6.6 and 9.4	520	1.04	[48]
500 nm, dense	10	9.4 and 23	680	2.39	[48]
300 nm, dense	500	48.5 and 166	120	1.0	[52]
150 nm, dense	30	2 and 5	60	1.43	[47]
150 nm, dense	30	5 and 10	75	1.56	[47]
1 μm, sparse	20	2.7 and 48.5	500	0.96	[59]
360 nm, sparse	10	15 and 33.5	1150	1.66	[62]
360 nm, sparse	10	33.5 and 48.5	1250	1.22	[62]
Nanofence	10	15 and 48.5	400	1.8	[63]
Nanofence	10	33.5 and 48.5	400	0.91	[63]
Magnetic beads	3.2	48.5 and 97	2000	2.0	[64]
Magnetic beads	3.2	48.5 and 145.5	2300	1.3	[64]
Magnetic beads	7	15 and 48.5	800	2.6	[64]
Magnetic beads	7	33.5 and 48.5	800	1.0	[64]
Magnetic beads	20.3	48.5 and 97	275	1.27	[65]
Magnetic beads	20.3	97 and 168.9	275	1.16	[65]
Magnetic beads	18.8	48.5 and 97	250	1.84	[65]
2 μm posts	Pulsed	48.5 and 168.9	660	17.96	[57]
2 μm posts	Pulsed	48.5 and 168.9	10	1.0	[57]

size of the post arrays. However, the lithographic techniques used to pattern the arrays have limited spatial extent. While it is possible to increase the separation channel length with the same device footprint by introducing serpentine turns in the channel, these turns can give additional dispersion [71–74]. Moreover, as the separation time increases, the signal-to-noise ratio deteriorates due to the band broadening. Recall that the depth of the channels (several microns) is commensurate with the radius of gyration of long DNA, so the number of DNA per unit volume is not very high. It is our experience that post arrays that include a serpentine channel to increase the

separation channel length do not lead to the expected square root increase in separation resolution, which we attribute to this increased band broadening and lower signal-to-noise ratio. Second, most of the experiments reported in the literature only use a few DNA species per experiment. Indeed, the most common experiments are separations of λ DNA (48.5 kbp) and its dimer, or between λ DNA and T4 DNA (168.9 kbp) or some other binary mixture. The reason for choosing these binary mixtures is the ready availability of these DNA and the inability for dc gel electrophoresis to resolve such long chains. Based on the available data in the literature, it appears that the band capacity (i.e., the number of species that can be resolved) for these devices is relatively low. While two species can be readily resolved in a manner of minutes, it remains to be seen whether a more complicated mixture of long DNA can be resolved in a single electrophoretic run. Based on our own work, we are not optimistic that the band capacity can be increased much beyond the separation data reported in the literature without increasing the depth of the channels, which is a technological challenge that has only been met in rare cases [46] like Fig. 2.3c.

While the particular arrays highlighted in Fig. 2.3 feature relatively dense arrays of posts, they require sophisticated fabrication techniques. We have wondered whether similar quality separations are possible using sparse, ordered arrays. Sparse ordered post arrays are easily fabricated using step-and-repeat masks and conventional photolithography, and these ordered devices have large spaces (relative to the DNA radius of gyration) between neighboring posts. If the array is very sparse [59], the DNA molecules tend to move in the interstices between posts and rarely collide with the posts of the array. This effect is known as channeling [58]. Brownian dynamics simulations have suggested that the long range orientational order in a post array leads to channeling [75]. Another simulation study showed that hairpin formation (or collision) is more frequent in disordered arrays, and that random post positions are essential for separations [76]. However, these simulations neglected

the deflection of the electric field lines around the insulating posts. Later Brownian dynamics simulations that accounted for the non-uniform electric field showed that DNA collides frequently in an ordered array and that this agrees with experiments in an array of 1 μm posts with 3 μm center-to-center spacing. These Brownian dynamics simulations are described in Chapter 3. The predictions of these simulations agree very well with experimental data for λ DNA electrophoresis in an array of 1 μm posts with a 3 μm center-to-center distance. Thus, it is reasonable to expect that relatively sparse post arrays fabricated using simple step-and-repeat patterns should lead to good separations of long DNA.

The conclusions drawn from the fundamental experiments and simulations in Chapter 3 have been confirmed in subsequent separation work. For example, experiments have demonstrated separations in sparse arrays of 1 μm diameter posts and 360 nm diameter posts, with the separation resolution between 15 kbp to 48.5 kbp DNA improving as the post size decreases [62]. Further Brownian dynamics simulations of DNA electrophoresis in 1 μm post with 3 μm center-to-center spacing predicted that λ DNA and T4 DNA have baseline resolution after 15 mm at E = 30 V/cm [41], which should require around 7 minutes. This separation resolution is higher for low electric field strengths [41], which also has been our experience in experiments in this type of post array.

2.4 Transport Models

The development of models for the separation and their application to experiments has taken a tortuous but ultimately successful path. As a historical aside, we should point out that extrapolations from simulation data and models for collisions with isolated, single posts [30,33], made a few years after the development of the first post array [45] in 1992, predicted that post arrays

would not be able to separate long DNA due to the dispersion caused by the collision [30] or the distance between posts required to realize the single post collision statistics [33]. As we have seen in our review of the various devices produced since 2002, there is ample experimental evidence to the contrary. It behooves us to briefly review how realistic models must incorporate both the statistics for the collisions with the posts and the transport in the array. A natural starting point would be the geometration models from gel electrophoresis [77–79], which already acknowledge the potential for DNA to undergo rope-over-pulley collisions at modest electric fields. A schematic showing DNA geometration in an array of obstacles appears as Fig. 2.4. It is readily apparent that the geometration models for a gel lacks predictive power for transport in post arrays, since they predict that the mobility is independent of molecular weight [79]. Thus, more sophisticated models of DNA transport were developed with the goal of predicting how the macrotransport properties such as electrophoretic mobility and band broadening depend on the DNA-scale physics. One early attempt was a semi-phenomenological lattice Monte Carlo model [80] that estimates the mobility and band broadening of the DNA as a function of the average collision time and the collision probability, both of which can be obtained from separate single molecule experiments [44] or a microscale physical model. However, when the relevant experiments were performed [44, 65], it became apparent that while many of the underlying assumptions of this model are qualitatively correct, the model fails to quantitatively predict the dispersivity during electrophoresis [44].

Further improvements in models for DNA transport relied on continuous-time random walk (CTRW) theory, in particular the Scher-Lax CTRW [81]. Originally developed by Scher and Lax to describe electron transport in disordered solids [81], the Scher-Lax CTRW model consists of a repetitive sequence of steps where the particle exhibits both a random waiting time at a trapping site and a random distance traversed between these trapping sites. Building

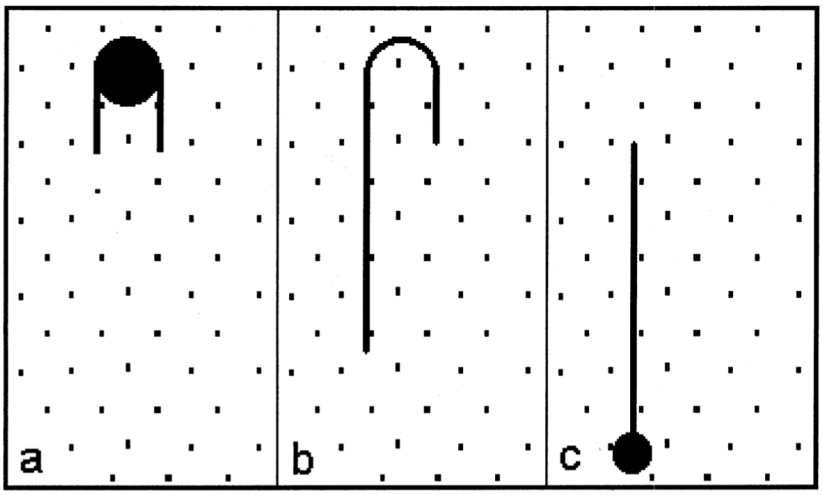

Figure 2.4: In the geometration model, DNA moves through an obstacle array in three distinct phases. (a) DNA in a coiled conformation encounters an obstacle and two arms start to form; (b) both arms become fully stretched and the molecule starts to slide off of the obstacle; (c) the molecule is released from the obstacle. Figure reproduced from [79].

on the geometration model for gel electrophoresis [79], the CTRW model for DNA electrophoresis in a post array consists of: (i) collision with post and extension into two arms, (ii) electric-field-driven unhooking from the post, and (iii) uniform translation until the next collision [44, 75, 82]. The configuration of the DNA molecule at the beginning of the collision determines the hold-up time of the collision. The first CTRW model applied to post arrays [44] assumed the chain was completely extended during the collision. To achieve accurate results in CTRW models, we must account for incomplete chain extension [75,82] as well as for the relaxation time and for interactions with multiple posts [41, 83]. Incomplete extension of the molecule does not strongly affect velocity, but increases dispersivity [82]. These CTRW models [44,75,82] treat successive collisions as uncorrelated events, an assumption which is experimentally verified in Chapter 4.

2.5 Post Arrays with a Pulsed Electric Field

Post arrays can also be operated under a pulsed-field, analogous to the pulsed-field gel electrophoresis separations we saw in Chapter 1. The fabrication methods are identical to the fabrication methods for dc field separation, and the origin for the advantages of using a post array are the same. The major limitation in pulsed field gel electrophoresis is the extraordinarily long time required for the DNA to reorient itself in the direction of the new electric field in the narrow pore sizes of a gel. By increasing the pore sizes to the micron scale in a post array, the DNA can readily reorient themselves in the new field direction. Pulsed-field operation of a post array device allows linear fractionation of long DNA [84], and using an entropic trap at the injection point permits the injection of a relatively narrow band of long DNA. Using the aforementioned properties of microfabricated post arrays, Austin and coworkers [57] demonstrated that very long DNA (100 kbp) can be separated in 10 seconds in a pulsed field.

The separation time during pulsed field electrophoresis in the post array device is a substantial improvement over the separation time required in PFGE. However, the complex apparatuses necessary for fabrication, operation and detection have thus far prevented widespread adoption of post array devices for long DNA separation. Overall, DNA separation in post arrays drastically decreases the separation time of long DNA compared to PFGE.

Chapter 3

DNA electrophoresis in a sparse ordered post array

This chapter is based on the publication:
J. Ou, J. Cho, D. W. Olson, and K. D. Dorfman
Physical Review E, **79**, 061904 (2009).

3.1 Introduction

Microfabricated and nanofabricated devices for DNA electrophoresis promise order-of-magnitude improvements in separation time and resolution when compared to conventional pulsed-field gel electrophoresis [85]. As a general rule, the physical principles underlying DNA transport in these devices are distinctly different from the biased reptation mechanism governing DNA electrophoresis in a gel [3]. Modeling has thus played a key role in elucidating the underlying separation mechanism each time a new device has appeared [86].

As a first approximation, it is simplest to treat the electric field as a spatially uniform convective force acting on each Kuhn segment of the DNA. However, many microfluidic electrophoresis devices are constructed in oxidized silicon or glass using fabrication tools from the semiconductor industry. Alternatively, devices are replica-molded in a plastic or elastomer from a lithographically patterned substrate. In either case, the electric field in these insulating materials is nonuniform and depends strongly on the device geometry. Thus, a uniform-field model implicitly assumes that spatial variations in the electric field can be treated, in a qualitative sense, as perturbations to conclusions drawn from a uniform-field model. For example, when nonuniform electric fields have been included in models of processes such as entropic trapping [24] or the collision with an isolated post [31], the details of the chain deformation change but the qualitative mechanism remains the same – the entropic trap still traps and the DNA still collides with the post.

We show here that uniform electric-field models do not correctly capture the dynamics of long DNA in a sparse ordered microfluidic post array. Post arrays, such as the one illustrated in Fig. 3.1, are one of the most well-developed microfluidic methods for separating long DNA by size [46, 48, 52, 64, 65]. The performance of dense nanopost arrays [46, 48, 52] or slightly disordered magnetic bead arrays [64,65] is typically rationalized in the context of conclusions drawn from uniform-field models [44,75,76,80,87]. Our results call into question these conclusions, demonstrating the generic importance of accounting for electric-field gradients when modeling DNA electrophoresis in microfluidic devices.

The basic transport process in a sparse ordered post array is illustrated in Fig. 3.1(a). The separation matrix consists of a hexagonal array of cylindrical posts of diameter d and center-to-center spacing a. The DNA moves through the spacing between the posts with a velocity $v = \mu_0 E$, where μ_0 is the free-solution electrophoretic mobility and E is the average value of the electric field in the direction of net motion. The DNA molecule is characterized by

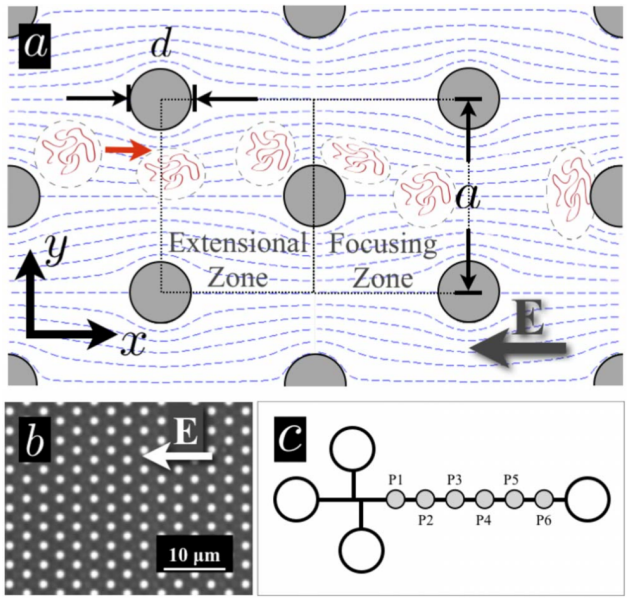

Figure 3.1: (a) Schematic illustration of a hexagonal array of cylindrical posts of diameter d and center-to-center spacing a. Several field lines created by the insulating posts are depicted in the figure. The equilibrium coil size of the DNA is commensurate with the spacing between the posts. The DNA move from left to right, in the direction opposite the electric field. (b) Image of a portion of a 50 μm $\times$ 15 mm PDMS hexagonal array of 1.2 μm diameter microposts with a 3 μm pitch. The electric field is applied from right to left. (c) To measure the mobility and dispersivity, the DNA are injected in a shifted-T geometry and the fluorescence intensity vs time is collected at i positions located $P_i = 2.5i$ mm downstream from the injection point. The microchannel is 50 μm wide and 1.97 μm deep.

its radius of gyration, R_g, contour length, $\mathcal{L}$, and molecular diffusivity, D_0. By a sparse array, we mean that

$$a - d > 2R_g, \tag{3.1}$$

so that the spacing between the posts is large enough for the DNA to relax in the interstices.

Let us consider first the predictions of a simple uniform-field model of DNA electrophoresis in this array. As noted elsewhere [87], after a rare collision with a post, DNA in a sparse ordered array can move through the "channel" between the posts with little hindrance. Assuming that the DNA needs to align with a post by molecular diffusion, the characteristic time between collisions is the diffusive time scale, a^2/D. Thus, the DNA will proceed unhindered through the unit cell when the convection due to the electric field is strong compared to diffusion. In other words, the unit-cell Peclet number is large,

$$\mathrm{Pe} = \frac{\mu_0 E a}{D_0} \gg 1. \tag{3.2}$$

After traveling a nominal distance $l_c = \mu_0 E a^2/D_0$, the DNA should have also experienced a collision with characteristic hold-up time $\tau_c = \mathcal{L}/v$ [29]. If we define the dimensionless parameter $\gamma = \mathcal{L}/a \gg \mathrm{Pe}$, the electrophoretic mobility from this model adopts the form

$$\mu/\mu_0 = (1 + \gamma/\mathrm{Pe})^{-1} \tag{3.3}$$

and is approximately unity. Moreover, for an array of total length L_T, this model predicts $N_c = L_T/(aPe)$ collisions will occur before the DNA exits the array. If N_c is not too large, then we would also expect the dispersivity of the DNA in the array, $\bar{D}$, to be close to the molecular diffusivity, $\bar{D} \sim D_0$. These generic conclusions, drawn from a relatively simple scaling analysis, agree with conclusions arising from Brownian dynamics simulations [87] that further account for the DNA elasticity and steric interactions between the finite-sized DNA and the post.

3.2 Methods

To test the predictions of this uniform-field model, we fabricated the polydimethylsiloxane (PDMS) post array depicted in Fig. 3.1(b) by soft lithography [88]. The post array was molded from a photoresist mold (Shipley S1818) patterned by photolithography. To assemble the chips, we spin-coated a #1 coverslip with a thin film of PDMS and bonded it to the replica-molded PDMS post array after exposing both substrates to an oxygen plasma. A 1" × 3" microscope slide with large cylindrical reservoirs (ID = 7 mm) was bonded to the back side of the chip for reinforcement and to suppress hydrodynamic flow. The completed and sealed chips were filled with TBE 2.2× buffer and submerged in buffer for 48 h at 55°C, a modification of the existing protocol [89] for preventing pervaporation. To perform replica experiments, the chips were regenerated by emptying them, refilling with neat buffer, and then soaking again in buffer at 55°C.

The electrophoresis experiments use λ-phage DNA (48.5 kbp) dyed with YOYO-1 (Molecular Probes) at 1 dye:5 bp in an electrophoresis buffer similar to Ref. [37], except that the β-mercaptoethanol was replaced with 100 mM DL-dithiothreitol. Previous experiments [32] on stained λ-DNA reported a contour length of 20 - 21 μm, so we will adopt $\mathcal{L} = 20.5$ μm. For the diffusivity and radius of gyration, we will use the free-solution experimental data $D_0 = 0.47$ $\mu\text{m}^2/\text{s}$ and $R_g = 0.7$ μm [90]. With the latter, our post/DNA system satisfies the sparse array definition (Eq. 3.1). Epifluorescence data were collected with a 63× oil-immersion objective using either a photomultiplier tube (Hamamatsu H7422-40) or an electron multiplying charge coupled device camera (Photometrics Cascade II).

To determine the electrophoretic mobility, μ, and dispersivity, $\bar{D}$, we implemented the multi-finish-line method illustrated in Fig. 3.1(c) [91]. The DNA are injected in a shifted-T configuration and we measure the time, $\bar{t}$, of the

maximum intensity and the full width at half maximum, τ, at different downstream distances, L.Assuming that the injected DNA plug is Gaussian at the detection point, μ and $\bar{D}$ can be computed from the relationships

$$\frac{dL}{d\bar{t}} \sim \mu E \quad \text{and} \quad \frac{d\bar{t}}{d\tau^2} \sim \frac{(\mu E)^2}{(16\ln 2)\bar{D}}. \tag{3.4}$$

The electric field in the separation arm was computed from the applied potentials using Kirchoff's laws and assuming a uniform resistivity. Importantly, the mobility and dispersivity computed by this method should be independent of the initial shape of the injection plug since they only depend on the slopes of the measured quantities. Occasionally, some experiments did not yield a linear fit (normally due to errors in the injection) and we only present data with correlation value $R^2 \geq 0.75$ when fit by Eq. 3.4.

3.3 Results

For λ-DNA electrophoresis in the array in Fig. 3.1(b) at a nominal Peclet number of Pe = 500, the uniform field model of Eq. 3.3 with $\gamma = 6.83$ predicts $\mu/\mu_0 \approx 0.98$ and approximately ten collisions over the 15 mm array. The latter mobility is much higher than the mobility $\mu/\mu_0 = 0.79 \pm 0.03$ we obtained by averaging our experimental data (see Fig. 3.3) over all fields. Our measurement of $\mu_0 = 1.8\times10^{-4}$ cm^2/Vs agrees well with previous measurements in PDMS devices [37].

While a reduced mobility is consistent with collisions in this ordered array, the dispersivity data presented in Fig. 3.2 provide much stronger support for collisions. Brownian dynamics simulations [87] using a uniform electric field predict that the dispersivity decays with Pe, asymptotically approaching the molecular diffusivity. However, the experimental dispersivity in the post array is orders of magnitude larger than what we observe in an empty channel

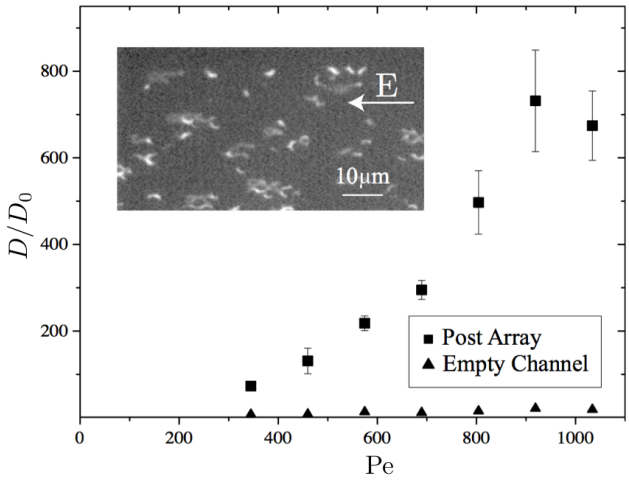

Figure 3.2: Plot of the experimentally measured dispersivity, $\bar{D}$, made dimensionless with the molecular diffusivity D_0, as a function of the Peclet number defined in Eq. 3.2. The squares correspond to measurements in the post array; the triangles correspond to measurements in an empty channel. The size of the error bars is one standard deviation; the error in the empty channel is smaller than the size of the symbol. The inset shows an image of the DNA dynamics at Pe = 230.

and increases with Pe. The dispersivity in the empty channel is also slightly higher than molecular diffusion ($\bar{D}/D_0 \approx 10$) and increases with Pe. We attribute this behavior to the dispersion caused by transient adsorption to the PDMS surface, which would be expected in a thin slit several R_g deep. In contrast, the large increase in the dispersion in the post array relative to the empty channel agrees with models of the dispersion due to collisions [44, 80].

To confirm that the DNA indeed collides with the obstacles, we also imaged the DNA during electrophoresis in this array. The inset of Fig. 3.2 presents one frame from a movie of the electrophoresis at a somewhat lower Peclet number (Pe = 230), which permits high-resolution imaging. Some of the DNA in this image are in the coiled conformation (the small bright spots); these DNA are moving between post collisions. The remaining DNA are in

extended J shapes (the enlarged dim lines); these DNA are in different stages of the unhooking process. Subsequent frames in this movie show that the hooked DNA in the inset of Fig. 3.2 undergo the expected rope-over-pulley mechanism.

These data make clear that the DNA collide with the posts much more frequently than predicted by a uniform-field model. To rationalize this result, we propose a nonuniform field model that draws analogies between the electric field and the equivalent potential flow in fluid mechanics. Let us consider the high-Pe trajectory of the DNA molecule in Fig. 3.1(a) as it passes by a post without colliding. The symmetry of the hexagonal array leads to a field line that extends from the back side of this post to a stagnation point at the front side of the next post in the x direction. The electric field on the back side of the post is curved and $E_y/E_x \gg 1$ there, so the electrophoresis toward this field line is much stronger than the electrophoresis toward the next post. The resulting focusing of the DNA increases the collision probability in two ways. First, the impact parameter approaches zero [33]; the center of mass of the DNA becomes aligned with the center of mass of the post. Second, the DNA will experience an extensional "flow" as it approaches the front side of the downstream post [31]. The combination of the focusing and extensional flow regimes leads to a time between collisions much smaller than the diffusive time scale a^2/D.

To see whether the inhomogeneous field indeed plays a key role in the DNA dynamics, we implemented Brownian dynamics simulations using either a uniform field [75] or the nonuniform field imparted by the insulating posts [92] using the parameters reported in [92]. In both cases, the λ-DNA was modeled by 37 beads connected by Marko-Siggia worm-like chain springs [93] corrected for the effective persistence length [94]. Excluded volume forces were modeled with a soft potential [95] and hydrodynamic interactions were neglected. The interactions between the DNA and the walls were treated with the Heyes-Melrose algorithm [96]. In the nonuniform field simulations, we first solved

Laplace's equation by the boundary element method using constant elements. At each time step in the simulation, the electric field vector **E** at the location of each bead was obtained by a regularization method [97]. To initialize the simulations, the DNA was relaxed in free solution, placed inside the array, and allowed to relax until fluctuations in the elongation decayed to a steady value [87]. We initially placed the DNA center of mass at three different points in the unit cell: immediately behind a post, in the center of the gap between two posts, and midway between the latter two positions. The center of mass was tracked over a distance of 400 μm and ten runs were performed for each initial position at each Peclet number.

The mobilities obtained from these simulations are plotted in Fig. 3.3 as a function of the Peclet number, along with the experimental data. We found that the simulated mobilities were essentially independent of the initial position of the DNA, so the data in Fig. 3.3 represent the average over all initial conditions and all random number seeds. The uniform field model in Eq. 3.3 overestimates the mobility since it neglects the fact that the DNA can collide with the post with an impact parameter greater than zero [33]. The uniform field simulations are qualitatively similar to those obtained elsewhere [75] using an electric field pointing from top to bottom in Fig. 3.1(b). In contrast, the simulations incorporating the nonuniform field exhibit a dramatically reduced mobility. Indeed, the agreement between the latter simulations and our experimental data is quite satisfactory and confirms the importance of the nonuniform field in modeling DNA electrophoresis in sparse ordered arrays. As the inset in Fig. 3.3 also makes clear, the number of collisions in the nonuniform field is roughly twice that in the uniform field.

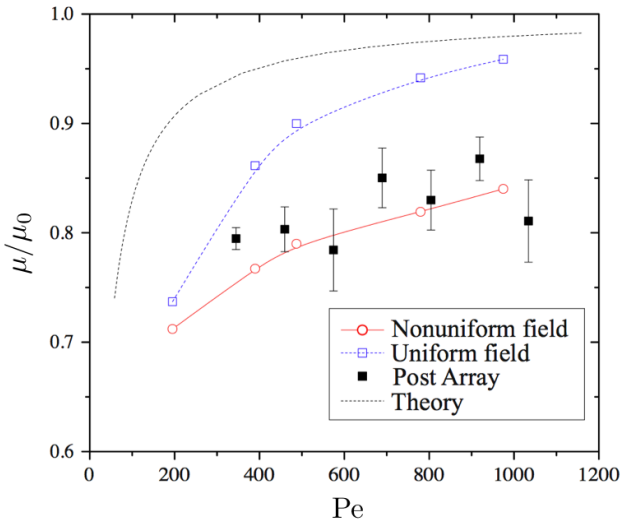

Figure 3.3: Comparison of the electrophoretic mobility, μ, made dimensionless with the free-solution mobility, μ_0, and the number of collisions as a function of the Peclet number between the experimental data (black squares), simulations with a nonuniform field (red circles), simulations with a uniform field (blue squares) and Eq. 3.3 (black dashed line). The size of the error bars for the mobility is one standard deviation; the error in the simulations is smaller than the size of the symbols. The simulation lines are only to guide the eye.

3.4 Conclusions

While uniform electric field models were extremely successful at rationalizing DNA electrophoresis in gels [3], the data presented here indicate that this may not be the case for emergent microfluidic and nanofluidic devices constructed in electrically insulating materials. In the present context, prior conclusions about post arrays [44,75,76,80,87] need to be revisited. In a broader context, our results open the question of whether electric field gradients have a similar impact on DNA transport in other devices with complex geometries. From a practical standpoint, the ordered arrays of micron-scale posts used here are relatively simple to fabricate by conventional photolithography and do

not require e-beam lithography [46, 48, 52] or the external equipment used to self-assemble magnetic bead arrays [64, 65]. As a result, it may be possible to design more efficient separation devices by building upon the nonuniform field model presented here using tools for simulating DNA electrophoresis in complex geometries [92, 98].

Chapter 4

Continuous-Time Random Walk Models of DNA Electrophoresis in a Post Array: I. Evaluation of Existing Models

This chapter is based on the publication:
D. W. Olson, J. Ou, M. Tian and K. D. Dorfman
Electrophoresis, **32**, 573–580 (2011).

4.1 Introduction

The first studies of DNA electrophoresis in micropost arrays [29, 45] hinted at their potential for rapidly separating long DNA by size. During the separation, the DNA repetitively collides with the posts of the array, with a size dependent collision time [30]. After several minutes, a large number of these collisions leads to a size separation of large DNA (15 to 169 kbp in typi-

cal experiments) under a dc electric field [46, 48, 52, 64, 65]. For comparison, the same separation by the standard method, pulsed-field gel electrophoresis (PFGE), takes 12 to 24 hours. While micropost arrays potentially offer a huge time savings over PFGE, they still remain at the proof-of-principle stage. We know that DNA transport on the microscale is governed by the array geometry and the applied electric field [66]; however, it is not clear how to tune these parameters to maximize the separation resolution for a given size range of DNA.

Evaluating the performance of a particular separation device requires knowledge of the mean velocity (or averaged electrophoretic mobility, in this case) and dispersivity as a function of the DNA size, array geometry, and electric field. The most obvious way to evaluate a given device geometry is to build the device and experimentally quantify the DNA separation therein. While there has been some work in this area [48,52,58,59,64,65], the data as a function of array geometry are limited because device fabrication is time consuming and expensive. As a result, Brownian dynamics (BD) simulations are an attractive alternative for rapidly exploring new device geometries [41, 58, 87]. However, if the only information taken from an ensemble of simulations is the averaged velocity of a molecule and its dispersivity, this simulation approach becomes very inefficient — gigabytes of simulated trajectory data are required to produce two numbers. In contrast, an analytical approach that treats the transport process as a repetitive cycle of collisions and translations [44, 79, 80, 82, 87, 99–101], i.e. a continuous-time random walk (CTRW), is potentially very efficient for device design, provided the underlying microscopic model is accurate.

At their heart, existing CTRW models rely on a model for the probability density of the DNA moving over n rows of the post array in some time t, $\psi(n, t)$. In a partially separable CTRW, this probability density is decomposed into the product of the probability density for moving n rows and the conditional probability of doing so in time t. The extant models approxi-

mate $\psi(n,t)$ using simplified microscale models of the DNA dynamics (e.g., rope-over-pulley collisions). Importantly, these models assume that (i) each collision is independent of the previous collisions [44, 79, 80, 82, 87, 99, 100]; (ii) the probability density of the distance between collisions decays exponentially after a no-collision zone [44, 82, 87]; and (iii) the collision time is described by a rope-over-pulley unhooking process with a uniform distribution of initial offsets between the arms [44,79,80,82,87,99,100]. Mobility and dispersivity calculations based on this approach are fast, but their accuracy is only as good as these unverified simplifying assumptions.

In the present contribution, we test these assumptions about DNA transport in a post array by direct observation of the microscopic DNA dynamics. Using single molecule videomicroscopy of λ DNA electrophoresis in an ordered post array, we investigated the probability densities for the hold-up time during a collision, t_H, and the number of rows between consecutive collisions, N_{rows}. We also tested the important assumption of independence of collision-translation cycles. Our experiments used an applied electric field of 10 V/cm, which prior experiments revealed is an appropriate electric field to separate DNA sizes near λ DNA [59, 64, 65]. We also compared our experimental data to the results of Brownian dynamics (BD) simulations of λ DNA at various electric fields in the same post array [41] to (i) test the accuracy of the simulation and (ii) extend our conclusions at 10 V/cm to a wide range of electric fields.

Our evaluation of the current DNA transport models in Chapter 4 motivates the development of a new method for estimating electrophoretic mobility and band broadening in Chapter 5.

4.2 Methods and Materials

4.2.1 Device Fabrication

Our array contains 1 μm oxidized silicon posts in a hexagonal array with a 3 μm center-to-center spacing. The post array is embedded in a 50 μm wide channel that connects a pair of 3 mm diameter reservoirs. The post array fills the entire 2 cm long channel with the exception of a 0.5 mm post-free region next to each reservoir. Although the array is relatively sparse, λ DNA collides many times in this type of array due to curved electric field lines caused by the insulating posts [58].

To fabricate the post array in oxidized silicon, we first grew a 30 nm layer of silicon oxide by thermal oxidation on a 4 inch silicon wafer. We then transfered the pattern of the channel and the posts from a chrome mask to S1805 photoresist (Shipley) on the wafer by photolithography and image reversal (YES 310). Subsequent wet etching of the exposed silicon oxide left an oxide mask of the posts and channel on the silicon wafer. We then used a Bosch process (Plasma Therm SLR 770) to etch the silicon to a depth of 2 μm, as measured by profilometry (KLA-Tencor P-16). We used a channel depth of 2 μm to match the depth of field of our microscope. After etching, we drilled access holes for each reservoir with a 3 mm diameter diamond drill bit. We then formed a 350 nm layer of oxidized silicon on the entire surface by thermal oxidation at 1200°C for 6 hours with an O_2 flow rate of 2 liters per minute. We characterized the chip by SEM (Fig. 4.1) after oxidation to confirm that each post has a diameter of 1 μm and the posts have a 3 μm center-to-center spacing.

The oxidized chip was sealed to a coverslip coated with NOA 81 optical adhesive (Norland Products). To do this without fouling the post array, we spin coated optical adhesive on the coverslip, then partially cured the

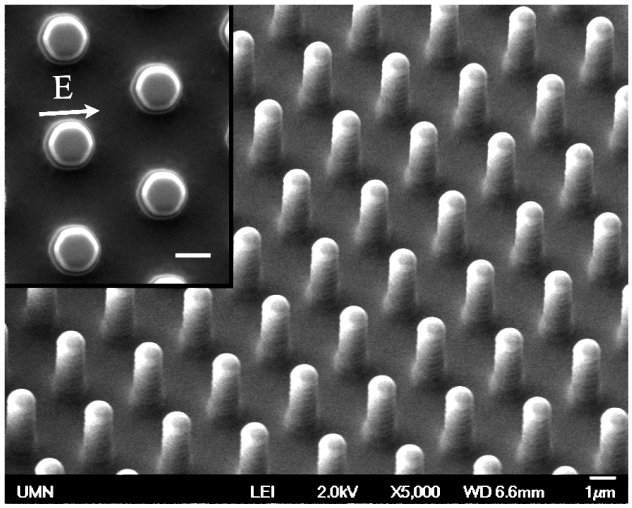

Figure 4.1: SEM images of the hexagonal array of cylindrical, 1 μm diameter oxidized silicon posts. The posts have a 3 μm center to center spacing and a height of 2 μm. The inset shows a top down view, where the scale bar is equal to 1 μm. The arrow shows the direction of the applied electric field.

optical adhesive by exposing it to UV light while it was in contact with a flat slab of clear polydimethylsiloxane (PDMS, Sylgard 184, Dow Corning). We pre-treated the PDMS with (tridecafluoro-1,1,2,2-tetrahydrooctyl)-1-trichlorosilane to prevent the PDMS from sticking to the optical adhesive. The PDMS is permeable to oxygen, which significantly retards the curing of the adhesive near the PDMS-optical adhesive interface [59]. After partial curing of the adhesive coated coverslip, we brought it into contact with the patterned side of the oxidized silicon channel. Reservoirs were affixed to each end of the channel on the unpatterned side of the wafer with optical adhesive. The completed assembly was fully cured by exposure to UV light for 2 minutes followed by 12 hours of heat curing at 70°C. We then filled the channel with DI water by capillary action.

4.2.2 DNA Imaging

We dyed λ DNA (48,502 bp, New England Biolabs) with the fluorescent dye YOYO-1 (Molecular Probes) at a ratio of one dye molecule to eight bp of DNA. Prior to DNA loading, we filled one reservoir of the channel with a solution of 1 wt% polyvinylpyrrolidone (PVP) in DI water. We left the other reservoir unfilled and allowed the solution to flow through the channel for one hour. PVP mitigates electroosmotic flow by forming a dynamic coating on the channel walls [102]. We then equilibriated the channel with a running buffer of 2.2x TBE, supplemented with 0.07 wt% PVP, 0.07 wt% ascorbic acid, and 3 vol% β-mercaptoethanol [32]. Before loading, we heated 200 μL of a solution of approximately 0.1 μg/mL λ DNA in running buffer at 70°C for 15 minutes to melt any λ DNA conactamers to single, linear λ DNA molecules. A potential difference of 20 V was applied across the 2 cm long channel using platinum electrodes and a Trek power supply (Model 677B), corresponding to a nominal electric field of 10 V/cm. The orientation of the electric field is shown in the inset of Fig. 4.1. In the channel, we observed the fluorescent λ DNA as they travel over a viewing window of 82.7 μm, corresponding to 30 rows of posts. Images were captured on an EM-CCD camera (Photometrics Cascade II) at 25 frames per second using a 100x, 1.4 NA, oil immersion objective on an inverted epifluorescence microscope (Leica DMI 4000B). Each image had 16 bit pixels and a pixel size of 162 nm. We captured several tiff image stacks of 1200 frames at 25 frames per second in the center of the channel, where the DNA has experienced numerous collisions before entering the frame.

4.2.3 Data Analysis

We used a custom MATLAB-based GUI to track the center of mass and the total intensity of DNA molecules in each frame of the image stack. The

tracking program first applied a 3x3 median filter to the raw image stack. Clusters of pixels above a threshold of 10% of the maximum intensity, but containing less than 50 contiguous pixels, were considered to be random noise. In our system, λ DNA spans at least 200 contiguous pixels; this size is comparable to an average equilibrium extension of 2.7 μm for λ DNA in a 2 μm deep silicone elastomer channel [32]. For each pixel cluster above the threshold and larger than 50 pixels, our tracking program extracted the position and size of the minimum bounding box of the cluster. We extracted the raw intensity of each pixel in the cluster, and calculated the centroid of the cluster weighted by this intensity value; we used this intensity-weighted centroid as the center of mass of the molecule in the following analysis.

Our tracking program also revealed the presence of λ DNA fragments in our device. These fragments correspond to pixel clusters that are larger than background noise, but smaller than λ DNA. DNA fragments could have resulted from photocleavage [103, 104], from shearing during loading [105], or were introduced from the stock DNA solution. To avoid including these fragments in the data set, we estimated the size of every molecule based on its total intensity, and eliminated those fluorescent objects that were smaller than a cut-off value corresponding to intact λ DNA [106].

During a collision, the leftmost edge of the bounding box of the molecule in Fig. 7.3 remains stationary for several consecutive frames. We were able to use the output from the tracking GUI to find these frames, and tentatively identified them as collisions. We then verified these collisions by first defining a coordinate system with the x-axis aligned with the electric field, and the y-axis transverse to the electric field, as in Fig. 7.3. Then, setting the origin at the post center, we confirmed the collision if the DNA molecule occupies all four quadrants of the space surrounding the post [37]. We found that our method was able to identify every single collision, along with some false collisions where the molecule failed to occupy all four quadrants of the post. These false collisions were removed from the data set. During

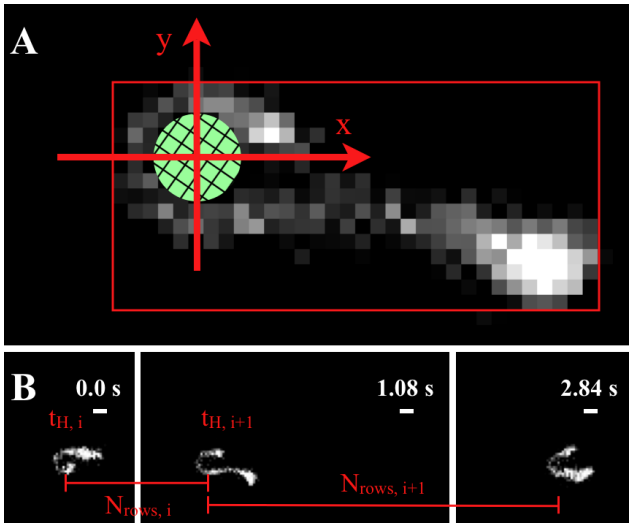

Figure 4.2: (A) DNA molecule colliding with a 1 μm diameter post. A collision occurs when the molecule occupies all four quadrants of the post centered coordinate system. The post, coordinate system, and bounding box were added to the single molecule image. DNA motion is from left to right. (B) Three images of collisions of a single molecule as it travels through the array. $N_{rows,i}$ is the number of rows between collision i and collision $i+1$, while $t_{H,i}$ is the hold-up time of collision i. Times shown in the upper right are relative to the first collision. The bars below the times correspond to 1 μm.

collision verification, we also identified several ($\approx 8\%$ of the total number of collisions) multiple post collisions. We broke these multiple post collisions into individual collision events to remain consistent with the above definition of a collision. In Chapter 5, we will see that these multipost collisions play a key role in band broadening [41].

Each collision takes place at a specific row of the regular array. Our collision identification method gave us the location of each collision. We then calculated the number of rows between collisions in the x-direction, N_{rows}, by taking the distance between collisions in x, dividing by the distance between the posts in the direction of the electric field, 2.60 μm, and rounding to the

nearest integer.

Since the center-of-mass of the molecule moves during collision, using the duration of the collision does not accurately predict the contribution of a single collision to the overall separation [37]. Before the first collision, after the last collision, and in between collisions the molecule moves at a well-defined drift velocity. During a collision, the center of mass of the molecule moves slowly, or not at all. For each collision, we calculated the time between constant velocity travel for each collision [37]. This time is the hold-up time, t_H, for the collision.

4.2.4 Comparison to Simulation Data

BD simulations of λ DNA in a 2 μm deep channel with 1 μm diameter posts with 3 μm spacing, which Cho and Dorfman recently used to compute the mobility and dispersivity of λ DNA, also provided us with a wealth of position versus time data for single molecules at different electric fields [41]. To complement our experimental data, we identified DNA-post collisions in the simulations when the molecule became hooked on the post. We then measured the probability density of hold-up times and number of rows between collisions as described above. The simulations span Péclet numbers, Pe, from 0.523 to 4.83, where

$$\mathrm{Pe} = \frac{\mu_0 E \xi l}{k_B T}. \tag{4.1}$$

In the latter, μ_0 is the electrophoretic mobility, E is the applied electric field, ξ is the friction coefficient on a bead, $l = 0.5833$ μm is the maximum extension of a spring, and $k_B T$ is the Boltzmann factor.

To make the conversion between the dimensionless simulation data and our experiments, we first measured the average velocity of DNA between collisions in the experiment from the mean of the distribution of frame-to-frame jump distances (when the DNA is not hooked on a post) divided by the

exposure time. This analysis established the effective in-array free-solution mobility of 1.45×10^{-4} cm^2/Vs. We measured the diffusion coefficient in the array from the standard deviation of the frame-to-frame jump distance distribution in an experiment in the absence of an applied electric field, finding $D = 0.25$ μm^2/s. The simulations use a freely draining chain, whereupon ξ is related to the diffusion coefficient by the Rouse diffusion model,

$$D = \frac{k_B T}{N_b \xi}, \tag{4.2}$$

where $N_b = 37$ beads were used to model λ DNA. This analysis leads to a bead friction coefficient $\xi/k_BT = 0.11$ s/μm^2, thus Pe = 0.914 is equivalent to E = 10 V/cm. For the hold-up time, we multiply the dimensionless simulation time by $\xi l^2/k_BT$ to obtain the time in seconds.

4.3 Results and Discussion

Using an analysis of single molecule observations and BD simulations [41], we tested the three main assumptions of the current CTRW models: (i) each collision is independent of the previous collisions; (ii) the distance between collisions decays exponentially after a no-collision zone; and (iii) the collision time is described by a rope-over-pulley unhooking process.

4.3.1 Correlations between Collisions

Theoretical models treat each collision as an isolated event [44, 79, 80, 82, 87, 99, 100]. We tested this assumption of independent collisions by measuring the correlation between consecutive collisions. For each collision the hold-up time, t_H, and the number of rows between collisions, N_{rows}, are the relevant parameters. As seen in Fig. 7.3, we label the hold-up time for collision i as

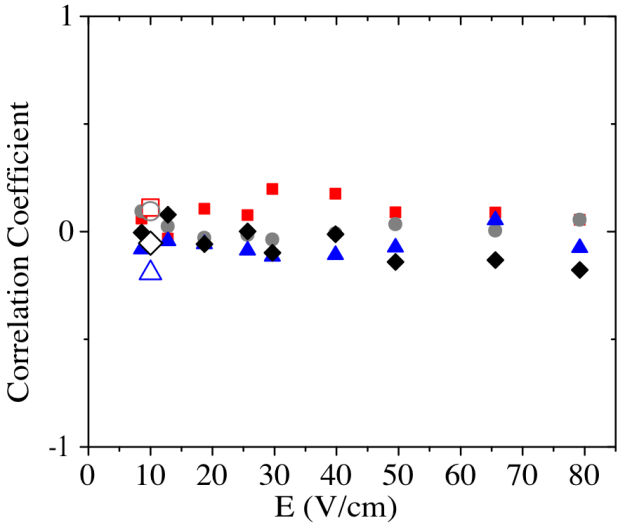

Figure 4.3: Correlation coefficient of $t_{H,i}$ and $N_{rows,i}$ (red squares), $t_{H,i}$ and $t_{H,i+1}$ (gray circles), $N_{rows,i}$ and $t_{H,i+1}$ (black diamonds), $N_{rows,i}$ and $N_{rows,i+1}$ (blue triangles) plotted against electric field for simulation data [41] (filled symbols) and the single molecule experiment (open symbols).

$t_{H,i}$ and the number of rows between collision i and collision $i+1$ as $N_{rows,i}$. We calculated the correlation coefficients between t_H and N_{rows} for collision i and t_H and N_{rows} for collision $i+1$. This gives us the four correlation coefficients in Fig. 4.3 to compare consecutive collisions. In addition to the experimental data, we revisited Brownian dynamics simulations of λ DNA in the same post array [41], allowing us to look for collision correlations over many different electric fields. Since the correlation coefficient has magnitude of less than 0.2 in all cases, we conclude that the values t_H and N_{rows} of a given collision are not correlated with the values of t_H and N_{rows} for the next collision. Thus, the collisions and the translation between collisions, as well as the cycle as a whole, can be treated as statistically independent events.

4.3.2 Distance between Collisions

To achieve a separation in a post array, many collisions are necessary [30] and the distance between collisions is important for modeling DNA transport. The current CTRW models of DNA transport in gels and microarrays offer four different predictions for the number of rows between consecutive collisions, N_{rows}. An early model developed for gels predicted that DNA will collide at evenly spaced intervals equal to the contour length of the molecule [79]. Later gel models [99, 100] used a random variable for the distance between collisions assuming that the number of collisions in a given distance follows a Poisson distribution. Subsequent models designed for post arrays took a micro-scale view of the process by setting the probability of collision with any given post as a constant, ρ, equal to the post diameter, d, [44, 82] or the radius of gyration, R_g, [87] divided by the post spacing, a. Since λ DNA has $R_g = 0.73$ μm [90], the two models are nearly equivalent for our system. The probability of colliding with a given post in the latter models [44, 82, 87] is given by $\rho(1-\rho)^{N_{rows}-n^*}$, where n^* is the number of rows before which a collision is not possible.

The length of this no-collision zone was originally taken to be the contour length of the molecule [44], but the model was later extended to account for the incomplete chain extension using a stem-flower model [82] or a worm-like chain model [87]. We can calculate the length of the predicted no-collision zone in our experiment; dyed λ DNA has contour length of approximately 21 μm [32]. This means that the no-collision zone in the model is either 7 rows (fully extended chain) or 5 rows (incomplete stem-flower extension [82]). These predictions are shown in Fig. 4.4.

Figure 4.4 also shows the probability density of N_{rows} from the experiment and BD simulations [41] binned in units of two rows to reflect the hexagonal geometry. The simulation data match the experimental data well, especially when we recall that hydrodynamic interactions are absent from the simula-

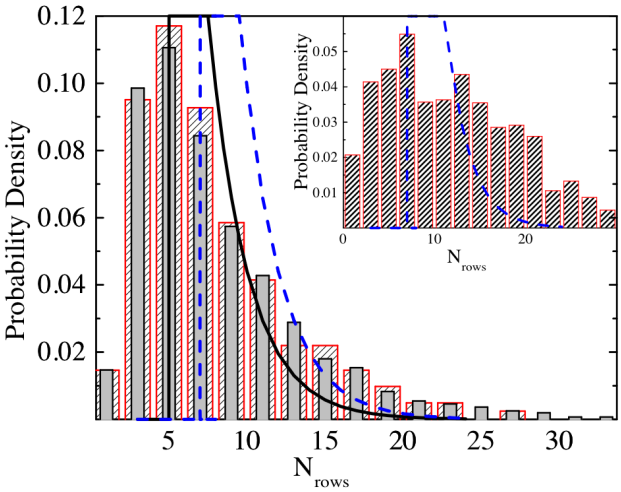

Figure 4.4: Probability density of the number of rows of posts between successive collisions for the experiment (striped large bars) and simulation [41] (solid thin bars) at E = 10 V/cm. The (blue) dashed line is the theoretical prediction at full extension, and the solid (black) line is the prediction of the incomplete extension model [82]. Both predictions use collision probability of $\rho = d/a$, and have maximum values larger than the maximum value of the ordinate. The bars in the inset shows the simulation results at E = 53 V/cm and the corresponding theoretical prediction at full extension.

tion and that the collision frequency depends on molecular diffusion. In both the experiments and the simulations, we observed collisions one row after the previous collision. These low N_{rows} collisions contradict the prediction of a no-collision zone [44, 82, 87]. However, we see that the probability of observing large values of N_{rows} decays exponentially as a function of the number of rows for the moderate electric field of 10 V/cm. The latter behavior agrees with the predictions of the microscale post array models [44, 80, 82, 87]. In contrast, the Poisson distribution assumed in the gel models [99, 100] decays too rapidly to fit the tail of the N_{rows} probability density.

The inset of Fig. 4.4 compares BD simulation results to the predictions of a post array model at E = 53 V/cm. At this high electric field, the stem-flower

extension of the chain is approximately equal to the contour length, thus only the full extension model is shown. Longer distances between collisions are more common for the high field case due to the strong convective force; the molecule can translate across many rows of posts before diffusing in front of a post. The large N_{rows} values constituting the tail of the N_{rows} probability density significantly increase the variance of position of the molecules, and thus increases the dispersion coefficient in the array. The models thus underestimate the dispersion coefficient and their prediction will be worse at high electric fields.

4.3.3 Hold-up Time

The DNA transport models [44, 79, 80, 82, 87, 99, 100] assume that the dynamics of the unhooking process are deterministic, but that the initial offset is random. The use of deterministic dynamics for λ DNA at these fields is supported by first-passage time modeling [36]. The models further assume that the initial offset is a uniformly distributed random variable [44], and Brownian dynamics simulations have shown that the initial offset indeed becomes uniform for high Pe [38]. A uniform initial offset leads to an exponentially decaying hold-up time probability density with maximum at $t_H = 0$ [79].

Our collision definition does not allow small initial short arm lengths; the four quadrant definition of a collision with a 1 um diameter post requires that the short arm be at least 0.78 μm long to form a hook. Since the typical maximum extension during a collision we observed in our movies is $\mathcal{L} = 9.4$ μm, the corresponding minimum fractional short arm length is 0.08 and the minimum rope-over-pulley hold-up time is $t_{H,\min} = 0.057$ s [87]. To compare this model with our data, we computed the predicted hold-up times from theory in Fig. 4.5 by using the hold-up time definition [87] and inverting it to a probability density [79] assuming that the initial short arm lengths

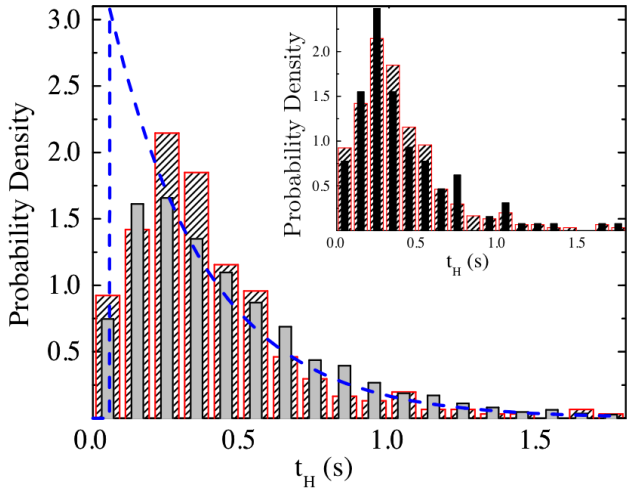

Figure 4.5: Probability density of hold-up times for collision from experiment (striped large bars) and simulation [41] (solid thin bars) at E = 10 V/cm. The dashed (blue) line is the theoretical prediction given by Eq. 4.3. The inset shows the hold-up time probability density of the full data set (striped large bars) compared to the hold-up time probability density for $N_{rows} \leq 7$ (solid thin bars).

are uniformly distributed on the interval [0.08, 0.5]. Using the hold-up time model for a single post [37], the probability density for the model is

$$\begin{aligned} P(t_H) &= 0, \quad t_H < t_{H,\min} \\ &= \tau \exp\left[-\tau(t_H - t_{H,\min})\right], \quad t_H \geq t_{H,\min} \end{aligned} \tag{4.3}$$

where $\tau = 2\mu_0 E/\mathcal{L}$ is the decay constant of the probability density.

Figure 4.5 shows a histogram of the hold-up times from experimentally observed collisions and from simulated collisions [41], again showing excellent agreement between experiment and simulation. The hold-up time probability decays exponentially for long times, in agreement with previous simulations [33, 107, 108] and an experimental study of single DNA dynamics in magnetic bead arrays [65].

For the most part, the model given by Eq. 4.3 provides a reasonable description of the experimental and simulation data. However, the model precludes very short duration collisions, which we observed in both simulations and experiments. These short hold-up times ($t_H < 0.057$ s) are due to collisions that delay the center of mass translation of the molecule without resulting in a J- or U-shaped collision. For example, X-collisions can have t_H less than the minimum rope-over-pulley hold-up time [37]. Since these non-rope-over-pulley collisions delay the center of mass of the molecule, they need to be included in the description of DNA transport. Accounting only for U/J-shaped rope-over-pulley collisions captures most of the data, but it is incomplete.

The data in Fig. 4.5 include all of the observed hold-up times, including the 129 collisions that occurred in the predicted "no-collision" zone ($N_{rows} \leq 7$) [44]. To look more closely at these events, we plotted the probability density for the ensemble of collisions occurring in the "no-collisions" zone in the inset of Fig. 4.5 along with the probability density of the full data set. The two densities are similar, showing that a wide range of hold-up times occur after small N_{rows} and providing further evidence that subsequent collisions are uncorrelated.

4.4 Conclusions

We evaluated the current models of DNA transport in microarrays [44, 79, 80, 82, 87, 99, 100] by direct observations of the macromolecular-scale dynamics of DNA molecules in both simulations and experiments. We found that consecutive collisions and translations in the array are uncorrelated, validating the assumption that collisions are independent events. The veracity of this key assumption lends confidence to the use of CTRW models in general to describe DNA electrophoresis in a post array.

Although the overall concept is sound, the current microscale models of DNA transport fail to accurately estimate two key components of the CTRW model, namely the probability density for the number of rows between collisions, N_{rows}, and the probability density for small values of the hold-up time of a collision, t_H. Accurately predicting these variables is crucially important because, as we will see in Chapter 5, the moments of these random variables determine the mobility and dispersivity of DNA in the CTRW model.

We showed here that a molecule can form a collision even when partially relaxed ($N_{rows} < 5$) and that a high number of rows between collisions occurs more often than predicted by the models. The excessively narrow probability density of N_{rows} in the current CTRW models causes an underestimation of the dispersion coefficient of DNA in the post array.

The rope-over-pulley model for hold-up times with a uniform distribution of short arm lengths greatly overestimates the probability of observing short duration collisions. To find better agreement with the observed hold-up time probability density, we modified the distribution of initial short arm lengths in the rope-over-pulley model to account for the finite sized posts in a physical device. With this modified model, rope-over-pulley collisions still have a minimum duration that is larger than the shortest observed hold-up times. Even with this modification, small t_H collisions are not accounted for in the current CTRW models.

Since the current microscale models fail to capture the details of the DNA dynamics during electrophoresis, we need to take a new approach to accurately predict mobility and band broadening in an array. In Chapter 5, we use our increased fundamental understanding of DNA transport on the single molecule level to make an improved DNA transport model based on CTRW statistics.

Chapter 5

Continuous-Time Random Walk Models of DNA Electrophoresis in a Post Array: II. Mobility and Sources of Band Broadening

This chapter is based on the publication:
D. W. Olson, S. Dutta, N. Laachi, M. Tian and K. D. Dorfman
Electrophoresis, **32**, 581–587 (2011).

5.1 Introduction

Continuous-time random walk (CTRW) models are a powerful tool for understanding, at a fundamental level, the sources of dispersion and concomitant band broadening during electrophoresis in a gel [79,99,100,109] or a microfabricated post array [66, 82, 87, 101]. We focus here on the latter system, which has the potential for rapid separations of long DNA [46, 48, 52, 64, 65]. Mod-

eling DNA transport in post arrays benefits from their ordered geometries and the insights gained from studies of the collision with a small, isolated post [28, 29, 37]. Thus, we are optimistic that a predictive model for DNA electrophoresis in post arrays, based on CTRW theory, ultimately will allow us to engineer such devices.

The existing CTRW models for DNA electrophoresis in a post array [66, 82, 87, 101] only qualitatively capture the mobility and band broadening seen in experiments and simulations. In Chapter 4, we investigated the microscale probability densities of the existing models using a combination of videomicroscopy experiments and Brownian dynamics (BD) simulations. We found that the probability density for the unhooking time is reasonably well captured by the standard rope-over-pulley microscale model [37], provided that we correct for the finite size of the post. In contrast, the distance between collisions is much harder to predict. In particular, the existing models for the distance between collisions [66,82,87,101] account for neither the electric field strength (apart from the chain extension during the collision) nor the local variations in electric field in an electrically insulating post array. The extant microscale models for the transport between collisions thus require significant modifications before they can be used for engineering purposes.

In this chapter, we take a different approach to CTRW modeling of DNA electrophoresis in a post array. Rather than start from some microscale model, we use a two-state CTRW model [110] to develop expressions for the mobility and the plate height in a post array that delineate the contributions due to the unhooking time and the distance between collisions. These are generic results that do not depend on any particular microscopic model. We used Brownian dynamics simulations to study both contributing factors as a function of the electric field strength and molecular weight for a given array geometry. Our approach permits a deeper insight into the transport process than we could obtain by simply computing the dispersivity (or plate height) alone [41,76]. Moreover, as the two-state model subsumes prior CTRW mod-

els [66,79,82,87,101,110] and expresses the mean velocity and dispersivity in terms of moments of the pertinent microscale processes, the approach here represents the proper starting point for future modeling efforts.

5.2 Methods and Materials

5.2.1 Two-State Continuous-Time Random Walk

Weiss derived the asymptotic results for a two-state continuous-time random walk [110] in which a given cycle of the walk leads to a displacement over a random distance $x = x_1 + x_2$ during a random time $t = t_1 + t_2$. In a post array, we define the first state as the translation between hooking events ($x_1 = x$, $t_1 = t_T$) and the second state as the hooked state ($x_2 = 0$, $t_2 = t_H$). If the moments of x and t are finite, the above model leads to the mean velocity [110]

$$\langle x \rangle = \bar{U} \langle t \rangle, \tag{5.1}$$

with $\langle t \rangle = \langle t_H \rangle + \langle t_T \rangle$. The dispersivity [110],

$$2\bar{D}\langle t \rangle = \sigma_x^2 + \bar{U}^2 \left(\sigma_{t_H}^2 + \sigma_{t_T}^2 \right) - 2\bar{U}\rho_{xt}, \tag{5.2}$$

includes a contribution due to the space-time correlation,

$$\rho_{xt} = \langle x t_T \rangle - \langle x \rangle \langle t_T \rangle. \tag{5.3}$$

In the latter equations, $\langle \cdots \rangle$ represents the average over many cycles and σ_i^2 is the variance of i over many cycles. For example, $\sigma_x^2 = \langle x^2 \rangle - \langle x \rangle^2$.

Using this approach, we calculated the dimensionless mobility from previous simulation data [41] finding that the two-state model gives an excellent prediction of the mobility. The predictions of the two-state model and two

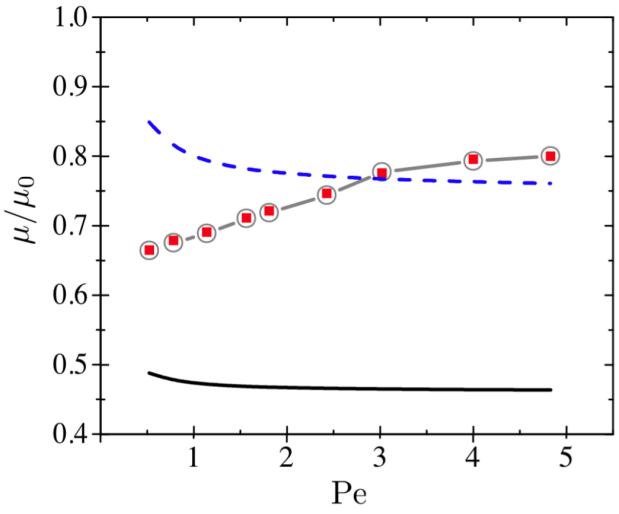

Figure 5.1: Dimensionless electrophoretic mobility of λ DNA in an array of 1 μm posts with 3 μm center to center spacing predicted from the wormlike chain extension model [87] (blue dashed line), and from the stem-flower extension model (black solid line) [82]. The red squares show the mobility measured from Brownian dynamics simulations in the same geometry [41]. Gray circles show the dimensionless mobility calculated from the model presented in this paper.

of the previous CTRW models [82, 87, 101] are shown against the simulation data [41] in Fig. 5.1.

5.2.2 Brownian Dynamics Simulations

We simulated DNA transport in a regular hexagonal post array of 1 μm diameter posts with $a = 3$ μm center to center spacing using Brownian dynamics (BD) in a non-uniform electric field. While we used a 2 μm high channel in Chapter 4 to aid visualization, we used a 4.5 μm high channel here to reflect the deeper channels used in separation experiments to increase the signal [48, 52, 59]. The simulation algorithm is described elsewhere [41]. Briefly, we used N_b beads connected by Marko-Siggia wormlike chain springs [93].

Excluded volume interactions were modeled with a soft potential [95]. Interactions between DNA and boundaries were handled by the Heyes-Melrose algorithm [96]. The key differences between the simulations used here and our prior work [41] are (i) the electric field is computed using a finite element solution; (ii) the code is vectorized in Fortran 95; and (iii) the post boundary is implemented as a continuous curve rather than an 448-sided polygon.

The ratio of convective forces to thermal fluctuations in the simulation was tuned by the Péclet number, defined as

$$\mathrm{Pe} = \frac{\mu_0 E \xi l}{k_B T}, \tag{5.4}$$

where ξ is the bead drag coefficient, $l = 0.5833$ μm is the maximum extension of a spring, $k_B T$ is the thermal energy, μ_0 is the free solution mobility, and E is the applied electric field. We simulated the trajectory of a molecule over 1 mm of the post array for Péclet numbers ranging from Pe = 0.523 to Pe = 20 and sizes ranging from $N_b = 12$ to $N_b = 42$, where $N_b = 37$ beads represents λ DNA.

Although we found a conversion between the simulation and experiment in Chapter 4, the latter was obtained using data for a 2 μm deep channel. To estimate the electric field corresponding to a given Péclet number in a 4.5 μm deep channel, we experimentally measured the diffusion coefficient of λ DNA in a 4.5 μm channel containing 1 μm diameter posts using the particle tracking method in Chapter 4. The corresponding diffusion coefficient, $D = 0.46$ μm^2/s, is the same as the bulk diffusion coefficient to within experimental error [90]. If we assume that the in-array mobility (i.e., when the DNA is not interacting with a post), $\mu_0 = 1.45 \times 10^{-4}$ cm^2/Vs, is also unchanged from its value in the 2 μm deep channel and the chain is freely-draining, these parameters lead to a Péclet number Pe = 1.14 being equivalent to an electric field E = 23 V/cm in the 4.5 um deep channel. In what follows, we use this Péclet number for the contant Pe case.

The following analysis is based on ensembles of 100 non-interacting molecules for each value of N_b and Pe. The data were analyzed using the same algorithms as in Chapter 4. Each data point thus consists of hundreds (or even thousands) of collisions. To estimate the error in our measurement, we calculated the standard error of each statistic. Since the standard error scales with the inverse of the square root of the number of collisions, the sampling error is very small. For example, for $N_b = 26$ the error of the plate height is between 1% and 2%. This error is smaller than the size of the symbols in the following plate height figures, and thus is not displayed. Since the difference in the mobility is much less than the difference in plate height, the error is significant and thus included in the mobility figure.

5.3 Results and Discussion

5.3.1 Limiting Cases

The current model captures the extant CTRW models [66, 82, 87, 101], which were based on the partially separable Scher-Lax CTRW [81]. The models [66, 82, 87, 101] assume that the translation between collisions occurs at the uniform rate $U = \mu_0 E$, where μ_0 is the free-solution electrophoretic mobility and E is the electric field strength. As a result, $x = Ut_t$, which implies that $\sigma^2_{t_T} = \sigma^2_x/U^2$ and $\rho_{xt} = \sigma^2_x/U$. The two-state dispersivity given by Eq. 5.2 then reduces to

$$2\bar{D}\langle t\rangle = \sigma_x^2\left(1 - \frac{\bar{U}}{U}\right)^2 + \bar{U}^2\sigma^2_{t_H}. \tag{5.5}$$

The term $(1 - \bar{U}/U)$ represents the delay caused by the hooking collisions and multiplies the variance in distance between collisions. Thus, Eq. 5.5 shares some semblance with the lever-rule.

All of the existing CTRW models [66, 82, 87, 101] assume a probability ρ of

colliding in a given row of the array after an exclusion region of size $n^* = \mathcal{L}/a$, where $\mathcal{L}$ is the length of the chain during unhooking and a is the spacing between posts. The corresponding expectation for the distance of a cycle is $\langle x \rangle = a\,(n^* + \rho^{-1} - 1)$ and the variance is $\sigma_x^2 = a^2\,(\rho^{-2} - \rho^{-1})$. If we include a pre-averaged unraveling of the chain during the collision [66, 79, 82, 101], then the expectation and variance for the holdup time are $\langle t_H \rangle = 3\mathcal{L}/(2U)$ and $\sigma_{t_H}^2 = \mathcal{L}^2/(4U^2)$. If we do not include the pre-averaged unraveling [87], then we subtract its deterministic contribution $\mathcal{L}/U$ from the expectation to give $\langle t_H \rangle = \mathcal{L}/(2U)$. Since the unraveling time is pre-averaged, the variance in the holdup time is unchanged.

Inserting these expectations and variances in Eqs. 5.1 and 5.5 readily leads to the mobility and dispersivity formulae reported in previous Scher-Lax CTRW models [66,87,101]. We have also confirmed, through significant algebra, that the Scher-Lax CTRW model of transport in a post array is equivalent to the present two-state model. We recall that the model of Ref. [66] with $\rho = 1$ leads to the geometration model [79], which is itself a Montroll-Weiss CTRW. Thus, the two-state model [110] that we adopt here is indeed a generalization of the existing CTRW models.

In the limit of zero posts, the dispersivity of the DNA should limit to the molecular diffusivity. However, this result cannot be recovered from Eq. 5.2 because the latter result was based on finite moments for x and t [110]. As the distance between collisions grows, the moments for x and t_T become unbounded and we reach an anomalous diffusion regime. (When a collision occurs, we would still expect the moments of t_H to remain bounded.) While results exist for unbounded moments in x [111], we have two reasons to believe this limit will not be of much interest for separations. First, the experimental data reported in Chapter 4 indicate that the distance between collisions decays exponentially and thus has bounded moments. Second, a system with large distances between collisions will have very low separation resolution. Nevertheless, if the distance between collisions were to decay

algebraically then the mathematical tools are available to modify the present analysis.

5.3.2 Electrophoretic Mobility

For each ensemble of molecules, we calculated the dimensionless electrophoretic mobility (μ/μ_0) according to

$$\frac{\mu}{\mu_0} = \frac{\langle x \rangle}{\mu_0 E \left(\langle t_T \rangle + \langle t_H \rangle \right)}. \tag{5.6}$$

We simulated 26 bead DNA at Péclet numbers from 0.523 to 4.83 and 12 bead DNA at Péclet numbers from 0.523 to 20 to measure the dependence of the mobility on the electric field.

The dimensionless electrophoretic mobility is shown as a function of Pe for $N_b = 26$ beads in Fig. 5.2. At low Pe, the mobility decreases with increasing Pe until a critical Péclet number, Pe*, is reached, after which the mobility increases with increasing Pe. These two regimes in DNA mobility have been reported elsewhere [76, 112]. For Pe $<$ Pe*, the number of collisions is limited by the relatively small stretching force when the chain collides with the post; the DNA is not pulled from its equilibrium coil state into a hairpin around the post. Indeed, we found many more molecules experience roll-off collisions at lower Pe numbers. As Pe increases in this low Pe regime, the number of collisions increases until the critical Pe* is reached. At the critical Péclet number, we observed the highest frequency of collisions and the lowest mobility. Scaling arguments suggest that Pe* occurs at Pe$^* N_b \approx 20$ [76], in agreement with our 26 bead DNA data. However, as seen in the inset of Fig. 5.2, Pe* occurs at significantly higher Pe than scaling laws predict for the 12 bead case. Note that the post diameter in our simulations is 1 μm, while the previous studies used 0.15 μm posts [76] or an asymptotically thin post [112]. The 26 bead DNA is large enough that the force required

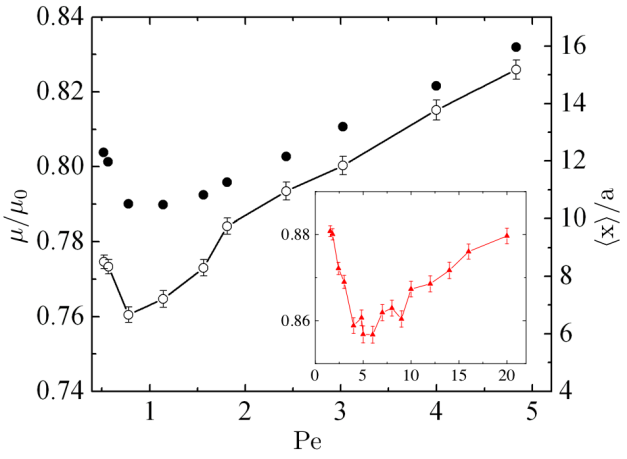

Figure 5.2: Dimensionless mobility (open circles) and mean distance between collisions (closed circles) as a function of Pe for 26 bead DNA. The inset shows the dimensionless mobility of the 12 bead DNA plotted against Pe. Error bars show the sampling error.

to stretch the molecule around a 1 μm diameter post is similar to the force required to stretch the molecule around a thin post. However, the force required to hook the 12 bead DNA is larger; thus Pe* is also larger.

For Pe $>$ Pe*, the number of collisions decreases with increasing Pe, resulting in an increase in mobility. In this high Pe regime, the collision frequency is limited by (i) the relaxation of the chain after a collision [41] and (ii) the lateral diffusion of the chain to a position in front of a subsequent post. These diffusive processes are largely independent of the applied electric field. Thus, at a higher Pe, the molecule bypasses more rows of posts before the subsequent collision.

Using the two state model, we can determine whether the change in mobility as a function of the electric field is dominated by the hooked state or the translating state. Since the hold-up time in the simulation scales linearly with Pe, we converted the hold-up time to a distance by $x_H = U\langle t_H \rangle$, similar to Eq. 5.1. This x_H is interpreted as the distance lost by the molecule

because of the collision [43]. We found that x_H increases slightly in the low Pe regime, then reaches a constant value of 5.47 $\pm$ 0.20 μm above Pe*. In contrast, the distance traveled during the translating state, $\langle x \rangle$, exhibits a strong dependence on Pe that mimics the trend of the mobility data, as seen in Fig. 5.2. We note that our simulations were run for a constant distance of 1 mm and thus $\langle x \rangle$ is inversely proportional to the number of collisions and the collision probability. Thus, the distance between collisions controls the change in mobility as a function of the electric field.

While the study of a single size of DNA at varying Pe reveals interesting physics behind the transport process, DNA separation occurs at a single Pe for many DNA sizes. To study the transport of a mixture of DNA, we simulated DNA sizes between $15 \leq N_b \leq 42$ at Pe = 1.14.

We found that the mobility decreases monotonically with the DNA size as expected from prior experiments in post arrays [28]. As in the constant Pe case, the mobility decreases as the number of collisions increases. The range of DNA sizes spans both transport regimes [Pe $<$ Pe$^*(N_b)$ and Pe $>$ Pe$^*(N_b)$] discussed in the previous section. In both regimes, larger molecules form more hooking collisions. At low Pe, the applied force required to form a hooking conformation is smaller for a longer chain; at high Pe, the collision probability is proportional to the size of the molecule in the direction perpendicular to the field, which is larger for a longer molecule. Thus, mobility should decrease with increasing size in both regimes.

We can again use the two-state model to determine the key factor governing the mobility. Here, it is convenient to invert the dimensionless mobility to clearly separate the two contributions:

$$\frac{\mu_0}{\mu} = \frac{U\langle t_T \rangle}{\langle x \rangle} + \frac{U\langle t_H \rangle}{\langle x \rangle}. \tag{5.7}$$

We found that the translation time and the distance traveled during transla-

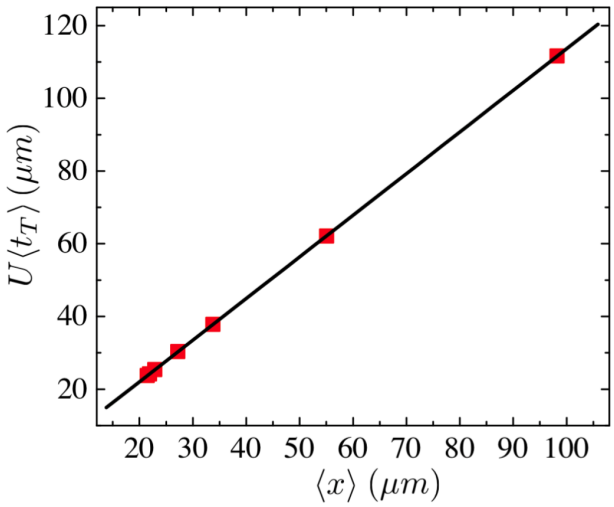

Figure 5.3: Plot of the translation time against the distance between collisions for the constant Péclet number case. The black line is a fit to the data, showing a linear relationship ($R^2 = 0.999$).

tion are related by $\langle x\rangle = [f(\mathrm{Pe})\mathrm{U}]\,\langle t_T\rangle$, where $f(\mathrm{Pe})$ accounts for the difference between the mean velocity and the instantaneous velocity of the molecule as it moves in the non-uniform electric field in the post array. In the previous CTRW models [66, 82, 87, 101], $f = 1$. Here, we simply assume that this parameter is independent of molecular weight. For the sizes studied here, linear regression to the data furnishes $f(\mathrm{Pe} = 1.14) = 0.89$ ($R^2 = 0.999$). A plot of $U\langle t_T\rangle$ versus $\langle s\rangle$ is shown in Fig. 5.3. Since the translation time and the distance traveled during translation exhibit a linear relationship, the first term of Eq. 5.7 is constant with changing DNA size.

According to the rope-over-pulley model of unhooking dynamics [37, 38, 87], the hold-up time scales with the extension of the chain during the collision, $\mathcal{L}$. To leading order, the extension of the chain depends linearly on the chain size; again using linear regression, we found that $\mathcal{L} = 0.33\ lN_b$ ($R^2 = 0.999$, Fig. 5.4). We therefore postulate that $\langle t_H\rangle$ dominates the second term of Eq. 5.7, and thus $U\langle t_H\rangle/\langle x\rangle$ has a linear dependence on N_b. With the plausible

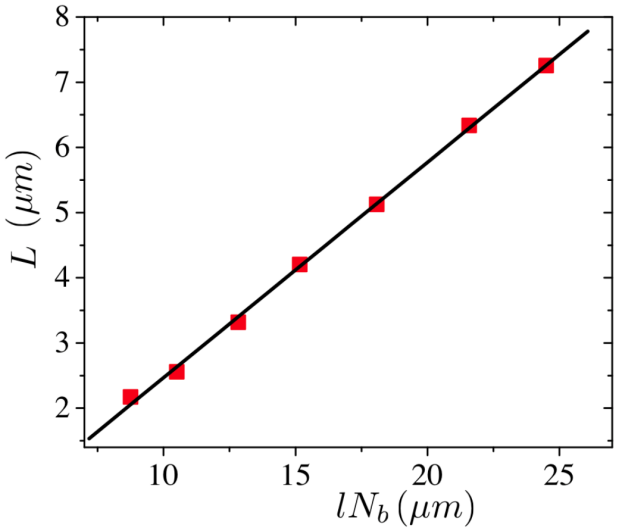

Figure 5.4: Maximum extension during collision versus the scaled size of the molecule at a constant Péclet number of 1.14. The black line is a linear fit to the data, showing a linear relationship ($R^2 = 0.999$).

assumption that $\langle t_H \rangle \sim N_b$, we can find an equation for the inverse mobility using linear regression, then invert the result to obtain

$$\frac{\mu}{\mu_0} = \frac{1}{1.0 + 0.010 N_b} \quad (R^2 = 0.961). \tag{5.8}$$

For $N_b = 26$ beads, the dimensionless mobility from Eq. 5.8 is 0.794, a 4% difference from the raw data. The discrepancy between the data and Eq. 5.8 is due to error in the regression. The original data, along with a plot of Eq. 5.8, are shown in Fig. 5.5. We find that Eq. 5.8 provides a better fit to the data than the $\mu/\mu_0 \sim N_b^{-3/2}$ scaling for single DNA-post collisions [33, 76]. Thus, at a constant Péclet number the dependence of the mobility on size is governed by the variable hold-up times of the different chains. While we certainly expected the mobility to depend on the collisions, our analysis shows that it is the duration, rather than the frequency, of the collisions that governs the separation. This contrasts with the constant size case, where

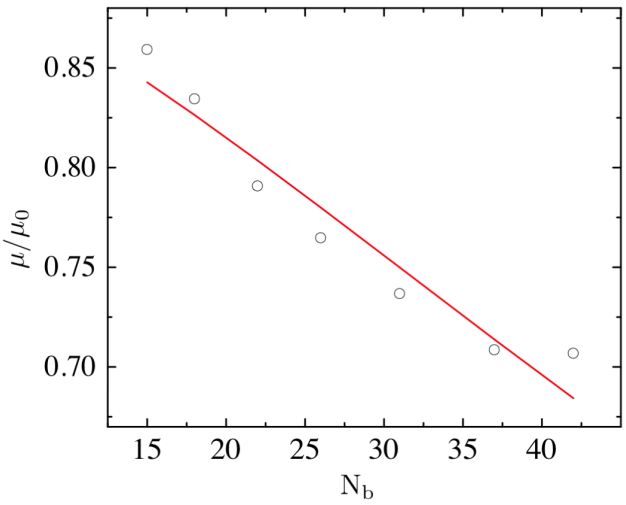

Figure 5.5: Dimensionless mobility versus the size of the molecule. The downward trend shows that separation based on size is possible provided that the dispersion in the system is low enough. The red line is Eq. 5.8, $R^2 = 0.961$.

the variation in the mobility is dominated by the number of collisions (or, equivalently, the frequency of collisions).

5.3.3 A van Deemter-like Equation

The general two-state model in §5.2.1 suggests a way to isolate the different sources of dispersion during electrophoresis in a post array. From a conceptual standpoint, our approach is analogous to the van Deemter equation for chromatography [113]. In the latter, the contributions to the plate height are apportioned to longitudinal molecular diffusion, eddy dispersion, and mass transfer. In the case of a post array, the dispersion comes from the random distance between collisions and the random collision time. The random distance between collisions takes dispersion and molecular diffusion into account, while the random collision time is analogous to the mass transfer term in the van Deemter equation.

We recast the two-state CTRW results in terms of the plate height,

$$H = \frac{2\bar{D}}{\bar{U}} = H_1 + H_2. \tag{5.9}$$

The first term is the contribution due to the fluctuations in the distance between collisions,

$$H_1 = \frac{\sigma^2_{x-\bar{U}t_T}}{\langle x \rangle}, \tag{5.10}$$

while the second term is the contribution due to the fluctuations in the holdup time,

$$H_2 = \frac{\bar{U}^2\sigma^2_{t_H}}{\langle x \rangle}. \tag{5.11}$$

In the following, we use H_1 and H_2 to investigate the various contributions to the plate height as a function of molecular weight and electric field.

The contributions to the plate height for $N_b = 26$ are shown in Fig. 5.6. The band broadening from state 1 (translation) is due to the random distance between collisions and the local velocity fluctuations caused by the non-uniform electric field. We found a piecewise linear relationship between the variance of the distance between collisions and the variance of the translation time as shown in Fig. 5.7:

$$\begin{aligned} \bar{U}^2\sigma^2_{t_T} &= 1.0\sigma^2_x - 17a^2 \ (R^2 = 0.999), \ \ \text{Pe} < \text{Pe}^* \\ \bar{U}^2\sigma^2_{t_T} &= 0.86\sigma^2_x - 7.6a^2 \ (R^2 = 0.999), \ \ \text{Pe} > \text{Pe}^*. \end{aligned} \tag{5.12}$$

Since the variance of the travel time and the variance of the distance between collisions are linearly related, $\sigma^2_{x-\bar{U}t_T}$ is nearly independent of Pe; it depends only on the relation between Pe and Pe*. The distance between collisions, rather than the local velocity fluctuations, is the dominant contributor to H_1, with $H_1 \sim 1/\langle x \rangle$.

The plate height due to the colliding state, H_2, is dependent on the hold-up

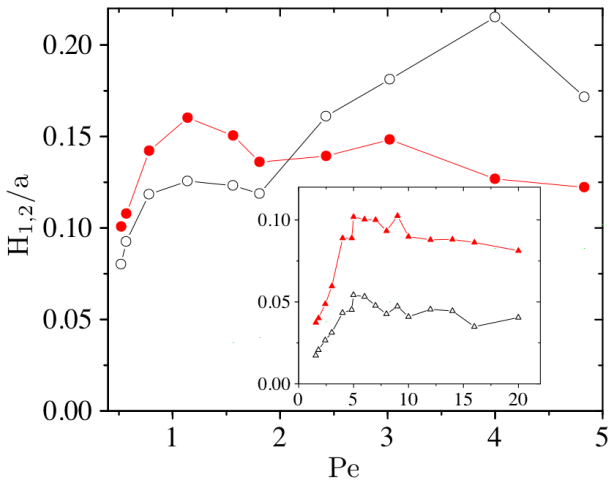

Figure 5.6: Plate height contributions from each state as a function of Pe for $N_b = 26$. Filled circles are H_1 and open circles are H_2. The inset shows the plate height contributions for $N_b = 12$ as a function of Pe, where filled triangles are H_1 and open triangles are H_2.

time of the collision. For a rope-over-pulley collision, the hold-up time is proportional to the extension of the chain during collision, $\mathcal{L}$ [37, 87]. Indeed, we find that this relation holds for the range of Pe studied here; linear regression provides $U\langle t_H\rangle = 0.55\mathcal{L} + 0.83a$ ($R^2 = 0.839$, Fig. 5.8). The average maximum extension of the 26 bead DNA is shown in Fig. 5.9. At the lowest Pe, $\mathcal{L}$ increases rapidly leading to an increase in H_2. At higher Pe, we see a drastic increase in H_2 once the extension of the molecule becomes greater than twice the row spacing. At this high extension, a single arm of the molecule can interact with multiple rows of posts, leading to an increase in the variance of the hold-up time, and thus an increase in H_2.

The extension of the chain can be estimated from the Marko-Siggia worm-like chain interpolation formula [87, 93, 114],

$$\mathcal{L} = l\,(N_b - 1)\left[1 - \left(\frac{N_b \mathrm{Pe} A}{l}\right)^{-1/2}\right], \tag{5.13}$$

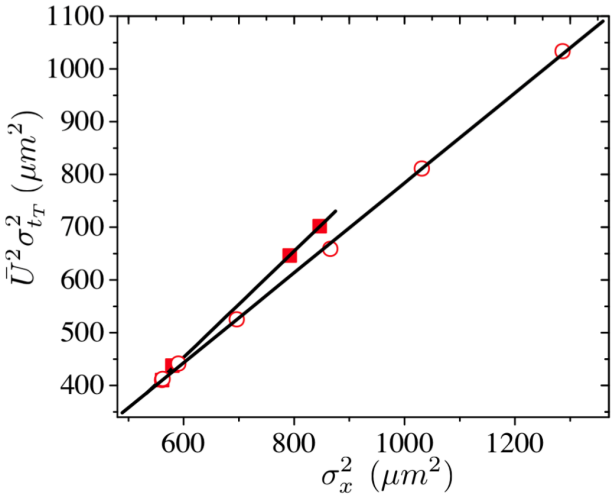

Figure 5.7: Variance of the translation time versus the variance in the distance between collisions at a constant DNA size of $N_b = 26$. Closed squares correspond to Pe $<$ Pe*, and open circles correspond to Pe $>$ Pe*. Black lines show linear fits to the data in each Pe regime (both fits have $R^2 = 0.999$).

where $A = 53$ nm is the persistence length of double-stranded DNA. Alternatively, we can model the extension of the chain during collision using the stem-flower model [82, 101, 115],

$$\mathcal{L} = l\,(N_b - 1)\left(1 - \frac{4l}{\mathrm{Pe}N_b l_k}\right), \tag{5.14}$$

where l_k is the length of a Kuhn monomer. Equations 5.13 and 5.14 are plotted with the simulation data in Fig. 5.9. Both models overestimate the extension of the molecule. Also, they predict multipost interactions at much lower Pe. As a result, these models only qualitatively capture the influence of the electric field on the likelihood of multi-post interactions in the array.

The inset of Fig. 5.6 shows the contributions to the plate height for $N_b = 12$. The band broadening from state 1 follows the same trend as the 26 bead case; H_1 increases with increasing Pe for Pe $<$ Pe*, then decreases above

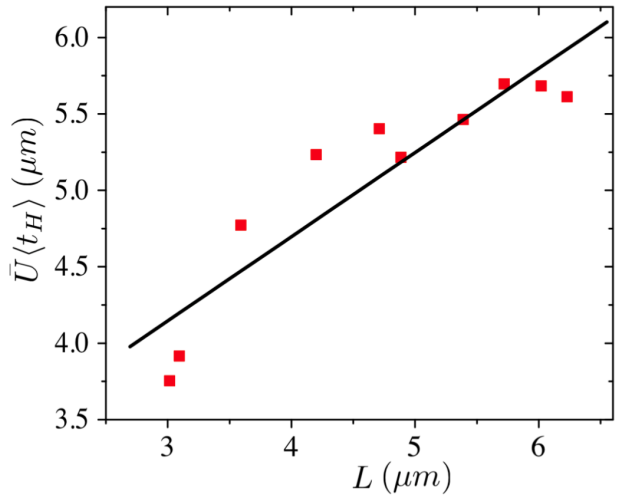

Figure 5.8: Hold-up time of the molecule versus the maximum extension of the molecule during a collision for a constant size of DNA, $N_b = 26$. The black line is a linear fit to the data ($R^2 = 0.839$)

the critical Péclet number. The plate height from state 2 (unhooking) only follows the trend of the 26 bead case below Pe*. The difference between the two constant N_b cases for Pe > Pe* is due to $\mathcal{L}$; the average maximum extension during a collision for the 12 bead DNA is $\mathcal{L} = 3.79 \pm 0.54$ μm and occurs at Pe = 20. Even at this extension, multi-post interactions are not important, and thus H_2 remains relatively constant above Pe*. Indeed, due to the relatively short collision times for this short DNA, the variance in the distance between collisions is the larger contributor to the plate height for all Peclet numbers.

In the case of a constant Péclet number, the plate height contribution from the translating state, H_1, is still driven by the number of collisions. We used linear regression to obtain

$$H_1 = \frac{1.4a^2}{\langle x \rangle} \quad (R^2 = 0.952). \tag{5.15}$$

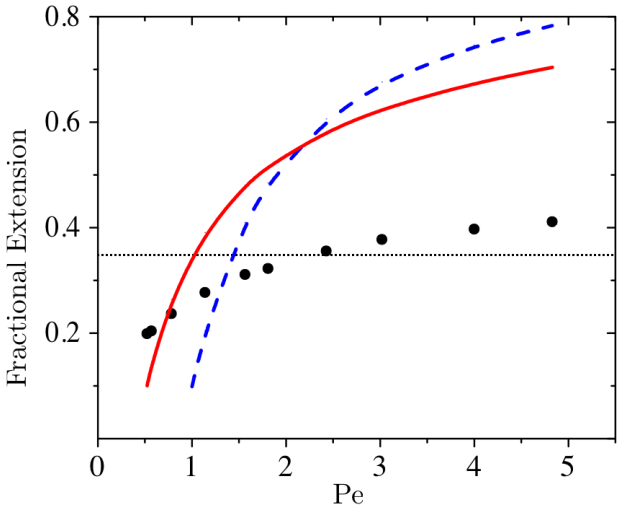

Figure 5.9: Fractional extension of the molecule in the field direction as a function of Pe for $N_b = 26$ (filled circles) plotted against the predictions of the stem-flower model [82, 101] (blue, dashed line) and the Marko-Siggia worm-like chain interpolation formula [87] (red, solid line). The horizontal dotted line is at an extension equal to twice the row spacing for this molecular weight.

The fit of H_1 is shown in Fig. 5.10 along with the simulation data. While DNA-post collisions cause a decrease in mobility and thus are necessary for separation, they also increase the band broadening in the array.

Based on the rope-over-pulley model of unhooking [37, 87], the hold-up time scales with $\mathcal{L}$, and thus $t_H \sim N_b$. We found that a good phenomenological fit to the data is

$$\langle x \rangle = b_1 \exp[b_2 N_b] + b_3, \tag{5.16}$$

where b_i are constants; this fit is shown in Fig. 5.11. Using Eq. 5.16 we are able to fit the simulation data for $\langle x \rangle$ with $b_1 = 4400$, $b_2 = -0.27$ and $b_3 = 22$ ($R^2 = 0.999$). We can then express the plate height due to hold-up as a

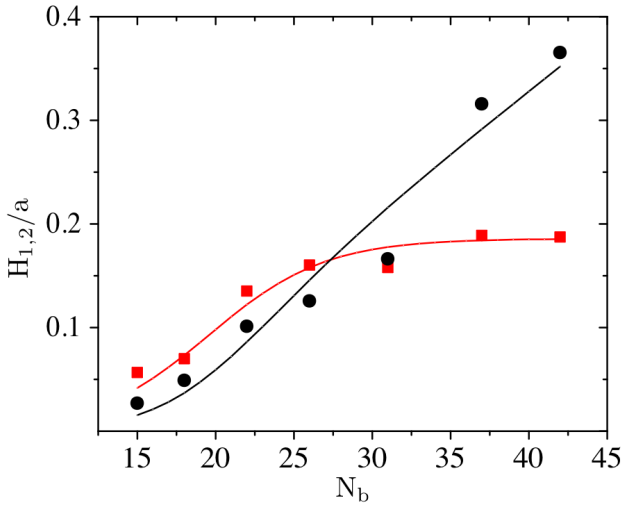

Figure 5.10: Contributions to plate height for changing DNA size. H_1 is shown in red squares, and H_2 is shown in black circles. The lines are the model equations for H_1 [Eq. 5.15] and H_2 [Eq. 5.17].

function of N_b by combining Eqs. 5.8, 5.16, and using $\sigma_{t_H}^2 \sim t_H^2 \sim N_b^2$,

$$H_2 = \left(\frac{N_b}{1.0 + 0.010N_b}\right)^2 \frac{c_1 a}{b_1 \exp[b_2 N_b] + b_3}, \tag{5.17}$$

where c_1 is the scaling coefficient. Using least squares minimization, we find $c_1 = 9.3{\times}10^{-3}$ ($R^2 = 0.958$). This fit is shown in Fig. 5.10 along with the simulation data. While Eq. 5.17 is a phenomenological model, it allows us to easily identify how the size of the DNA affects the second contribution (unhooking) to the plate height.

For Pe = 1.14, we found that the extension $\mathcal{L}$ remains smaller than the distance between posts for $N_b \leq 26$. As a result, we might expect this regime to correspond to the dispersion due to repetitive collisions with isolated posts. However, we found that the dispersivity in this regime scales like $\bar{D} \sim N_b^{2.2}$. This result differs from the dispersivity scaling from simulations of DNA collisions with a single post, $\bar{D} \sim N_b^{5/2}$ [76]. However, we note that dispersion

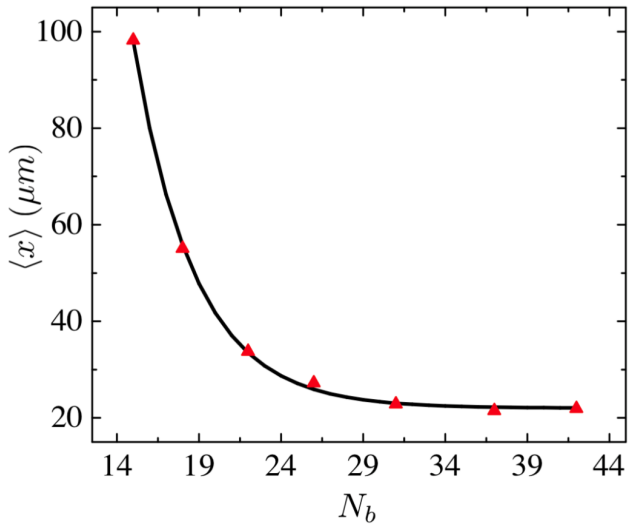

Figure 5.11: Mean distance between collisions as a function of the DNA size for the constant Pe case. Red triangles show the simulation data while the black curve is Eq. 5.16.

calculated from simulations in a random array of posts also exhibited a weaker dependence on chain length than the $N_b^{5/2}$ scaling [76], in agreement with our results.

5.4 Conclusions

Our analysis, based on a two-state model of DNA transport in a post array, allowed us to decouple the effects of (i) translation between collisions and (ii) hold-up during a collision on the electrophoretic mobility and the plate height. We found that the mobility of a fixed DNA size over a range of Pe depends primarily on the number of collisions experienced by the molecule, and that the number of collisions also predicts the observed mobility minimum. In this case the hold-up time is of secondary importance because $t_H \sim 1/E$. When the Péclet number is held constant and the size of the DNA is var-

ied, the change in mobility is governed by the hold-up time of the collisions rather than the change in their frequency. Thus, the state that dominates the change in the electrophoretic mobility depends on whether we consider mobility as a function of Pe, or mobility as a function of DNA size.

Using a van Deemter-like equation we calculated the plate height due to the different states of the molecule. The plate height due to translation between collisions scales with the number of collisions. The plate height due to the variable hold-up time of a collision is well predicted by the single post rope-over-pulley unhooking model for small molecules and low Pe. However, large molecules under a strong electric field have such a large extension that the effects of multiple posts become important. Since these multi-post effects increase the variance in the hold-up time [41], they increase the plate height.

Our results make clear the usefulness of the two-state model [110], since it allows us to interpret the various factors contributing to the mean velocity and band broadening. We should also point out that the mathematics required to produce meaningful results from the two-state model are trivial compared to those required for the equivalent Scher-Lax treatment [66]. In the latter approach, one begins with the probability density $\psi(x,t)$ for moving a distance x in a time t and computes the asymptotes of the first two moments from the solution to the random walk [81]. In the context of a post array model, the steps include inverting the microscale model for the holdup time (which can only be done with certain limiting assumptions [79]) and extensive algebra. In contrast, the two-state model given by Eqs. (5.1)-(5.3) allows a rapid calculation of the mean velocity and dispersivity from the moments of the microscale processes. Importantly, these moments are obtained without inverting the holdup time model. Thus, we posit that the two-state model provides the ideal starting point for any future CTRW studies of DNA electrophoresis in a post array.

Chapter 6

DNA electrophoresis in a nanofence array

This chapter is based on the publication:
S.-G. Park, D. W. Olson, and K. D. Dorfman
Lab on a Chip, **12**, 1463–1470 (2012).

6.1 Introduction

Long DNA in the tens of kilobase pair (kbp) range cannot be readily separated by conventional dc gel electrophoresis [7], and the alternative approach, pulsed-field gel electrophoresis, requires hours to separate these DNA [9]. Ordered post arrays, embedded in a microfluidic channel, increase the range of DNA sizes that can be separated by electrophoresis in a dc electric field [45, 46, 48, 49, 51, 52, 58, 59, 61, 62, 64, 65, 116] because the mechanical stability of a post array permits much larger pore sizes than are possible in a gel. DNA electrophoresis in pores larger than its radius of gyration does not take place by biased reptation [3]. Rather, the DNA moves primarily in its re-

laxed, coiled conformation. The separation is effected by occasional collisions between the DNA and the posts, where the DNA is deformed [28–30, 117]. Both the duration of a collision and the distance traveled between collisions are random variables [44, 60, 66, 76, 80, 82, 83, 87, 118] that depend on the size of the DNA, electric field, and the arrangement of the posts.

In this chapter, we present an improved post array geometry for long DNA electrophoresis that we call the "nanofence" array. Existing post array devices for DNA electrophoresis use a regular lattice of posts, [45, 46, 48, 49, 51, 52, 58, 59, 61, 62, 116] either in a hexagonal or square configuration, or a quasi-hexagonal array of self-assembled magnetic beads [64, 65]. In contrast, the nanofence device shown in Fig. 6.1 consists of regions of closely spaced posts (the nanofences) separated by a relatively long distance (20 μm) between them. Our recent results on the origin of the band broadening in post arrays [60, 83] led us to hypothesize that the nanofence should have sharper bands since the DNA collide at regular intervals. In such a system, the distance between collisions is no longer a random variable and its contribution to the plate height should vanish [83]. We show here that, remarkably, the nanofence array provides a high separation resolution but actually exhibits an increase in band broadening compared to a hexagonal geometry. Through detailed single molecule investigations and continuous-time random walk (CTRW) modeling, we provide evidence that the uniform field lines between collisions lead to more efficient collisions with the posts. Even with the increased band broadening due to these collisions, the nanofence ultimately exhibits a separation resolution comparable to the best results presented for a hexagonal array of posts. As the device in Fig. 6.1 is only a prototype version, we expect that the nanofence array will quickly surpass the resolving power of hexagonal arrays.

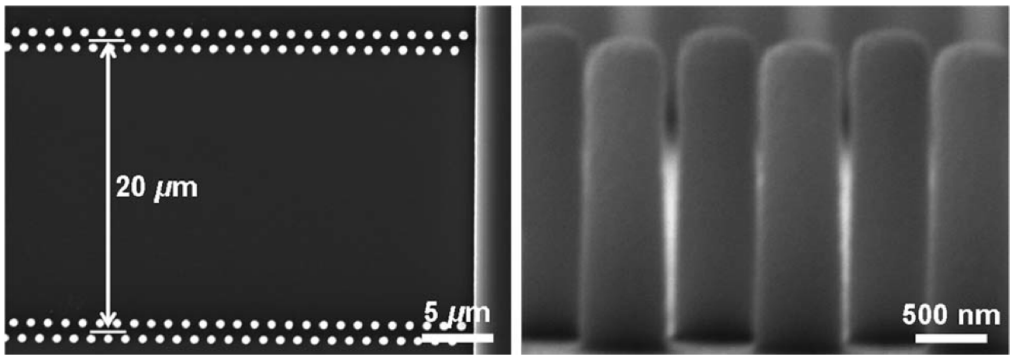

Figure 6.1: Scanning electron microscope (SEM) images of one period of the nanofence array. (a) Top view of the nanofence array with a 20 μm distance between fences. (b) Cross-sectional image of the nanofence array showing the smooth nanopost side walls. The nanoposts are 600 nm in diameter and 2 μm high. The fabrication method is described in Fig. 6.2.

6.2 Experimental

6.2.1 Device fabrication

The silicon nanoposts were fabricated using projection lithography and a deep reactive ion etching (DRIE) process. Fig. 6.2 shows the typical procedure for fabricating a nanofence array in a microfluidic channel starting from a silicon wafer with a 300 nm thermal oxide layer. The mask for the nanofence array consists of 500 fences (500 nm post diameter, 700 nm spacing between adjacent posts, and 20 mm fence-to-fence distance) embedded in a 150 mm wide microchannel with a shifted-T injection (170 mm offset). The assembled microfluidic device is shown in Fig. 6.2g. The uniform diffraction color results from the periodic pattern in the separation channel.

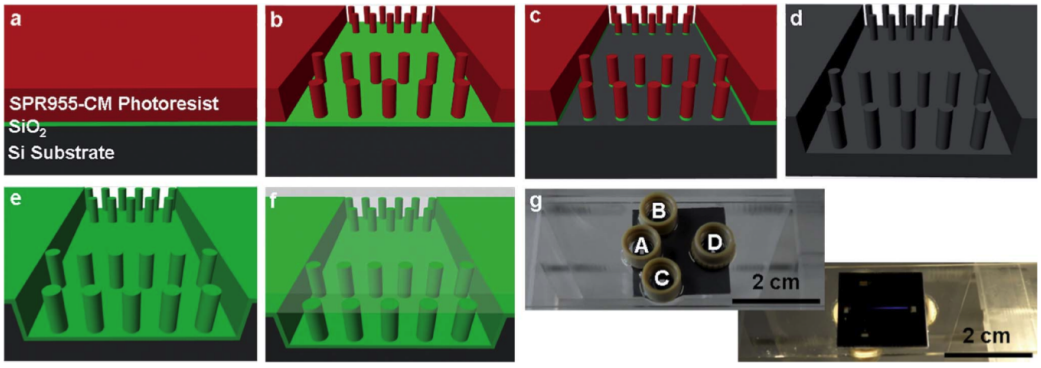

Figure 6.2: Schematic illustration of the typical procedure for fabricating a nanofence array in a microfluidic channel. (a) A 700 nm thick photoresist layer (SPR955-CM, Megaposit) was obtained by spin coating the photoresist solution onto the substrate. (b) The die pattern was transferred to the photoresist using a projection lithography stepper (2500 i3, Canon). (c) The exposed silicon dioxide was removed by reactive ion etching (RIE, STS 320, Surface Technology System) and the remaining post-patterned oxide and photoresist served as the etching mask for silicon DRIE (SLR-770, Plasma-Therm). (d) Silicon posts with a height of 2 μm were obtained after 12 min of etching in $SF_6/C_4F_8/O_2/Ar$ (flow rate of 27/63/10/40 sccm) under a power of 700 W with a dc bias of 60 V and a pressure of 8 mTorr. In order to provide external access to the microchannels, four square openings through the silicon substrate for each die were made by silicon nitride low pressure chemical vapor deposition and KOH wet etching. (e) After stripping the silicon nitride, the silicon substrate was coated with a 120 nm thick layer of thermally grown silicon dioxide for electrical passivation. (f) For the separation experiments, a 500 μm thick borofloat glass wafer was sealed to the frontside of the oxidized silicon wafer using anodic bonding (SB6, Karl Suss). To permit single molecule observations, one wafer was bonded with a 100 μm thick borofloat glass wafer for use with high numerical aperture objectives. The finished devices (12 per wafer) were diced with a wafer saw (DAD 2H/6T, Disco) into approximately 20 mm $\times$ 20 mm pieces. (g) Each piece was bonded on its backside using optical adhesive (Norland Optical Adhesive 81) to a 1 mm thick microscope slide (25 mm $\times$ 75 mm) that had been drilled previously with openings for the reservoirs. Four plastic reservoirs (Upchurch 131 reservoirs) were also mounted to the back of this microscope slide using optical adhesive.

6.2.2 DNA preparation

A stock solution of λ-DNA (48.5 kbp, 20.5 μm stained contour length [37,56, 119], 0.73 μm radius of gyration [90], 500 mg/ml, New England BioLabs) was mixed with XhoI (New England BioLabs) digested λ-DNA fragments. There is a single XhoI restriction site in λ-DNA, leading to 15 kbp (6.3 μm stained contour length, 0.23 μm radius of gyration) and 33.5 kbp (14.2 μm stained contour length, 0.50 μm radius of gyration) digestion fragments. The aforementioned radii of gyration for the digestion fragments were computed from the scaling for a swollen chain [90]. Owing to the stiffness of double-stranded DNA, these radii of gyration for the restriction fragments may be overestimates. Our stock mixture for the DNA separation experiments contains XhoI digest fragments at an approximate concentration of 18 mg/ml and intact λ-DNA at an approximate concentration of 16 mg/ml in 2.2×TBE buffer (196 mM tris base, 196 mM boric acid, 6.2 mM ethylenediaminetetraacetic acid, Sigma). The DNA solution was dyed with YOYO-1 (Invitrogen) at the ratio of one dye molecule per five base pairs by gently rocking the DNA and dye mixture overnight. For the single molecule experiments, the DNA contains either XhoI digestion fragments or intact λ-DNA, dyed with YOYO-1 at the same dye ratio, and diluted to a concentration around 0.1 mg/ml in 2.2×TBE buffer. Before loading the DNA into the chip, the solution was heated at 75°C for 10 min to melt any λ-DNA concatemers to single, linear λ-DNA molecules.

6.2.3 DNA separation experiments

Upon loading de-ionized (DI) water into reservoir D (Fig. 6.2g), the microchannel was wet spontaneously by capillary action. After complete wetting with DI water, the microchannel was filled with a buffer solution of 2.2×TBE, supplemented with 0.07 wt% ascorbic acid, 0.07 wt% polyvinylpy-

rollidone (PVP), and 3 vol% β-mercaptoethanol and submerged in the buffer for 48 h [32]. The chip was mounted on a customized plastic stage with four platinum electrodes connecting the reservoirs to a programmable power supply (HVS-1500, LabSmith). The electric fields were specified by assigning the appropriate potentials at the electrodes based on Kirchoff's law and the assumption that the electrical resistance of each arm is proportional to its length. Prior to loading the DNA, the system was equilibrated by pre-running the chip at 20 V/cm in the separation arm for 30 min. After pipetting the DNA into reservoir B (Fig. 6.2g), the DNA were loaded and injected into the nanofence array using a standard shifted T-protocol [120]. An inverted epifluorescence microscope (DMI-4000, Leica) with a 40×, 0.5 numerical aperture objective (HI PLAN 1, Leica) was used to monitor the progress of the separation. To obtain electropherograms, the smallest rectangular field diaphragm (130×100 μm^2) setting of the microscope was used to limit the field of view and the emitted light was focused onto a photomultiplier tube (H7422-04, Hamamatsu) connected to a data acquisition card operating at 1 kHz. During the electrophoretic run, the stage moved at a speed of 7.0 mm/s between the start and endpoint approximately every 20 s, allowing us to monitor continuously the DNA electrophoresis along the 10 mm separation channel [121]. The experimental system is entirely automated and controlled by a custom LABVIEW program.

To make a quantitative analysis of the separation, we obtained electropherograms at 20 s intervals between scans (25 electrophegrams/run) and fit the electropherograms with a sum of three Gaussian functions. The fits provide the evolution of the peak position, $X(t)$, and its variance, $\sigma^2(t)$, of each species as a function of time. The separation resolution during the experiment can be computed directly from these fitted quantities [70]

$$R_s = \frac{X_2 - X_1}{2(\sigma_1 + \sigma_2)} \tag{6.1}$$

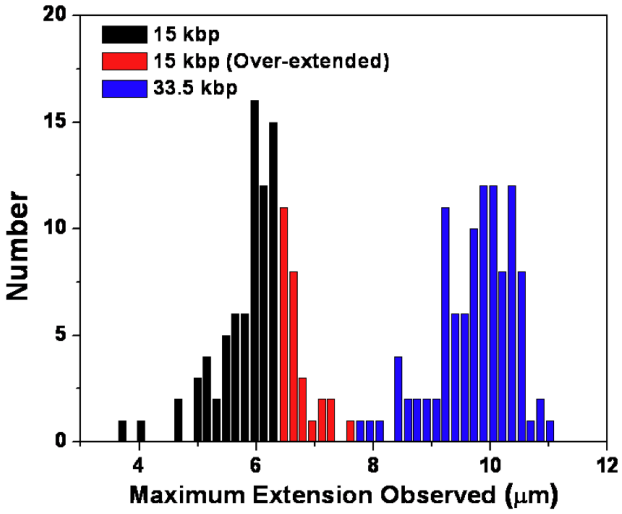

Figure 6.3: Frequency distributions for the maximum extension of the hooked DNA at 10 V/cm for the mixture of 15 kbp and 33.5 kbp DNA. The data in black were definitively identified as 15 kbp fragments and the data in blue were definitively identified as 33.5 kbp fragments. The data in red were tentatively identified as 15 kbp fragments but their extension exceeds the maximum extension of a 15 kbp fragment. The measurements of these short distances are hindered by blooming of the image and streaking of the DNA, so we cannot be certain whether these DNA are strongly extended 15 kbp or weakly extended 33.5 kbp DNA.

where the subscripts refer to the Gaussian peaks corresponding to individual species.

6.2.4 Single molecule experiments

After complete wetting of the microchannel with DI water, the microchannel was filled with the same buffer solution as in the DNA separations. We began with the XhoI digested λ-DNA fragments and determined the size of each observed molecule based on its maximum extension during a collision, as explained in Figs. 6.3 and 6.4. After completing the single molecule

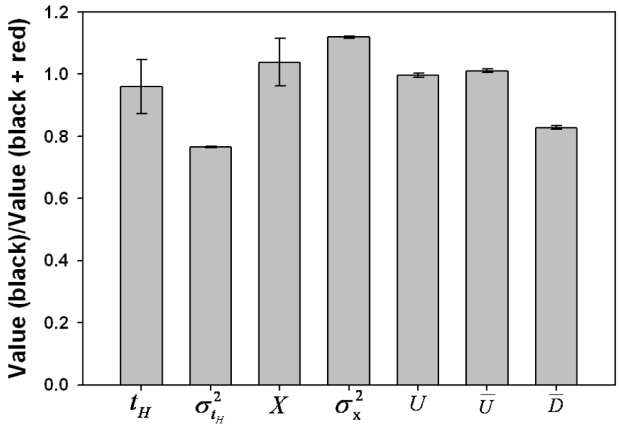

Figure 6.4: In the data analysis, we only include those DNA that can be definitively identified as 15 kbp DNA (the black data in Fig. 6.3). The histogram shows how the various CTRW parameters appearing in Table 6.1 are affected by excluding over-extended 15 kbp molecules from the distribution. The results are presented as the ratio of the data appearing in the main text (black in Fig. 6.3) relative to all potential 15 kbp DNA (black + red in Fig. 6.3). The error bars are the sampling error. The key difference is a reduction in the variance of the holdup time distribution and a corresponding reduction in the predicted dispersion coefficient.

experiments with XhoI digested λ-DNA fragments, the DNA and running buffer were replaced with DI water and the chip was submerged in the running buffer for 48 h before proceeding with the experiments with λ-DNA. During the λ-DNA single molecule experiments, we still observed some smaller DNA. These DNA could be restriction fragments that were not removed from the device during the cleaning or, posssibly, λ-DNA that was sheared during loading. In order to avoid including fragments during λ-DNA analysis, we again estimated the size of every molecule based on its contour length when hooked on the post and only included those that could be λ-DNA. The DNA imaging was performed with an inverted epifluorescence microscope (Leica DMI 4000B). A potential difference of 16 V was applied across the 1.6 cm long channel using platinum electrodes and a Trek power supply (Model

677B), corresponding to an electric field of 10 V/cm. An EM-CCD camera (Photometrics Cascade II) was used to observe single DNAs using a 100×, 1.4 NA oil immersion objective lens (8 bit grayscale pixels and a pixel size of 162 nm). The square viewing widow of width 82.7 μm included 4 nanofences in the channel. Tiff image stacks of 1500 frames at 25 frames per second were captured in the center of the channel (1 mm into the nanofence array).

We used a custom MATLAB-based GUI to track the center of mass and aspect ratio of each DNA identified in the image stack [60]. DNA-post collisions were identified by a delay in the center of mass motion of the DNA molecule. The holdup time of the collision was measured as the time between constant velocity motion of the molecule before and after the collision, as defined previously [60]. The location of each collision was at a specific nanofence as determined from a brightfield image of the nanofence array.

The single molecule data provide probability distributions for the holdup time, t_H, and the number of rows between collisions, N_{Row}. In addition to using these data to analyze the microscale transport in the device, we can also use them to calculate the mean velocity and dispersion coefficient for transport inside the nanofence array (i.e., neglecting the contributions due to injection and detection) using a previously developed continuous-time random walk (CTRW) model [83]. Briefly, we treat the DNA molecule as a particle moving in one dimension. The particle can be in one of two states: (i) colliding with a nanofence for a random time t_H, resulting in no translation of the center of mass of the molecule, or (ii) translating at a steady velocity, U, between collisions over a random distance x, which is obtained from the random number of rows between subsequent collisions, x(μm) = 20 N_{Row}. The corresponding mean velocity is

$$\bar{U} = \mu E = \frac{\langle x \rangle}{\langle t_H \rangle + \frac{\langle x \rangle}{U}} \tag{6.2}$$

and the dispersion coefficient, $\bar{D}$, is given by

$$\bar{D} = \frac{\sigma_x^2 \left(1 - \frac{\bar{U}}{U}\right)^2}{2\left(\langle t_H \rangle + \frac{\langle x \rangle}{U}\right)} + \frac{\bar{U}\sigma_{t_H}^2}{2\left(\langle t_H \rangle + \frac{\langle x \rangle}{U}\right)} \tag{6.3}$$

where σ_i^2 is the variance in random variable i. We write Eq. 6.3 in this slightly longer form to emphasize the separate contributions due to the random distance between collisions (first term) and the variance in the collision times (second term).

6.3 Results and discussion

6.3.1 Separation resolution

Figures 6.5 and 6.6 show the detailed evolution of an electrophoretic separation of the mixture of λ-DNA and its XhoI digest at an electric field of 10 V/cm. Two bands become visible along the separation channel after 45.0 s, with the slower band corresponding to a mixture of the 33.5 kbp and 48.5 kbp species and the faster band being the 15 kbp fragment. The mixture of 33.5 and 48.5 kbp starts to separate after 157.0 s and all three bands are further resolved with the passage of time. After 7 min, the resolution in Fig. 6.5 between the 15 and 33.5 kbp fragments is 1.15, and the resolution between the 15 and 48.5 kbp fragments is 1.91.

We also tested the nanofence array at a higher electric field (Fig. 6.7). At 20 V/cm, two distinct bands are again resolved after 45.0 s. The slower band, consisting of the 33.5 and 48.5 kbp fragments, begins to separate into two bands after 201.8 s, but the resolution at the end of the array is inferior to the results we obtained at 10 V/cm. Based on the detailed single molecule

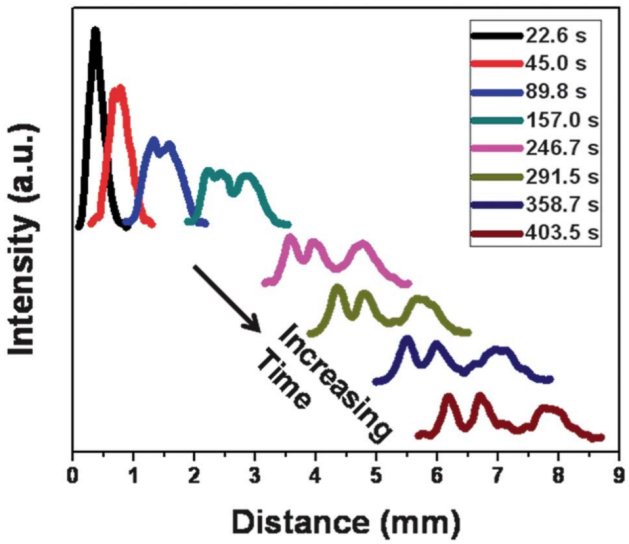

Figure 6.5: Evolution of the bands during DNA electrophoresis at 10 V/cm. Multiple scans of the separation channel are acquired at different times during the run, making it possible to monitor the continuous separation of λ and the XhoI λ-digest.

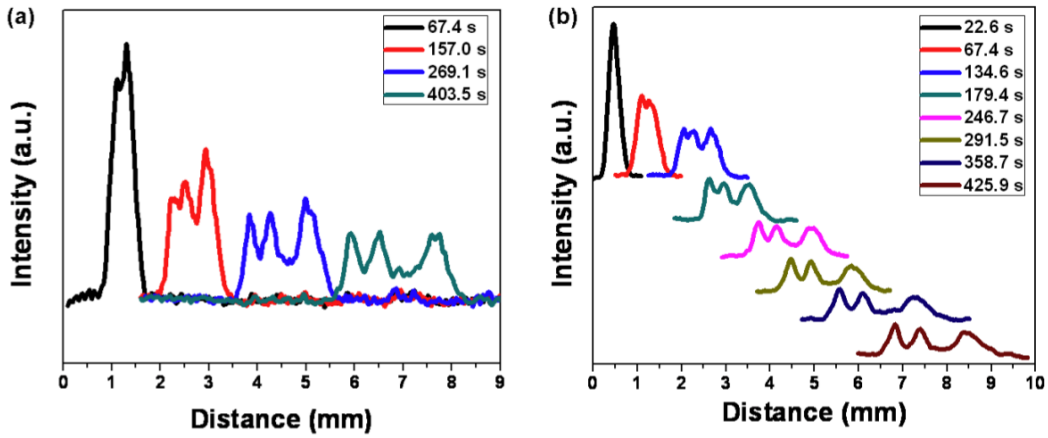

Figure 6.6: Evolution of the bands for two different sets of DNA electrophoresis at 10 V/cm. Each experiment used the same scanning interval but only selected data are included here for clarity.

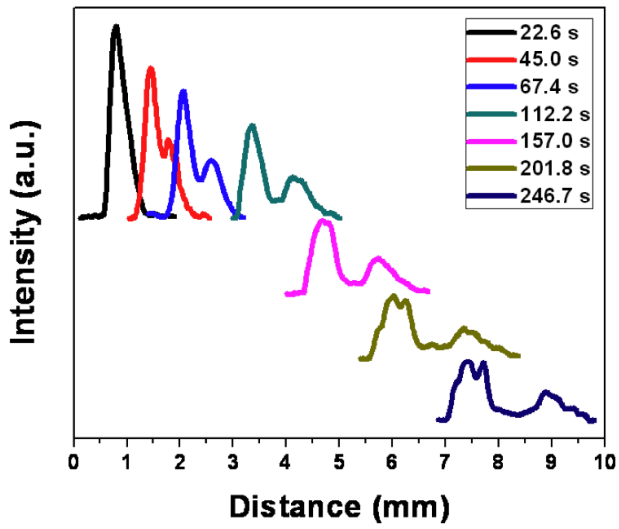

Figure 6.7: Evolution of the bands during DNA electrophoresis at 20 V/cm. Three distinct peaks start to be resolved after 201.8 s.

study at 10 V/cm described in the following subsections, we propose that the reduced resolution at 20 V/cm is due to incomplete relaxation of the DNA between collisions. Thus, as the electric field increases further, the resolution in the particular nanofence design in Fig. 6.1 should continue to decrease.

Figure 6.8 shows the evolution of the separation resolution at 10 V/cm as a function of time, averaged over three separate experiments. Compared with other types of microfluidic devices, the nanofence array quickly separates the mixture of λ-DNA and its XhoI digest with high resolution. For example, in self-assembled magnetic beads a lower electric field (4.8 V/cm) and around 15 min was required to obtain a similar resolution to Fig. 6.8 [64]. The nanofence also exhibits superior resolution compared to a previous device produced by projection lithography; the latter hexagonal nanopillar chip with a post diameter and a post spacing of 500 nm only led to a resolution of 0.8 between 21 kbp and 165 kbp fragments after 15 min [46,61]. Separations

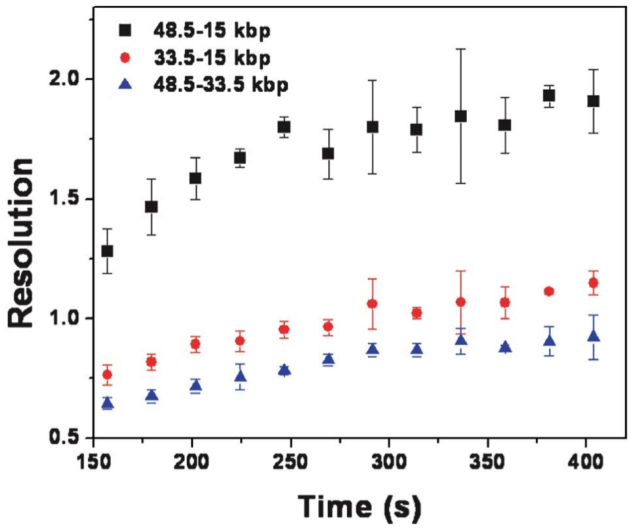

Figure 6.8: Plot of the separation resolution at 10 V/cm. Error bars represent the standard deviations for the different data sets in Figs. 6.5 and 6.6.

in a hexagonal array of 360 nm posts with a 3 μm center-to-center distance at 10 V/cm required around 20 min to achieve a resolution of 2.15 between 15 and 33.5 kbp fragments [62]. Using the $t^{1/2}$ scaling for the resolution [70], this corresponds to a value of 1.2 after 7 min, comparable to the nanofence array. Although there are no data for the XhoI λ-digest in dense nanopillar arrays fabricated from electron-beam lithography (EBL) [48] and nanoimprint lithography (NIL) [52], the data available for separating 10 kbp and 38 kbp fragments [48] lead us to speculate that dense nanopillar arrays will exhibit a somewhat higher separation resolution than the nanofence. However, from a fabrication standpoint, EBL is limited to short separation matrices and requires long processing times because of the serial nature of the fabrication procedure. NIL is an alternative choice for mass-production, but it is still limited by the need to make the mold by EBL and by challenges in transferring the pattern over the large areas required for separations [122]. In contrast, our approach using projection lithography allows high-throughput, easy, wafer-scale fabrication of devices for rapid, sharp separations of long

DNA.

6.3.2 Do the DNA collide with each nanofence?

The underlying principle of the nanofence is to enforce regularly spaced collisions. Realizing this goal requires that the gap between the posts be small enough to prevent the DNA from squeezing through without a collision. Since we also wanted to minimize the cost of the device, we chose to use projection lithography to pattern the device. Our projection lithography system has a line width of 500 nm, which sets the lower bound on both the post diameter and the spacing between the posts. To maintain a small gap, we used two offset rows of posts to create each nanofence.

From a fabrication standpoint, it appears that we met our design criteria. As one would expect, the dry etching and the thermal oxidation processes affect the gap between nanoposts and the post diameter in the finished device. After DRIE, the diameter of the etched silicon nanoposts is about 360 nm due to undercutting (Fig. 6.9). After the thermal oxidation step, the diameter of the oxidized silicon nanoposts increased to 600 nm (Fig. 6.1b), giving a post radius commensurate with the 230 nm radius of gyration of the 15 kbp fragment. At the same time, the gap between the posts projected onto a plane with its normal vector parallel to the direction of motion, 100 nm, is small compared to the radius of gyration of the smallest DNA in our separation.

From an operational standpoint, DNA transport in the device is more complicated than we initially expected. To see if the DNA actually collided with each nanofence, we measured the probability distribution for the number of rows between collisions at 10 V/cm, conditioned on colliding in the first row of the viewing window. We chose to condition on a collision in the first row to obtain the most reliable statistics for the limited viewing window (a square

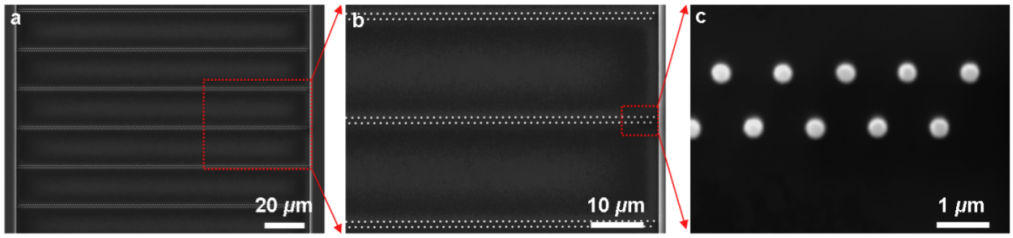

Figure 6.9: SEM images of the silicon nanofence array after the silicon etching process (Fig. 6.2d). The diameter of silicon posts was 360 nm, which was 140 nm smaller than the patterns from the stepper mask due to undercutting during the dry etching process.

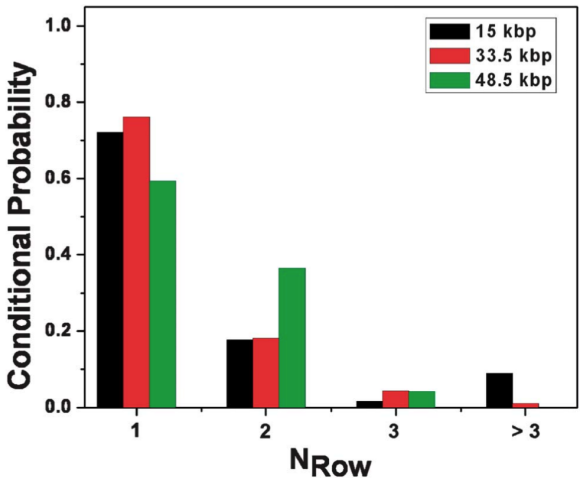

Figure 6.10: Probability distribution for the collision at a given row conditioned on colliding with the first nanofence in the viewing area. The histogram shows the probability of a DNA molecule that collides with the first fence to make its next collision with the second fence ($N_{Row} = 1$), third fence ($N_{Row} = 2$), fourth fence ($N_{Row} = 3$), or some later fence ($N_{Row} > 3$) outside of the viewing area. The experiments were carried out at an electric field of 10 V/cm.

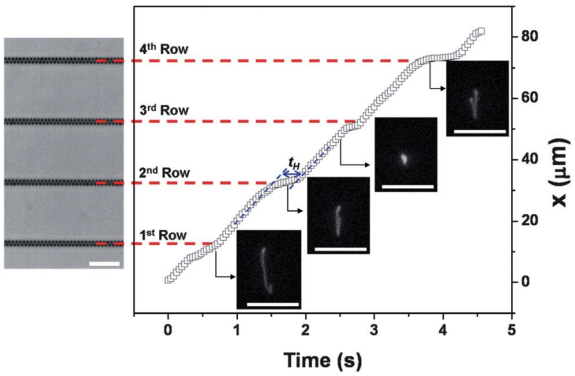

Figure 6.11: Trajectory of the center of mass of a 33.5 kbp DNA at 10 V/cm. There are four nanofences in the viewing window of 82.7 μm. Four images of a 33.5 kbp DNA during migration in the nanofence array are included, with the direction of motion being from bottom-to-top (corresponding to the bright field image). The DNA moves at constant free solution migration velocity before and after collisions (blue dotted lines). Scale bars = 10 μm.

with width = 82.7 μm) available to us for single molecule imaging with a high numerical aperture objective. While the data in Fig. 6.10 do not indicate a unit conditional probability $P(N_{Row} = 1) = 1$ for any of the DNA sizes, $P(N_{Row} = 1) + P(N_{Row} = 2) \approx 1$ for all of the DNA sizes. The best results were obtained for the 33.5 kbp DNA, as we can see from the exemplary trajectory in Fig. 6.11. The conditional collision probability for the 33.5 kbp DNA appears to decay exponentially with a constant of 76.2%, and only 1 of the 101 molecules that collided in the first row exited the viewing window without a second collision. For the smaller 15 kbp DNA, most of the DNA make their next collision in the subsequent row, but 6 out of the 68 molecules exited the observation window without making a second collision. Although the gap between posts is small, the porosity of a fence is still limited by the projection photolithography to 33% (measured from the entrance to the exit of a nanofence in the direction of net motion). Apparently the combination of this porosity and thermal fluctuations of the 15 kbp DNA coil, along with deformation caused by the non-uniform electric field near the posts, is suffi-

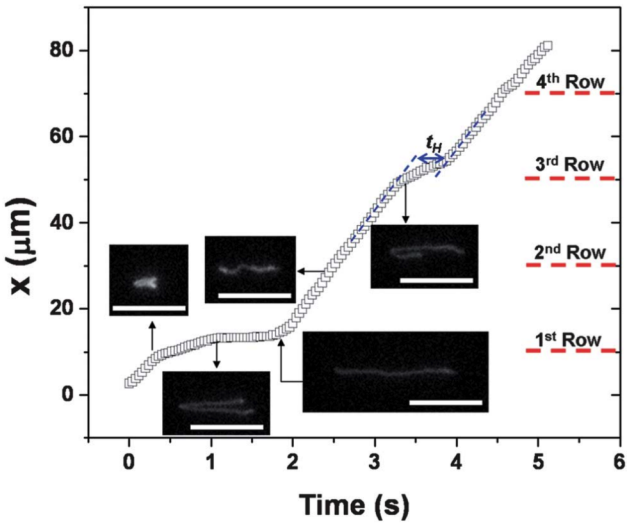

Figure 6.12: Trajectory of the center of mass of a λ-DNA molecule at 10 V/cm. The λ-DNA is highly extended and does not always have enough time for complete relaxation before next collision, which for this particular trajectory results in reptation through the second nanofence array. Five images of a λ-DNA during migration in the nanofence array are included, with the direction of motion being from left-to-right. The DNA moves at constant free solution migration velocity before and after collisions (blue dotted lines). Scale bars = 10 μm.

cient to allow occasional passage of these small DNA through the nanofence. In contrast, all of the 96 observed λ-DNA molecules collided within the observation window. However, we found that the incomplete relaxation after the collision leads to 40.6% of the molecules slithering through the next row of posts without a collision. (See Fig. 6.12 for an exemplary trajectory.) The slow relaxation is offset by a large radius of gyration, whereupon a vast majority (89.7%) of the λ-DNA molecules that reptated through the first nanofence collided with the second nanofence.

6.3.3 Continuous-time random walk model

The CTRW model described in Eqs. 6.2 and 6.3, combined with probability distributions obtained from single molecule experiments, is the most straightforward way to analyze the role of the post geometry on band broadening. In this approach, we assume that the region of the nanofence array probed by the single molecule experiments is representative of the rest of the array; i.e., that there are no defective fences or changes in the surface zeta potential that could impart a non-uniform electroosmotic flow elsewhere in the channel. Under these assumptions, the CTRW equations readily provide the rate of growth of the width of the bands as a function of time solely due to the interactions between the DNA and the fences. In contrast, extracting the same data from electropherograms such as the ones in Fig. 6.5 is considerably more challenging. While we can easily estimate the position of the peaks, $X_i(t)$, by visual inspection of the electropherogram, the corresponding measurements of the peak variances, $\sigma_i^2(t)$, are hindered by the absence of a unique deconvolution of the electropherogram into the sum of three Gaussians. Moreover, the signal-to-noise ratio begins to affect the measurements of the peak widths towards the end of the experiment. Indeed, the signal-to-noise ratio also limits the resolution we can obtain in our separations.

However, in order to use the CTRW model to compare the dispersion in a nanofence array to the hexagonal array, we should first check if the CTRW model predictions agree with the separation data. The form of Eq. 6.2 is a simplification of the general result 5.1 for the case where the DNA velocity, U, between collisions in the direction of the net motion is a constant, as suggested by Figs. 6.11 and 6.12. As we see in Table 6.1, this "in-array" free solution mobility was essentially independent of the DNA molecular weight. We can then compute the average velocity and dispersion coefficient by determining the parameters in Eqs. 6.2 and 6.3 from the distribution for the distance between collisions (Fig. 6.10) and the distribution for the holdup

Table 6.1: CTRW parameters measured from single-molecule data at 10 V/cm. The first three columns correspond to the data obtained here for the nanofence array. The data in the last column are from single-molecule experiments in hexagonal array of 1 μm diameter posts with a 3 μm pitch. The latter experiments are described in Chapter 4. The in-array free solution velocity, U, is the average of the slopes of the trajectories (e.g., Fig. 6.11 and 6.12) for all molecules and the error corresponds to the standard deviation of this ensemble. The errors for the mean velocity and dispersion coefficient are estimates of the sampling error for the distributions for the holdup time and the variance, propagated through Eqs. 6.2 and 6.3.

	15 kbp	33.5 kbp	48.5 kbp(nf)	48.5 kbp(hex)
U (μm/s)	23.5 $\pm$ 1.7	24.0 $\pm$ 1.5	23.0 $\pm$ 2.0	14.9 $\pm$ 0.9
t_H (s)	0.26	0.40	0.54	0.34
$\sigma^2_{t_H}$ (s^2)	0.04	0.08	0.22	0.08
X (μm)	29.4	25.9	29.0	18.5
σ^2_x (μm^2)	323.2	140.4	133.6	150.7
$\bar{U}$ (μm/s)	19.4 $\pm$ 0.09	17.6 $\pm$ 0.06	16.1 $\pm$ 0.38	11.7 $\pm$ 0.05
$\bar{D}$ (μm^2/s)	8.00 $\pm$ 0.06	12.0 $\pm$ 0.03	19.4 $\pm$ 0.4	5.7 $\pm$ 0.03

times (Fig. 6.13). The data appearing in Fig. 6.13 are reminiscent of the cumulative distribution function for a gamma distribution, which we might expect for collisions with an isolated nanopost [35]. However, we found that the average collision time in the nanofence appears to be somewhat longer-lived than equivalent data for isolated nanoposts [35]. To estimate the average distance between collisions and its variance from Fig. 6.10, we assumed that any DNA in the $N_{Row} > 3$ category collided at $N_{Row} = 4$; as there are very few DNA that fail to collide in the viewing window, their collisions contribute little to the mobility and dispersivity from the CTRW model. The relevant statistics from the single molecule experiments are summarized in Table 6.1, along with the corresponding predictions for the mean velocity and the dispersion coefficient.

The CTRW results for the average velocity agree with the separation experiments. To obtain the latter data, we used the average of the peak positions,

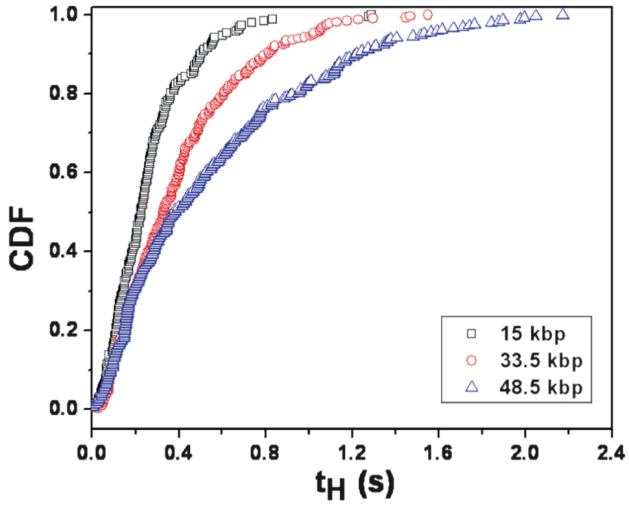

Figure 6.13: Cumulative distribution function (CDF) of the holdup time for each molecular weight at 10 V/cm.

$X(t)$, from three separate experiments at 10 V/cm and then computed the velocity from linear regression (Fig. 6.14). The corresponding velocities (19.9 $\pm$ 0.08, 17.2 $\pm$ 0.06, and 16.0 $\pm$ 0.07 μm/s for the 15 kbp, 33.5 kbp and 48.5 kbp DNA) are in excellent agreement with the CTRW results in Table 6.1.

We also checked to see whether the band broadening predicted from the CTRW model agrees with the data from the separation experiments. Fig. 6.15 shows the variance data for one run; the data for the other runs are shown in Fig. 6.16 and 6.17. The difficulty in obtaining accurate values of the peak width from the deconvoluted electropherograms is apparent in Fig. 6.15; the variance should increase monotonically but the data are scattered about a general increase in width. Fig. 6.15 also includes estimates for the band broadening from the CTRW dispersion coefficients appearing in Table 6.1. Since we do not know the initial width of the band due to the injection, we fixed the slope as twice the dispersivity and chose the intercept to minimize the sum-squared error between the separation data and the CTRW

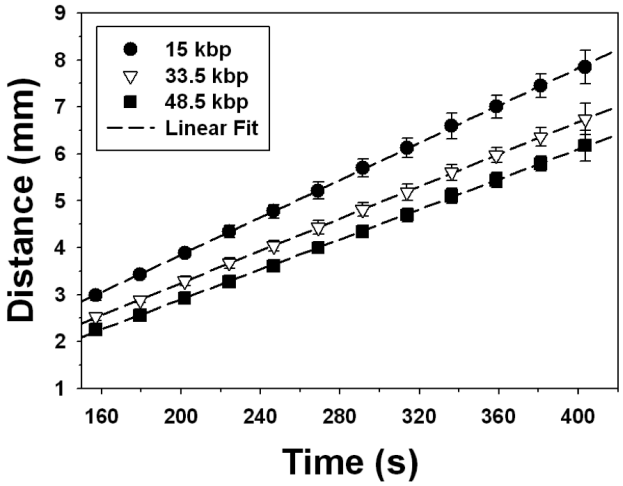

Figure 6.14: Migration distance as a function of time. Error bars represent the standard deviations for three different data sets. The linear equations fit the data with negligible standard errors on the order of 10^{-5}. The equations for fitting the data are $X(t) = 0.0199\ t$ - 0.126 for the 15 kbp DNA ($R^2 = 0.999$), $X(t) = 0.0172\ t$ - 0.182 for the 33.5 kbp DNA ($R^2 = 0.999$), and $X(t) = 0.0160\ t$ - 0.300 for the 48.5 kbp DNA ($R^2 = 0.999$).

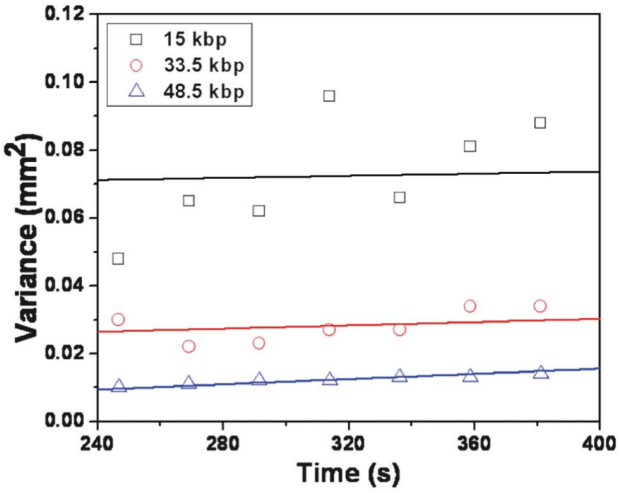

Figure 6.15: Variance of the peaks during the separation as a function of time and the comparison with the prediction of the single-molecule data for 15 kbp, 33.5 kbp and 48.5 kbp. The intercept for the single-molecule data is the best fit of a line with slope of twice the dispersion coefficient in Table 6.1 to the separation data.

prediction.

For the larger DNA, the agreement between the CTRW predictions and the experimental data is quite good, especially considering the error in extracting the variance from the separation data. The agreement is not as good for the 15 kbp DNA. We did not find that the disagreement was due to the limited statistics in Fig. 6.10 and 6.13, since we had to alter the single molecule data in an unrealistic manner to fit the separation data. We can also exclude fragmentation of the DNA as an explanation, since this would lead to a band of non-colliding small fragments moving at the free solution mobility that do not appear in the electropherogram. We ultimately concluded that the relatively low signal-to-noise ratio during detection of the bands in the separation is the most likely explanation for the discrepancy between the CTRW predictions for the band broadening of the 15 kbp DNA and the peak widths we extracted from the electropherogram. Our explanation is

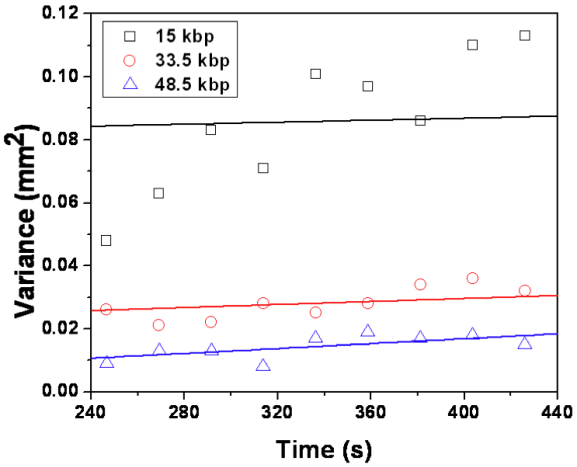

Figure 6.16: Variance of the peaks during the separation as a function of time and the comparison with the prediction of the single-molecule data for (a) 15 kbp, (b) 33.5 kbp and (c) 48.5 kbp (trial #2, Fig. 6.6a). The intercept for the single-molecule data is the best fit of a line with slope of twice the dispersion coefficient in Table 6.1 to the separation data.

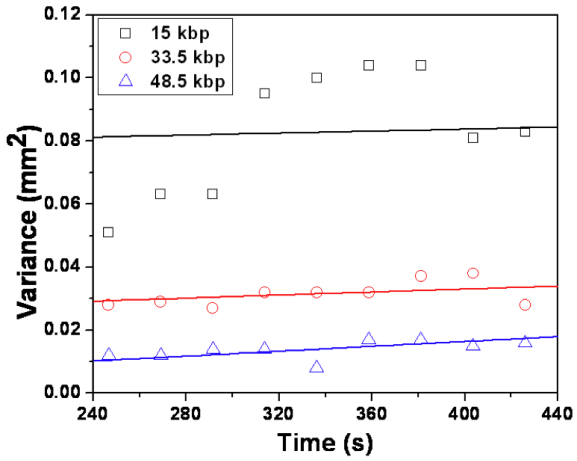

Figure 6.17: Variance of the peaks during the separation as a function of time and the comparison with the prediction of the single-molecule data for (a) 15 kbp, (b) 33.5 kbp and (c) 48.5 kbp (trial #3, Fig. 6.6b). The intercept for the single-molecule data is the best fit of a line with slope of twice the dispersion coefficient in Table 6.1 to the separation data.

supported by two features of the electropherogram for the 15 kbp peak. First, while the 48.5 and 33.5 kbp peaks are reasonably Gaussian, the 15 kbp peak is highly non-Gaussian. The sum of a weak Gaussian peak and random noise from the detector gives a non-Gaussian result. Second, the area under the 15 kbp peak is much larger than one would expect from an XhoI digest of λ-DNA. Assuming a stoichiometric dye ratio and uniform detection of the fluorescence, we would have expected the area of this 15 kbp peak to be $\sim$45% of the area under the 33.5 kbp peak. As we can see in Fig. 6.5, this is clearly not the case.

6.3.4 Comparison with a hexagonal array

We are now in a good position to evaluate our initial hypothesis that the nanofence reduces the band broadening compared to a hexagonal array. In Chapter 4, we obtained the probability distributions for the holdup time and distance between collisions for λ-DNA at the same electric field (10 V cm^{-1}) in a hexagonal array of 1 μm diameter posts with a 3 μm pitch. Table 6.1 includes the in-array free solution velocity, U, mean and variance of the probability distributions, and the predictions of Eq. 6.2 for the mean velocity and Eq. 6.3 for the dispersion coefficient of λ-DNA.

Remarkably, the dispersion coefficient for λ-DNA in the nanofence array is a four-fold increase over a hexagonal array. The latter result contrasts sharply with our expectation that, by enforcing uniform distances between collisions, the dispersion in the nanofence array would be smaller than the dispersion in a hexagonal array. The CTRW model provides ready insights into the origin of the increased dispersion. Equation 6.3 provides two distinct sources to the band broadening; the first term is the contribution due to the distance between collisions and the second term is the contribution due to the collisions themselves [83]. Both terms are normalized with the average time for a collision-translation cycle. While the nanofence array did not

enforce uniform collision distances, the variance in the collision distance, σ_x^2, is indeed lower in the nanofence array. However, the first term in Eq. 6.3 is 3.35 μm^2/s in the nanofence array, compared to 2.23 μm^2/s in the hexagonal array. As the total cycle time, $\langle t_H \rangle + \langle x \rangle / U$, is longer in the nanofence array, we can conclude that the increase in dispersion due to the variance in the distance between collisions arises from an increase in the difference between the mean DNA velocity and its velocity between the collisions. In other words, the collisions in the nanofence array are more efficiently retarding the DNA. Such an effect is obviously desirable for separating the peaks, but it has a deleterious effect on the band broadening. Indeed, even if the nanofence worked perfectly with $\langle x \rangle = 20$ μm and $\sigma_x^2 = 0$, the dispersion coefficient would still be substantial (5.56, 8.82, and 15.9 μm^2/s for the 15, 33.5 and 48.5 kbp DNA). All of these values exceed the dispersion coefficient of λ-DNA in the hexagonal post array.

Since the band broadening in the nanofence array is actually higher than in a hexagonal array, inspection of Eq. 6.1 reveals that the resolution in the nanofence array must be due to the separation between the peaks. Between collisions in the nanofence, the DNA relax and translate through an empty channel under a uniform electric field. In contrast, DNA moving in a hexagonal array experience a complex electrophoretic "flow" field, consisting of regions of compression and extension along with substantial steric hindrances caused the presence of nearby posts. The difference between these two types of electric field distributions is readily apparent in the in-array free solution velocity U in Table 6.1. Although both experiments correspond to the same potential drop per over the array length, $\Delta V / \Delta L = E$, the apparent speed *in the direction of this potential drop* is much lower in the hexagonal array due to the curved field lines [58]. The interfence transport in the nanofence array leaves the DNA in a conformation that favors collisions. This favorable conformational effect is enhanced by the high local density of posts in the nanofence array, whereupon a DNA molecule approaching a

nanofence is always reasonably aligned with one of the posts (*i.e.*, the impact parameter [33] is small). In contrast, collisions in a hexagonal post array occur over a wide range of impact parameters. The combination of these two effects leads to stronger stretching on the post. Indeed, the mean extension of the hooked λ-DNA in the nanofence at 10 V/cm was 15.2 ± 2.6 μm, which is significantly longer than the typical value of 9.4 μm in the hexagonal array at the same electric field [60].

6.4 Conclusions

While we initially expected that the unique geometry of the nanofence array would reduce the band broadening compared to a regular post array without reducing the nominal collision frequency, our single molecule data and CTRW modeling led to the opposite conclusion. Rather, the resolution in the nanofence array is the result of more efficient collisions due to the absence of conformational changes caused by the electric field gradients and steric obstacles in a hexagonal post array. As our device is a prototype, we expect that the resolution can be enhanced further. As we now know that the device operates by ensuring high-quality collisions with the obstacles, we expect that the performance might be improved by ensuring that all of the DNA are completely relaxed prior to colliding. In particular, there are a substantial number of λ-DNA that reptate through the first row of posts following a collision before colliding in the second row. We suspect that a number of the λ-DNA collisions are partially relaxed molecules that are arrested during their reptation through the nanofence or instances of the bunching instability [77, 78].

There are two possible routes to increasing the time between collisions and thus ensuring complete relaxation: (i) We could reduce the electric field so that it takes more time to move between fences with the same distance

between fences. While this approach is a simple remedy to the problem, since it does not require any change in the device geometry, it is of limited utility since the electric field still needs to be strong enough to deform the DNA when it collides with an obstacle. Reducing the electric field also will increase the number of roll-off collisions for the smaller DNA, thereby reducing the efficiency of the separation. (ii) We could increase the distance between fences while keeping the electric field fixed. While this second solution will certainly allow the λ-DNA to relax before the subsequent collision while providing sufficient electrical force to deform the DNA during a collision, it increases the footprint of the device. It is not obvious that increasing the time between collisions will actually lead to an improved separation since, by definition, the same number of collisions will now require more time. The challenges related to relaxation will only increase as the size of the DNA increases. Indeed, we could reach the point where the fence spacing is so long that we need to introduce turns into the separation channel, which can introduce substantial band broadening [71]. In the most extreme case, the time between collisions could be much longer than the nominal collision time, at which point the separation would vanish. Owing to the non-trivial cost of fabricating next-generation prototypes, the nanofence is an ideal candidate for optimization through simulation, provided that we can identify a suitable DNA model that resolves the relatively small post size and the long DNA contour length.

Chapter 7

Experimental study of the effect of disorder on DNA dynamics in post arrays during electrophoresis

This chapter is based on a pending publication:
D. W. Olson, and K. D. Dorfman
Physical Review E.

7.1 Introduction

Two dimensional arrays of micron-sized cylindrical posts are proven to rapidly separate long DNA under a dc electric field [46,48,49,52,59,62,64,65]. While the application of a dc electric field using the standard separation matrices (polyacrylamide or agarose gels) fails to produce a size dependent mobility for long DNA ($\gtrsim$10 kbp) [7], the increased pore size of microfabricated ar-

rays results in a size dependent mobility for long DNA. Repeating a regular pattern of posts over a large distance in a microfluidic channel is one method for producing the requisite post array geometry [45, 46, 48, 49, 52, 59, 62, 118]. Alternatively, self-assembled magnetic bead arrays, formed by the application of a magnetic field to a suspension of super-paramagnetic beads in a microfluidic channel, also produce the necessary geometry to separate long DNA by size [64, 65]. In both types of arrays, DNA collides with the individual posts of the array and disengages with a time that depends on the size of the DNA molecule [30, 37, 66]. A schematic of DNA colliding with the posts of the array is shown in Fig. 7.1. Significant spatial separation of different species requires many collisions during transport in the device [30].

Initial simulations of DNA transport in ordered and disordered post arrays using a 2D bead-rod model suggested that disordered post arrays result in lower electrophoretic mobility than ordered square and hexagonal arrays [76]. In the ordered arrays, DNA molecules migrate in the 'channel' between the edges of posts, which leads to fewer DNA-post collisions. Further simulations, using a 3D bead-spring model for DNA, also found that very few collisions occur in an ordered post array [75]. The dispersion coefficient in ordered arrays thus approaches the free solution diffusion coefficient of the DNA as there are very few DNA-post collisions. The results of these studies suggested that disordered arrays are essential to size separation due to an increased collision probability. It should be noted that both studies neglected perturbations to the electric field caused by the presence of the posts. These perturbations are shown in Fig. 7.1 for the geometries used in the present study.

In contrast to the predictions of these simulations, the experimental observations in Chapter 4 showed that frequent DNA-post collisions *do* occur in an ordered array at this post density [58]. Moreover, Brownian dynamics simulations that included the perturbations in the electric field caused by insulating posts matched the experimentally measured electrophoretic mo-

bility [58, 60], indicating that the disturbance in the electric field due to the posts qualitatively alters the transport in this relatively tight array. These experiments and simulations showed that DNA makes enough collisions in an ordered array to yield a size based separation [83]. However, it is still unclear whether an ordered or disordered array will be superior for long DNA separation. Since Brownian dynamics simulations of DNA transport in post arrays have given conflicting results on the utility of ordered arrays, an experimental study is necessary to definitively determine the role of order in post arrays. In the following, we examine the role of disorder on the transport properties of long DNA, thereby providing a fundamental basis to determine the role of disorder on DNA size separation.

The two most important measures of separation efficacy are the time to conduct the separation and the resulting separation resolution. The separation resolution is defined as

$$R_s = \frac{\Delta\mu}{\langle\mu\rangle}\sqrt{\frac{L}{16H}}, \tag{7.1}$$

where $\Delta\mu$ is the difference in electrophoretic mobility between two species, $\langle\mu\rangle$ is their average mobility, L is the length of the separation device, and H is the plate height. The plate height is a macroscopic measurement of microtransport properties and can be written as $H = 2\bar{D}/\bar{U}$, where $\bar{D}$ is the dispersion coefficient in the array and $\bar{U}$ is the averaged velocity in the array. We are interested here in determining whether the factors appearing in Eq. 7.1, namely the electrophoretic mobility and the plate height, are affected by disorder in the array. As such, it proves sufficient to study the dynamics of a single DNA size with a molecular weight typically used in the separations. In this manner, we can unambiguously ascertain the changes in electrophoretic mobility and plate height without introducing artifacts inherent in multicomponent data, such as deconvolving overlapping peaks. We thus measured the electrophoretic mobility of λ DNA (48.5 kbp) in an ordered post array and a disordered post array to determine whether the

mobility depends on the array type. Observations of DNA-post collisions in each array type revealed the cause of the deviation between the free solution mobility and the mobility inside the array. As shown in Eq. 7.1, resolution is maximized by minimizing plate height. We thus measured the plate height of a single species in both array types and determined the underlying causes of band broadening from single molecule observations. Because the time to conduct the separation is directly proportional to the applied electric field, we further measured DNA velocity and band broadening over a wide range of electric fields. Based on our measurements, we provide guidelines for optimizing the array and electric field.

7.2 Materials and Methods

The ordered array in Fig. 1A consists of 1 μm diameter cylindrical posts with a 5 μm center-to-center spacing in a regular hexagonal pattern. To create the disordered array in Fig. 1B, we allowed each post of the regular hexagonal array to undergo a short random walk consisting of $n = 15$ steps with a distance of $d = 0.5$ μm and a random angle. We characterized the disorder of the array by the dimensionless dispersion of the array, s, that corresponds to the deviation of the array from a regular hexagonal array [66]. For the random walk described above, the dispersion of the array is given by

$$s = \frac{d}{a}\sqrt{n}, \tag{7.2}$$

where $a = 5$ μm is the center-to-center spacing of the ordered array. Using Eq. 7.2, the theoretical dispersion of the disordered array is $s = 0.387$. The parameters for the random walk were chosen to provide substantial disorder in the array while keeping the posts far enough from each other to allow fabrication of individual posts.

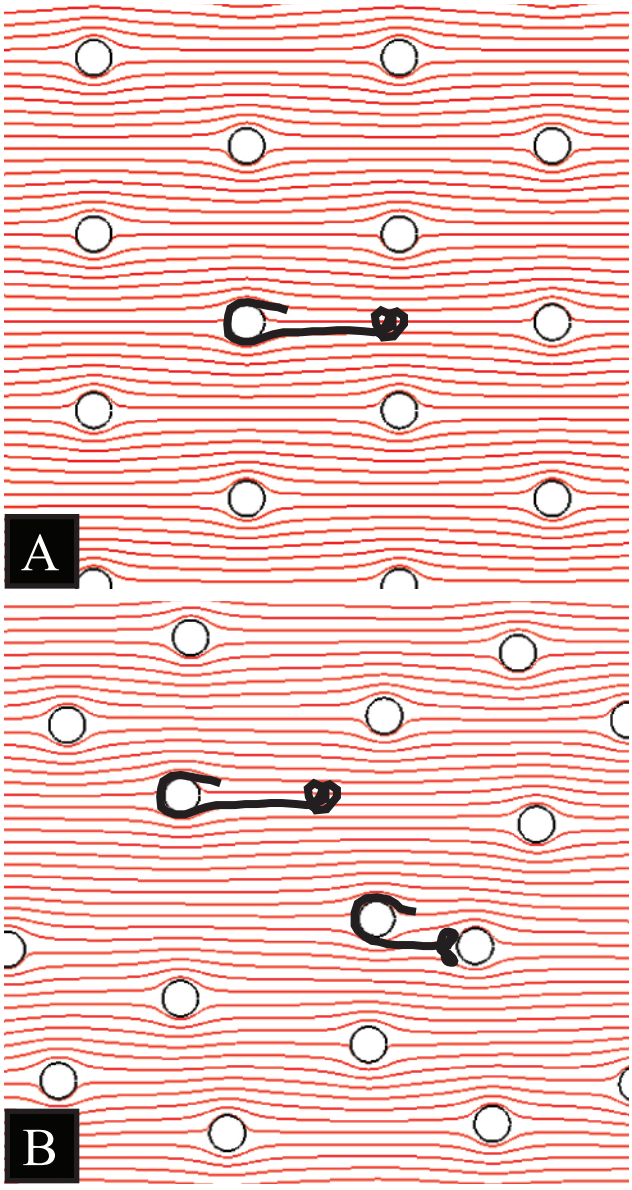

Figure 7.1: Schematic of a DNA molecule colliding in the ordered array (A) and DNA molecules colliding in the disordered array (B). In the disordered array, DNA can collide with an isolated post or with multiple posts in a single collision event. Red lines approximate the electric field lines in each array.

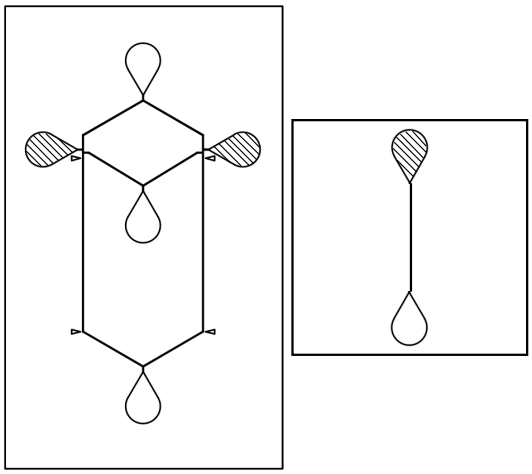

Figure 7.2: Schematics for the devices used in the experiments. The 5-reservoir chips is shown on the left, and the 2-reservoir chip on the right. DNA is loaded into the hashed reservoirs and driven through the device by an applied electric field. The 5-reservoir chip contains the ordered array in the left channel and the disordered array in the right channel. Post arrays span the channel between the arrows. 50 rows of the ordered array and disordered array are placed in the 2-reservoir array.

7.2.1 Single Molecule Experiments in a 2-Reservoir Device

We fabricated a 2-reservoir device with 50 rows of an ordered array and 50 rows of a disordered array in series. The two arrays were separated by a post free region 2 mm long. The device is shown schematically in Fig. 7.2. We fabricated the device in oxidized silicon using projection lithography following a procedure described previously [63]. We characterized the chip by SEM (Fig. 7.3A,B) after oxidation to confirm that each post has a diameter of 1 μm and to make the measurement of the disorder of each array described above. The oxidized wafer was bonded to a 100 micron thick BOROFLOAT wafer (Mark Optics) by anodic bonding at 450°C and 1800 V. We scored and cracked the wafer into individual devices. The sealed channel was attached

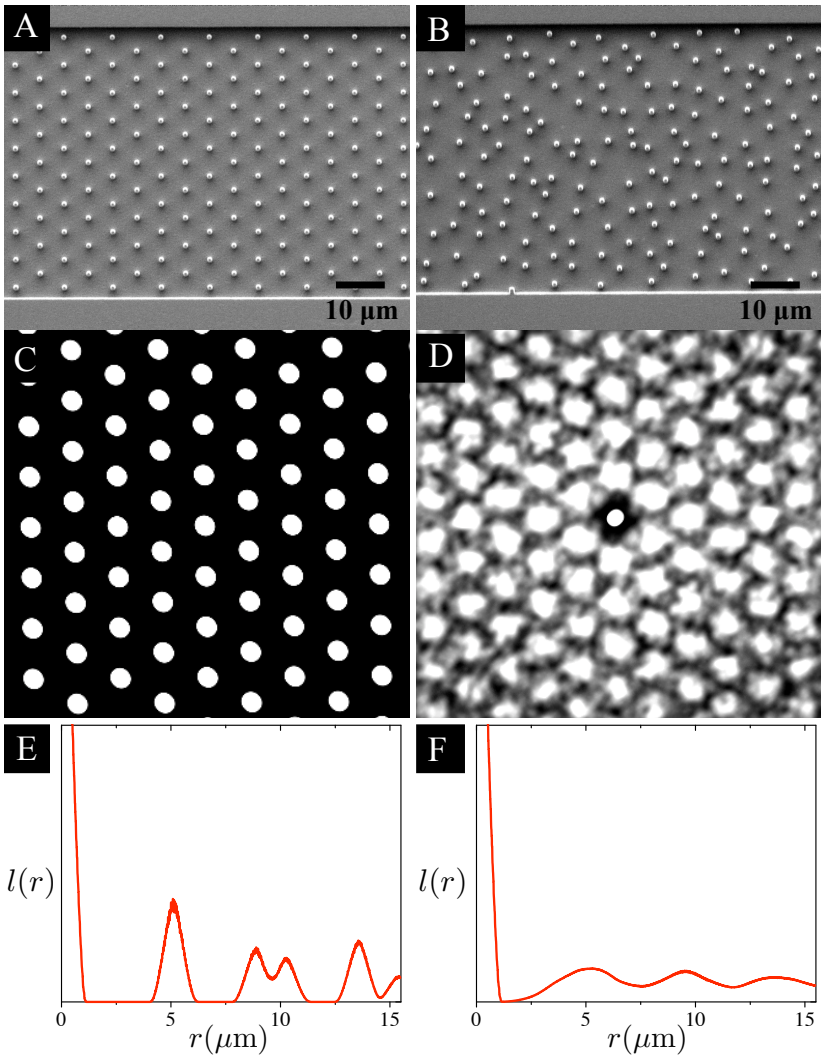

Figure 7.3: Scanning Electron Micrographs of the oxidized array geometry for the ordered hexagonal array (A) and the disordered array (B). 2D autocorrelation function of the binary SEM image of the ordered array (C) and of the disordered array (D). Radial intensity function of the ordered array (E) and disordered array (F). The autocorrelation function and radial intensity functions are discussed in section 7.4.1.

to a glass backplate and plastic reservoirs (Upchurch Scientific) with NOA 81 optical adhesive (Norland Products).

We dyed λ DNA (48,502 bp, New England Biolabs) with the fluorescent dye YOYO-1 (Molecular Probes) at a ratio of one dye molecule to eight bp of DNA. At this dye ratio, YOYO-1 bisintercalation into the DNA backbone saturates and external binding to the DNA molecule begins [123]. We have found that a relatively high dye ratio is useful for high spatial and temporal resolution of single molecules based on our previous work [35,60]. While such a high dye ratio was not necessary for data acquisition in the 5-reservoir device, we used a constant dye ratio for both the single molecule and the ensemble level experiments to facilitate comparison between them.

Prior to DNA loading, we filled one reservoir of the channel with a solution of 1 wt% polyvinylpyrrolidone (PVP) in DI water and loaded the channel using a syringe pump for one hour. Neutral, adsorbed polymers suppress electroosmotic flow (EOF) during electrophoresis by forming a dynamic surface coating [102]. While several polymers have been shown to reduce EOF in capillaries [124], we chose PVP based on its success in microfluidic devices [31, 35, 37, 48, 59, 60, 62, 63, 89]. The device can be conditioned with the polymer overnight to develop a uniform surface coating [35, 125, 126]; however, several groups have had success conditioning the device for less than one minute [124], or simply including polymer in the running buffer [31, 37, 62, 63, 89]. Our one hour conditioning time is sufficient for EOF suppression and has been reported elsewhere [59, 60, 127].

We then equilibriated the channel with a running buffer of 2.2x TBE, supplemented with 0.07 wt% PVP, 0.07 wt% ascorbic acid, which was pumped into the channel with a syringe pump for one hour. The high salt concentration of this buffer reduces the size of the electric double layer and is commonly used in microfluidic electrophoresis experiments [31, 35, 37, 58, 60, 63, 89]. Before DNA loading, we heated 200 μL of a solution of approximately 0.1 μg/mL λ

DNA in running buffer at 70°C for 15 minutes to melt any λ DNA concatemers to single, linear λ DNA molecules. A potential difference of 10 V was applied across the 1 cm long channel using platinum electrodes and a Trek power supply (Model 677B), corresponding to a nominal electric field of 10 V/cm. Images were captured on an EM-CCD camera (Photometrics Cascade II) at 25 frames per second using a 100x, 1.4 NA, oil immersion objective on an inverted epifluorescence microscope (Leica DMI 4000B).

We analyzed the single molecule data in the context of the two-state continuous-time random walk (CTRW) model described in Chapters 4 and 5. To measure the hold-up time, we fixed the observation window at the end of each post array and recorded tif stacks with 0.04 second exposure time. We were able to observe a length of the array equivalent to 18 rows of posts. We analyzed the video microscopy data using the automated tracking program described in Chapter 5. To find the probability distribution of the distance between collisions (x) we needed to observe a collision pair from a large fraction of the molecules. While this measurement was possible in a 3 μm spacing array using a stationary stage [60], the decreased post density studied here led to an increase in x. To measure collision pairs we needed to increase the length of the viewing window. We automated the stage using Micro-Manager to follow the DNA molecules as they travel through the post array. The viewing window began at the array entrance and moved the equivalent of 9 rows of posts 4 times to follow individual DNA molecules through the whole post array. The timing of the stage jumps was determined by the average DNA velocity in the array. Using this method we were able to track individual molecules over an expanded viewing window of 50 rows of posts. Photo-bleaching of the DNA molecules limits the measurement of this distance at an applied field of 10 V/cm. We located DNA-post collisions in the moving stage videos manually using the 4-quadrant definition of a collision [31]. We measured the total intensity of each molecule to ensure that it is λ-DNA and not a small fragment of DNA. The cumulative probability density does not go to unity

because some molecules do not make a second collision in the array.

7.2.2 Velocity and Dispersion Measurements in a 5 Reservoir Device

The DNA electrophoretic mobility (μ) remains relatively constant in a single day of experiments but normally varies over different days of experiments due to environmental factors [59]. In order to measure mobility simultaneously in different geometries during a single experiment, and thus avoid the error due to day-to-day variations, we designed a 5-reservoir device with 15 mm ordered and 15 mm disordered arrays side-by-side in oxidized silicon (Fig. 7.2). A single experiment in this device greatly reduces variations in mobility because (i) all surfaces in the device receive the same pretreatment; (ii) buffer conditions are identical; (iii) background electro-osmotic flow is constant; and (iv) other uncontrolled variables (temperature, etc.) are the same for the ordered and disordered arrays.

The 5-reservoir device was fabricated as described previously [63] with two exceptions; the photolithography step and device assembly. Instead of projection lithography, we used standard photolithography (Karl Suss MA-6) with S1805 photoresist (Shipley). The device was anodically bonded to 500 μm thick BOROFLOAT glass as this thicker glass is easier to handle and DNA was not imaged with high numerical aperture objectives in this device. The assembled device was sealed into a polycarbonate chip holder which increased the reservoir volume to 200 μL.

We injected a plug of λ DNA into the ordered and disordered arrays simultaneously and scanned each channel using an automated stage (Prior Scientific) mounted on an inverted epifluorescence microscope (Leica). The 5-reservoir device has two DNA loading reservoirs that are connected with common buffer supply and waste reservoirs by two shifted T injection areas. Voltage

was set at each of the five reservoirs by a platinum electrode connected to a high voltage power supply. The electric field was calculated by Kirchoff's Law assuming a constant resistance in all channels of the device. This assumption is valid because the post density is very low; 93% of the volume of the post array contains the buffer solution. A photomultiplier tube imaged the fluorescent DNA to record intensity versus time. We used MATLAB to calculate the DNA intensity as a function of distance from the injection. An example of the intensity versus position data is shown in Fig. 7.4. The channel scanning method gave us a measurement of DNA intensity versus position once every 15 seconds. We calculated the velocity of DNA from the best-fit line of the peak location versus time. For each time point, we also measured the full-width at half-max (FWHM) of the peak, which is related to the standard deviation of a Gaussian peak by FWHM $= \sigma\sqrt{8\ln(2)}$. We calculated the dispersion coefficient ($\bar{D}$) from the best-fit line to the variance versus time according to $\sigma^2 = 2\bar{D}t$. We found that $\bar{D}$ calculated from FWHM was more accurate than $\bar{D}$ calculated from a direct measurement of the variance due to noise in the intensity measurement and the error in the tails of the fit. All linear regression fitting resulted in high coefficients of determination; for the velocity measurement the minimum was R^2=0.998 and for the dispersion coefficient measurement the minimum was R^2=0.938.

The non-Gaussian shape of the peak in the disordered array (Fig. 7.4) is due to a defect in the channel immediately after the injection area. The injected plug of DNA must deform around the defect, resulting in a tail in the electropherogram. There is also a small peak of intensity at a distance slightly after the λ DNA peaks due to the presence of small fragments of DNA. These fragments could have been introduced from the original sample, or broken off from λ DNA by high shear flows during pipetting [105] or by photocleavage [103, 104]. The DNA fragments and imperfect injection result in deviations from Gaussian shaped electropherograms. Since our method for calculating the dispersion coefficient is based on the growth of the FWHM,

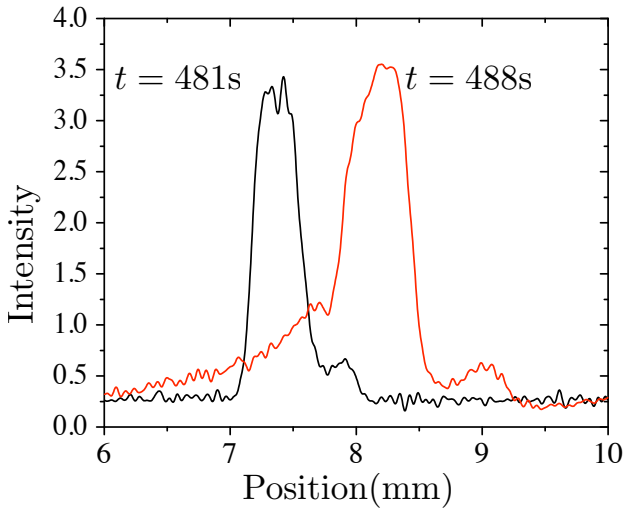

Figure 7.4: Overlaid electropherograms of λ DNA in the ordered array (black, $E = 6.9$ V/cm, $t = 481$ s) and in the disordered array (red, $E = 6.8$ V/cm, $t = 488$ s).

these imperfections are equivalent to background noise and do not lead to inaccuracies in the dispersion coefficient calculation. DNA velocity is calculated from the change in peak position with respect to time and is also unaffected by the non-Gaussian shape of the peaks.

7.3 Theory

According to the two-state continuous-time random walk (CTRW) model, DNA undergoing electrophoresis in a post array is considered to be in one of two states: (i) colliding with a post for hold-up time t_H with no center of mass displacement ($x = 0$), or (ii) translation for time t_T over a random distance x. DNA transport is fully described by the first and second moments of the random variables t_H, t_T, and x. The dispersion coefficient of a single

DNA size can be written as

$$2\bar{D}\left(\langle t_H\rangle + \langle t_T\rangle\right) = \sigma_x^2 + \bar{U}^2(\sigma_{t_H}^2 + \sigma_{t_T}^2) - 2\bar{U}\rho_{xt_T}, \tag{7.3}$$

where $\langle z\rangle$ represents the average of variable z and σ_z^2 is the variance in z. We must account for the space-time correlation, ρ_{xt_T}, defined as

$$\rho_{xt_T} = \langle xt_T\rangle - \langle x\rangle\langle t_T\rangle, \tag{7.4}$$

and estimated from the moving stage data. Values of the above variables were calculated from the distributions of the CTRW variables measured in single molecule experiments. We measured the hold-up time, t_H, from stationary stage experiments. The distribution of the distance between collisions, x, and the time between collisions, t_T, were measured from moving stage experiments. The velocity in the model is given by the distance traveled during one collision/translation cycle,

$$\bar{U} = \frac{\langle x\rangle}{\langle t_H\rangle + \langle t_T\rangle}. \tag{7.5}$$

7.4 Results and Discussion

7.4.1 Fabrication and Characterization

We directly measured the disorder of the array from a SEM image of a portion of the post array such as the ones in Fig. 7.3A and Fig. 7.3B. Using the Wiener-Khinchin theorem, we calculated the two dimensional autocorrelation function from the binary image of the array. The average intensity at a distance r from the origin of the autocorrelation function, $l(r)$, was given by the average intensity of pixels contained in an annulus of width 0.01 μm. Fig. 7.3C and Fig. 7.3D show the autocorrelation function of the ordered

array and Fig. 7.3E and Fig. 7.3F show the radial intensity function. The large, blurry spots in the autocorrelation function in Fig. 7.3D indicate the variation in post spacing in the disordered array. The dispersion of the array was based on the width of the second peak in a plot of $l(r)$ versus r (Fig. 7.3E, 7.3F) following the work of Minc *et al.* [66].

Using this method we measured $s = 0.045$ and 0.352 for the ordered and disordered arrays respectively. For comparison, s ranges from 0.16 to 0.47 in magnetic bead arrays [66]. The measured values differ from the theoretical array dispersion due to limitations in the mask making process. Explicitly, the post positions on the mask are limited to a 2D lattice and cannot be placed with infinite precision. This limited spatial resolution resulted in additional order in the disordered arrays and also prevented the fabrication of a perfectly ordered array.

7.4.2 Mobility

The electrophoretic mobility measured in the 5-reservoir device is plotted in Fig. 7.5 as a function of the applied electric field. We also computed the mean of the mobility measurements for both arrays and all E and plotted dashed lines one standard deviation above and below the mean. We only observed a 3% deviation from the mean electrophoretic mobility over all electric fields, array geometries, and different experiments. This variance in the measured mobility is comparable to that measured for a single DNA size at a single electric field in microfluidic devices [58,59,66]. While the standard deviation of mobility for small DNA molecules in capillary electrophoresis is around 1.7% [128], the standard deviation of mobility for large DNA in TBE buffer can be as high as 4% [127]. In light of the standard deviations observed in previous experiments and the data in Fig. 7.5, there is no significant difference in mobility between the hexagonal ordered array and the disordered array. Also, the mobility does not depend on the applied electric field.

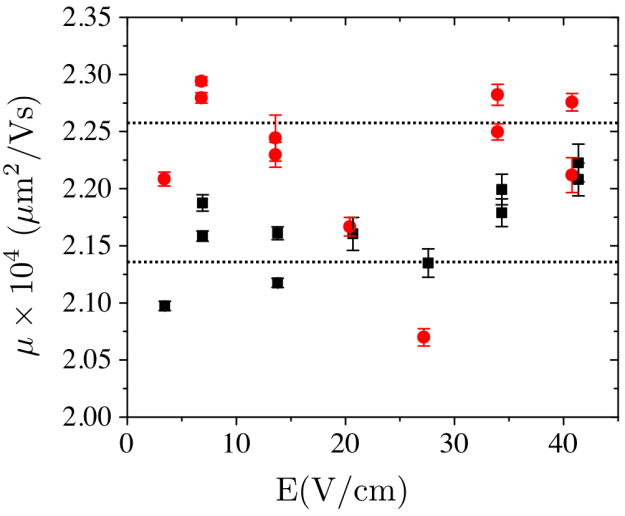

Figure 7.5: Electrophoretic mobility of λ DNA in the ordered array (black squares) and the disordered array (red circles) as a function of applied electric field. Error bars show the standard error for the fitting within a given experiment. Dashed lines show plus or minus one standard deviation from the mean of the data in this figure.

In the single molecule experiments, we determined the DNA mobility, μ, from the average passage time of DNA molecules across the fixed viewing window and we calculated the free solution mobility, μ_0, from the DNA velocity between collisions. From the single molecule experiments at 10 V/cm, we found a dimensionless mobility, μ/μ_0, of 0.874 in the ordered array and 0.870 in the disordered array. These dimensionless mobilities are less than unity due to frequent long-lived DNA-post collisions.

As shown in Table 7.1, the values of the velocity measured from the single molecule experiments in the 2-reservoir device do not match the velocity measured in the 5-reservoir device. Day-to-day variations in the buffer, channel conditions, and environmental factors can lead to differences in the electroosmotic flow (EOF), and thus in the measured DNA mobility [59]. If we assume that the variation in velocity between experiments comes from a dif-

Table 7.1: Summary of the velocity, $\bar{U}$, and dispersion coefficient, $\bar{D}$ in each experiment.

	Array Type	E	$\bar{U}$ (μm/s)	$\bar{D}$ (μm^2/s)
5-reservoir	ordered	6.9	15.0	28.9
2-reservoir	ordered	10	18.6	16.9
5-reservoir	ordered	13.8	29.5	56.2
5-reservoir	disordered	6.8	15.5	47.6
2-reservoir	disordered	10	19.0	18.5
5-reservoir	disordered	13.6	30.4	226

ference in the electro-osmotic flow in the different devices, it is useful to write the electrophoretic mobility as a contribution from interactions with the post array, μ^o, and a contribution due to the EOF, μ_{EOF}:

$$\mu = \mu^o + \mu_{\text{EOF}}. \tag{7.6}$$

The mobility due to interactions with the post arrays depends on the array type only. The EOF term is the same within an experiment but varies between the two sets of experiments. Thus, the difference in mobility, $\Delta\mu$, between the 2-reservoir device, μ_2, and 5-reservoir device, μ_5, for a single array type (ordered or disordered) could be explained by the change in the electro-osmotic flow, $\Delta\mu = \Delta\mu_{\text{EOF}}$. We found that $\Delta\mu_{\text{EOF}} = 0.30$ μm cm/Vs in the ordered array and $\Delta\mu_{\text{EOF}} = 0.36$ μm cm/Vs in the disordered array. While these two values are not identical, they are within the experimental error.

To further investigate the difference between DNA electrophoresis in ordered and disordered arrays, we looked at the parameters of the continuous-time random walk model [83]. We measured the hold-up time under an applied electric field of 10 V/cm for 602 collisions in the disordered array and for 326 collisions in the ordered array and plotted the cumulative distribution function in Fig. 7.6. The two distributions are the same to within a 93.5%

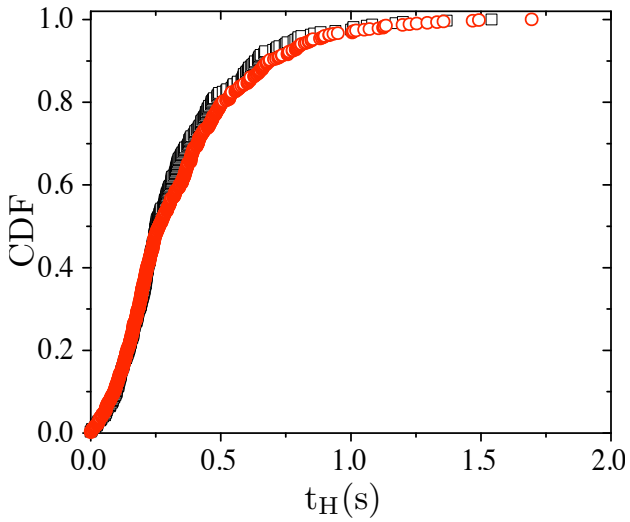

Figure 7.6: Cumulative distribution function (CDF) of the hold-up times for the ordered array (black squares) and the disordered array (red circles). The hold-up times are measured from single molecule videomicroscopy at a fixed position at 10 V/cm.

confidence level. The data follow the gamma distribution as was the case for DNA collisions with an isolated post [35] and in the nanofence geometry described in Chapter 6. In the two-state CTRW model, computing the DNA velocity requires the mean hold-up time, while information on the full hold-up time distribution is important for determining the dispersion coefficient of a group of DNA molecules. The mean hold-up time is 0.32 s in the ordered array and 0.35 s in the disordered array. The mean hold-up times are similar because post size is the same in both arrays, and DNA molecules were rarely hung up on more than one post at a time at 10 V/cm. While the arrangement of the posts does affect the electrical forces acting on the molecule, the differences in post arrangement do not lead to an appreciable difference in the hold-up time once a DNA molecule is engaged with a post.

From the stationary stage data we were able to estimate the collision probability for the DNA in each of the arrays at 10 V/cm from the number of

collisions observed as molecules passed through the viewing window divided by the number of rows in the viewing window. We found $\rho_c = 0.052$ in the ordered array and $\rho_c = 0.081$ in the disordered array. The collision probability in the disordered array matches collision probabilities measured in magnetic bead arrays [66]. Both collision probabilities are in the range of ρ_c measured in uniform electric field simulations [75].

Using these collision probabilities as the probability for colliding in each row of posts, the cumulative distribution function (CDF) of the distance between collisions, x, would be

$$\mathrm{CDF}(\rho_c, x) = 1 - \exp\left(\rho_c x\right). \tag{7.7}$$

We plotted this model for each array as the solid lines in Fig. 7.7. The decreased collision probability in the ordered array is due to fact that alternating rows of posts are offset by 2.5 μm. This large lateral offset reduces the collision probability in alternating rows because the molecule is unable to diffuse lateral to the applied electric field to collide with the first few offset rows. This qualitative explanation is supported by single molecule data for the the distance between collisions in the ordered array, which are shown in the inset of Fig. 7.7. Because some posts are unavailable for collision in the ordered array we see a lower collision probability than in the disordered array for short distances. As we will explain later, the collision probabilities for the ordered array and disordered array converge for long distances.

We must observe two collisions for a single molecule to be able to measure the distance between collisions. In the stationary stage experiment the majority of the molecules pass through the viewing window without making two collisions. In those experiments, the distance between collisions can be no more than 70 μm and, unsurprisingly, we find that the measured distribution is biased towards small distances between collisions. To increase the viewing window to 216 μm, we captured video data while moving the stage to follow

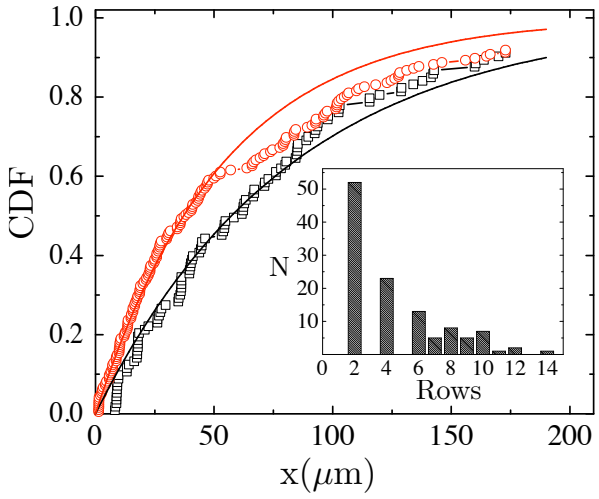

Figure 7.7: The cumulative distribution function (CDF) of the distance between collisions for the ordered array (black squares) and the disordered array (red circles). The solid lines show the CDFs predicted by Eq. 7.7. Molecules included in the data set were tracked at least 180 μm after their initial collision. For the ordered array, 91.2% (103/113) of the molecules collide within 180 μm while for the disordered array, 91.8% (179/195) of the molecules collide within 180 μm. The inset shows the number of collisions, N, for a given number of rows between collisions observed at each distance in the stationary stage experiment in the ordered array.

individual DNA molecules using the protocol described above. To remove any bias in the measured distribution, we defined a cut-off distance of 180 μm. Any molecule included in the distribution must be observed for at least 180 μm after it makes its first collision. The cumulative distribution function for this unbiased distance between collisions is shown for each array in Fig. 7.7. As we can see, λ DNA makes frequent collisions in both of the arrays. Over short distances, the CDF extrapolated from the stationary stage experiments matches the CDF measured in the moving stage experiments.

Due to the large offset between consecutive rows in the ordered post array, DNA molecules cannot make a collision with every row. However, if the

molecule travels long enough in the ordered array without colliding, it will diffuse such that its location after a previous collision is uncorrelated to its current position. For this to occur, the molecule must diffuse over a distance equal to the distance from the edge of one post (its initial location after the collision) to the center of the offset row of posts. In a hexagonal array of 1 μm diameter posts with 5 μm spacing, this is a distance of $a = 2$ μm. The diffusion time is then $t_{\text{diff}} = a^2/2D_0$, where the diffusion coefficient of λ DNA is $D_0 = 0.47$ $\mu\text{m}^2/\text{s}$ [90]. In this time, the molecule travels a distance of 84.7 μm at the free solution mobility at $E = 10$ V/cm. The data in Fig. 7.7 show that the two CDFs converge after this distance. While the collision probabilities over short distances depend strongly on the order of the array, they become indistinguishable at long distances.

7.4.3 Plate Height

While the DNA velocity and electrophoretic mobility depend only on the first moment of the hold-up time and distance between collisions, the dispersion coefficient, and thus the plate height, depends on the second moment of these random variables as well. The second moment captures molecule to molecule variability, which gives rise to macroscopic band broadening. As discussed above, the hold-up time distributions (Fig. 7.6) and distance between collisions distributions (Fig. 7.7) measured from single molecule experiments at $E = 10$ V/cm show only a slight dependence on array order. From these results, and the time between collisions measured in the moving stage experiments, we calculated the dispersion coefficient in Table 7.1 using the CTRW model. We note that the dispersion coefficients for the 2-reservoir device do not account for any sources of dispersion in the channel not due to DNA-post collisions and thus represent a theoretical minimum. In the 5-reservoir experiments, we calculated the dispersion coefficient in each array from the growth of λ DNA peak width. Measurement of the dispersion coefficient

from macroscopic variables includes all sources of band broadening that are present during transport in the device. As in the single molecule case, the dispersion coefficients are higher in the disordered array in the 5-reservior experiments. Since the 5-reservoir experiments involve many possible sources of band broadening, it is unsurprising that they exhibit a higher total dispersion coefficient.

Experiments conducted in the 5-reservoir device allowed us to measure the dispersion coefficient at several different applied electric fields. We found that the dispersion coefficient is always higher in the disordered array, and increases with increasing electric field. This qualitative behavior agrees with experiments in magnetic bead arrays [65], experiments in ordered arrays [58], and in simulations of λ DNA in ordered arrays [41,83]. From the macroscopic measurements of the DNA velocity, $\bar{U}$, and dispersion coefficient, $\bar{D}$, we calculated the plate height, $H = 2\bar{D}/\bar{U}$, and plotted it in Fig. 7.8. The plot of plate height versus applied electric field in Fig. 7.8 shows that plate height in the ordered array is constant over the range of electric fields studied; however, plate height in the disordered array is not constant.

Simple scaling laws for the CTRW parameters suggest that H should be independent of E. We will assume that $t_H \sim E^{-1}$, which has been verified experimentally [29, 37]. We also propose that $t_T \sim E^{-1}$ which is equivalent to assuming that the free solution velocity scales with E. As shown in Fig. 7.5, $\mu \sim E^0$ and thus $\bar{U} \sim E$. We can write the DNA velocity as

$$\bar{U} = \frac{\langle x \rangle}{\langle t_H \rangle + \langle t_T \rangle}. \tag{7.8}$$

Since both times scale with E^{-1}, $\langle x \rangle$ must be independent of the applied electric field. This is equivalent to stating that the collision probability is independent of E, a common assumption in CTRW models [44,87] supported by experimental evidence [66,75]. Using $t_H \sim E^{-1}$ and $\rho_c \sim E^0$ we find that $\bar{D} \sim E$ from Taylor-Aris dispersion theory [80]. Thus, we expect that the

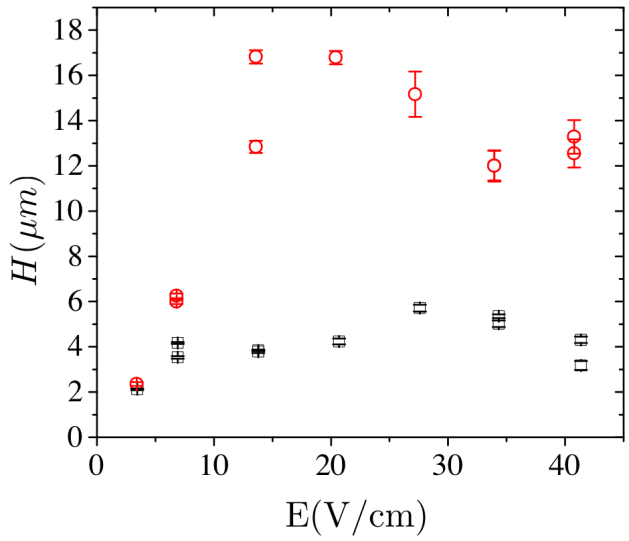

Figure 7.8: Plate height as a function of electric field for the ordered array (black squares) and the disordered array (red circles). Error bars show the standard error of the plate height in a given experiment. The dispersion coefficient is calculated from the band broadening measured in the channel scanning experiments.

plate height is independent of E. Indeed, this is true in the ordered array. However, the plate height in the disordered array is not constant across the range of E.

As we saw in Chapter 5, the two-state CTRW model lends insight into the sources of band broadening. We can express the plate height in general as

$$H = \frac{\sigma^2_{x-\bar{U}t_T}}{\langle x \rangle} + \frac{\bar{U}^2 \sigma^2_{t_H}}{\langle x \rangle} \tag{7.9}$$

where the first term is the contribution to H due to fluctuations in the transport between collisions and the second term is due to fluctuations in the hold-up time of a collision. We can already exclude the fluctuations in the distance between collisions as the source of the higher plate height in the disordered array since the CDF for the distance between collisions in Fig.

7.7 is similar for the ordered and disordered array for the large values of x that would dominate the variance. However, we also need to consider fluctuations in the time required to traverse the distance x. Convective transport between collisions is driven by the electric field. The posts are insulating, so the electric field lines bend around the posts leading to the curved field lines shown in Fig. 7.1. The field lines are more irregular in the disordered array, whereupon we might anticipate that the fluctuations in the time between collisions for a give distance x will be greater in the disordered array. However, the calculated electric field lines shown in Fig. 7.1 lead us to suspect that the difference in the local electrophoretic velocities are a small contribution to the plate height in this relatively sparse array.

If the first term in Eq. 7.9 is similar for the ordered and disordered array, the major contribution to H in the disordered array must be increased fluctuations in the hold-up time. We propose that this increase with electric field in the disordered array is caused by the non-uniform placement of the posts. Based on the Brownian dynamics simulations in Chapter 5, fluctuations in the hold-up time term are related to the extension of the molecule during collision. Specifically, once the molecule is extended enough to interact with two rows of posts during a collision, the plate height increases dramatically. Figure 7.1 shows a schematic of DNA colliding with the posts of each array and includes an example of a multiple post collision. Because DNA does not collide with consecutive rows in the ordered array (inset, Fig. 7.7), the minimum extension for a multiple post collision in the ordered array is equal to twice the row spacing, 8.7 μm. Note that the latter value is a very conservative estimate, since the unraveling chain needs to have sufficient relaxed DNA at its head to initiate a second collision. In the disordered array, the extension required for multiple post collisions varies depending on the location of the posts. Thus, multiple post collisions can occur even at relatively low extension in regions of the post array where the density of posts is high. Multiple post collisions have a much larger mean hold-up time than single

post collisions; therefore, a t_H distribution in an array where both types of collisions can occur has a much higher variance than a t_H distribution where only single post collisions are possible. As E increases, the extension of the molecule during collision increases. At $E > 10$ V/cm, the DNA extension is great enough to allow frequent multiple post collisions in the disordered array, which we believe results in the increase in H. Owing to the rapid motion of the chain at higher electric fields, it is difficult to confirm our hypothesis with single molecule measurements. The requisite extension in the ordered array for multiple post collisions occurs at a much higher E that is not reached in our single molecule experiments. As a result, the ordered array follows the models for collision with an isolated post [44, 80], where H is independent of E.

7.5 Conclusions

In this chapter, we measured the electrophoretic mobility and dispersion coefficient of a single size of DNA molecules in an ordered hexagonal array of posts and a disordered array of posts from two different types of experiments. Video microscopy experiments revealed micro-transport properties such as the hold-up time of a collision and the distance traveled between collisions. Although macroscopic measurements of a group of DNA in the array do not allow as much insight into the details of the transport process, they do allow us to measure mobility and dispersion over a large range of applied electric fields. Both types of experiments compare DNA dynamics in an ordered and disordered geometry in a single integrated device that isolates the effect of array order on transport.

To improve a separation, we must increase the separation resolution, which is proportional to the difference in mobility and inversely proportional to the square root of the plate height. Based on the data presented here, the array

type does not alter the DNA mobility. However, the plate height does depend on the array type. The increased plate height in the disordered array leads to greater band broadening in the device and to poorer separation resolution. We found that a lower applied electric field results in less band broadening and therefore a higher separation resolution. This result is in agreement with previous experiments of an electrophoretic separation of 48.5 kbp DNA and 2.7 kbp DNA in a sparse ordered array [59] and Brownian dynamics simulation of the separation of 169 kbp DNA and 48.5 kbp DNA [41].

The work presented here shows that DNA separation by rope-over-pulley collisions in a 2D device is optimized in an ordered geometry. Improvement in the separation due to reduced band broadening in an ordered, 2D geometry also occurs in liquid chromatography [129, 130]. DNA separation by Ogston sieving is possible in 3D geometries formed by self-assembly of colloid solutions [131]. While there has not been a study of the role of order in dc field separation in a colloidal crystal, a study of long DNA separation under a pulsed electric field in a 3D colloidal array found that an ordered matrix improved the separation resolution over a disordered matrix [132]. We anticipate that dc electric field separations in 3D colloidal arrays will also benefit from increased array order, similar to the results for protein chromatography in colloidal crystals [133].

Chapter 8

Concluding Thoughts

We used single molecule observations and Brownian dynamics simulations to increase our understanding of DNA size separation in post arrays. In Chapter 3, we proved that long DNA collide with posts frequently in ordered post arrays. This discovery validated our continued research in ordered post arrays since many DNA-post collisions are necessary for size separation. Prior models and simulations in ordered post arrays did not predict frequent collisions because they neglected the interaction between the electric field and the insulating post array. We showed that simulations utilizing a more complete calculation of the electric field *do* predict frequent collisions, in agreement with our experimental observations.

Many models of DNA transport in micropost arrays are based on continuous-time random walk (CTRW) statistics. In a Scher-Lax CTRW the probability of moving distance x in time t can be decomposed into the product of the probability of moving distance x and the conditional probability of doing so in time t. Many CTRW models predict the latter probabilities based on toy models of DNA transport in micropost arrays. In Chapter 4, we measured both the probability of moving distance x between collisions and the prob-

ability of a collision lasting a time t_H. We found that these probabilities are more difficult to predict than previously anticipated. Additionally, these probabilities must be precisely known to accurately predict macro-transport properties (mobility and band broadening) of groups of DNA. To apply the CTRW model to DNA transport, each DNA-post collision event must be independent. We showed that this assumption is valid in Chapter 4.

We measured x and t_H from experiments and from simulations and found that our simulation results match the experimental observations. We then measured x and t_H by simulation for a range of DNA sizes and applied electric fields in one particular post array. In Chapter 5, we used a new two-state CTRW model to calculate the electrophoretic mobility and band broadening from x and t_H. As a function of applied field, the DNA mobility depended on the distance between collisions. When we looked at DNA mobility as a function of DNA size, we found that the mobility depended on collision duration. According to the two-state model, DNA band broadening increases when the width of either the x or t_H distribution increases. In Chapter 5, we found that long DNA under high electric field stretched enough to interact with multiple posts, leading to fluctuations in the measured collision duration. These fluctuations increased the width of the t_H distribution and led to broad DNA peaks.

The knowledge gained from the CTRW analysis of the simulation data in Chapter 5 led us to design the nanofence geometry. A device based on this geometry is described in Chapter 6. The separation performance in the nanofence device was superior to that found in hexagonal arrays. While we hypothesized that the nanofence geometry would reduce band broadening, a study of the single molecule dynamics in the nanofence revealed the improved separation resolution was due to more efficient collisions.

All of the work in Chapters 3 to 6 dealt with DNA transport in ordered post arrays. In Chapter 7, we explored the role of disorder in the post

array on DNA dynamics. To do this, we observed single molecules in an ordered hexagonal array and in a disordered array with the same post density. Additionally, we experimentally measured the electrophoretic mobility and band broadening of an ensemble of DNA under a range of applied electric fields. We found that DNA mobility was unaffected by the order of the array. However, at moderate to high electric fields, band broadening was much higher in the disordered array. The geometry of the disordered array allows colliding DNA to interact with multiple posts at lower DNA stretching. Thus, the band broadening in the disordered array may be due to the multiple post collisions that we saw in Chapter 5.

We have learned some general rules for maximizing separation performance in post array devices. Ordered arrays are superior to disordered arrays because (i) ordered arrays are easier to fabricate using top-down fabrication; (ii) ordered arrays have decreased band broadening at moderate to high electric fields. Band broadening increases sharply when the DNA molecule extends enough to interact with multiple posts. This occurs for long DNA or under large forces (high applied electric field). The array should be sparse enough that multiple post interactions do not occur. However, lower post density decreases the collision frequency per unit length. Since a large number of collisions are needed to produce a size separation, low post density arrays require long separation lengths. The separation geometry should be tuned to maximize the post density while preventing multiple post interactions.

Experimentally measuring DNA separation performance for various DNA sizes at different applied electric fields is time consuming. Furthermore, changing the separation geometry is an expensive process that requires weeks to months of fabrication to build a new device. Because our Brownian dynamics simulation method matches the experimentally observed single molecule dynamics, we can use the simulation results and the two-state CTRW model to accurately predict separation performance. Thus, we can use simulations to guide device design.

Bibliography

[1] F. Collins, V. McKusick, Implications of the Human Genome Project for Medical Science, *Journal of the American Medical Association* **285** (2001) 540–544.

[2] P. Keim, T. Pearson, R. Okinaka, Microbial forensics: DNA fingerprinting of Bacillus anthracis (Anthrax), *Analytical Chemistry* **80** (2008) 4791–4799.

[3] J. L. Viovy, Electrophoresis of DNA and other polyelectrolytes: Physical mechanisms, *Reviews of Modern Physics* **72** (2000) 813–872.

[4] P. C. Hiemenz, T. P. Lodge, *Polymer Chemistry*, CRC Press, 2007.

[5] G. S. Manning, Limiting laws and counterion condensation in polyelectrolyte solutions I. Colligative Properties, *Journal of Chemical Physics* **51** (1969) 924–933.

[6] P. G. de Gennes, Reptation of a polymer chain in the presence of fixed obstacles, *Journal of Chemical Physics* **55** (1971) 572–579.

[7] C. Heller, T. A. J. Duke, J. L. Viovy, Electrophoretic Mobility of DNA in Gels. II. Systematic Experimental Study in Agarose Gels, *Biopolymers* **34** (1994) 249–259.

[8] T. A. J. Duke, A. N. Semenov, J. L. Viovy, Mobility of a reptating polymer, *Physical Review Letters* **69** (1992) 3260–3263.

[9] D. C. Schwartz, C. R. Cantor, Separation of yeast chromosome-sized DNAs by pulsed field gradient gel electrophoresis, *Cell* **37** (1984) 67–75.

[10] G. F. Carle, M. V. Olson, An Electrophoretic Karyotype for Yeast, *Proceedings of the National Academy of Sciences* **82** (1985) 3756–3760.

[11] C. L. Smith, C. R. Cantor, Purification, specific fragmentation, and separation of large DNA molecules, *Methods in Enzymology* **155** (1987) 449–67.

[12] S. Gurrieri, S. B. Smith, K. S. Wells, I. D. Johnson, C. Bustamante, Real-time imaging of the reorientation mechanisms of YOYO-labelled DNA molecules during 90 degrees and 120 degrees pulsed field gel electrophoresis, *Nucleic Acids Research* **24** (1996) 4759–4767.

[13] T. Kobayashi, M. Doi, Y. Makino, M. Ogawa, Mobility minima in field-inversion gel electrophoresis, *Macromolecules* **23** (1990) 4480–4481.

[14] J. J. Schwinefus, M. D. Morris, Periodicity of λ DNA Motions during Field Inversion Electrophoresis in Dilute Hydroxyethyl Cellulose Visualized by High-Speed Video Fluorescence Microscopy, *Macromolecules* **32** (1999) 3678–3684.

[15] J. Sudor, M. V. Novotny, Separation of Large DNA Fragments by Capillary Electrophoresis under Pulsed-Field Conditions, *Analytical Chemistry* **66** (1994) 2446–2450.

[16] M. Cabodi, S. W. P. Turner, H. G. Craighead, Entropic recoil separation of long DNA molecules, *Analytical Chemistry* **74** (2002) 5169–5174.

[17] S. W. P. Turner, M. Cabodi, H. G. Craighead, Confinement-induced entropic recoil of single DNA molecules in a nanofluidic structure, *Physical Review Letters* **88** (2002) 128103.

[18] M. Cabodi, Y. F. Chen, S. W. P. Turner, H. G. Craighead, R. H. Austin, Continuous separation of biomolecules by the laterally asym-

metric diffusion array with out-of-plane sample injection, *Electrophoresis* **23** (2002) 3496–3503.

[19] T. A. J. Duke, R. H. Austin, Microfabricated Sieve for the Continuous Sorting of Macromolecules, *Physical Review Letters* **80** (1998) 1552–1555.

[20] D. Ertaş, Lateral Separation of Macromolecules and Polyelectrolytes in Microlithographic Arrays, *Physical Review Letters* **80** (1998) 1548–1551.

[21] L. R. Huang, E. C. Cox, R. H. Austin, J. C. Sturm, Tilted Brownian Ratchet for DNA Analysis, *Analytical Chemistry* **75** (2003) 6963–6967.

[22] K. Inatomi, S. Izuo, S. S. Lee, H. Ohji, S. Shiono, Electrophoresis of DNA in micro-pillars fabricated in polydimethylsiloxane, *Microelectronic Engineering* **70** (2003) 13–18.

[23] J. Han, H. Craighead, Separation of long DNA molecules in a microfabricated entropic trap array, *Science* **288** (2000) 1026–1029.

[24] F. Tessier, J. Labrie, G. W. Slater, Electrophoretic separation of long polyelectrolytes in submolecular-size constrictions: A Monte Carlo study, *Macromolecules* **35** (2002) 4791–4800.

[25] M. Streek, F. Schmid, T. T. Duong, A. Ros, Mechanisms of DNA separation in entropic trap arrays: a Brownian dynamics simulation, *Journal of Biotechnology* **112** (2004) 79–89.

[26] A. S. Panwar, S. Kumar, Time scales in polymer electrophoresis through narrow constrictions: A Brownian dynamics study, *Macromolecules* **39** (2006) 1279–1289.

[27] S. H. Kim, A. S. Panwar, S. Kumar, K. H. Ahn, S. J. Lee, Electrophoresis of a bead-rod chain through a narrow slit: A Brownian dynamics study, *The Journal of Chemical Physics* **121** (2004) 9116–9122.

[28] K. Dorfman, DNA electrophoresis in microfabricated devices, *Reviews of Modern Physics* **82** (2010) 2903–2947.

[29] W. D. Volkmuth, T. Duke, M. C. Wu, R. H. Austin, A. Szabo, DNA electrodiffusion in a 2D array of posts, *Physical Review Letters* **72** (1994) 2117–2120.

[30] G. I. Nixon, G. W. Slater, DNA Electrophoretic Collisions with Single Obstacles, *Physical Review E* **50** (1994) 5033–5038.

[31] G. C. Randall, P. S. Doyle, Electrophoretic collision of a DNA molecule with an insulating post, *Physical Review Letters* **93** (2004) 058102.

[32] G. C. Randall, P. S. Doyle, DNA deformation in electric fields: DNA driven past a cylindrical obstruction, *Macromolecules* **38** (2005) 2410–2418.

[33] E. Sevick, D. Williams, Collision of a field-driven polymer with a post: Electrophoresis in microlithographic arrays, *Physical Review Letters* **76** (1996) 2595–2598.

[34] N. Araki, E. S. Aydil, K. D. Dorfman, Collision of a long DNA molecule with an isolated nanowire, *Electrophoresis* **31** (2010) 3675–3680.

[35] M. N. Joswiak, J. Ou, K. D. Dorfman, Statistical properties of the electrophoretic collision of a long DNA molecule with a small obstacle, *Electrophoresis* **33** (2012) 1013–1020.

[36] N. Laachi, J. Cho, K. Dorfman, DNA unhooking from a single post as a deterministic process: Insights from translocation modeling, *Physical Review E* **79** (2009) 31928.

[37] G. C. Randall, P. S. Doyle, Collision of a DNA polymer with a small obstacle, *Macromolecules* **39** (2006) 7734–7745.

[38] J. Kim, P. Doyle, Brownian Dynamics Simulations of a DNA Molecule Colliding with a Small Cylindrical Post, *Macromolecules* **40** (2007) 9151–9163.

[39] W. D. Volkmuth, T. A. J. Duke, R. H. Austin, Trapping of branched DNA in microfabricated structures, *Proceedings of the National Academy of Sciences* **92** (1995) 6887–6891.

[40] E. Sevick, D. Williams, Long-lived states in electrophoresis: Collision of a polymer chain with two or more obstacles, *Europhysics Letters* **56** (2001) 529–535.

[41] J. Cho, K. D. Dorfman, Brownian dynamics simulations of electrophoretic DNA separations in a sparse ordered post array, *Journal of Chromatography A* **1217** (2010) 5522–5528.

[42] Y. Masubuchi, H. Oana, T. Akiyama, M. Matsumoto, M. Doi, Dynamics of a DNA Molecule Hanging over an Obstacle in Gel Electrophoresis, *Journal of the Phyiscal Society of Japan* **64** (1995) 1412–1412.

[43] P. M. Saville, E. M. Sevick, Collision of a field-driven polymer with a finite-sized obstacle: A Brownian dynamics simulation, *Macromolecules* **32** (1999) 892–899.

[44] N. Minc, J. L. Viovy, K. D. Dorfman, Non-Markovian transport of DNA in microfluidic post arrays, *Physical Review Letters* **94** (2005) 198105.

[45] W. D. Volkmuth, R. H. Austin, DNA electrophoresis in microlithographic arrays, *Nature* **358** (1992) 600–602.

[46] Y. C. Chan, Y. Lee, Y. Zohar, High-throughput design and fabrication of an integrated microsystem with high aspect-ratio sub-micron pillar arrays for free-solution micro capillary electrophoresis, *Journal of Micromechanics and Microengineering* **16** (2006) 699.

[47] M. Baba, T. Sano, N. Iguchi, K. Iida, T. Sakamoto, H. Kawaura, DNA size separation using artifically nanostructured matrix, *Applied Physics Letters* **83** (2003) 1468–1470.

[48] N. Kaji, Y. Tezuka, Y. Takamura, M. Ueda, T. Nishimoto, H. Nakanishi, Y. Horiike, Y. Baba, Separation of long DNA molecules by quartz nanopillar chips under a direct current electric field, *Analytical Chemistry* **76** (2004) 15–22.

[49] R. Ogawa, N. Kaji, S. Hashioka, Y. Baba, Y. Horiike, Fabrication and characterization of quartz nanopillars for DNA separation by size, *Japanese Journal of Applied Physics* **46** (2007) 2771–2774.

[50] R. Ogawa, H. Ogawa, A. Oki, S. Hashioka, Y. Horiike, Fabrication of nano-pillar chips by a plasma etching technique for fast DNA separation, *Thin Solid Films* **515** (2007) 5167–5171.

[51] N. Kaji, A. Oki, R. Ogawa, Y. Takamura, T. Nishimoto, H. Nakanishi, Y. Horiike, M. Tokeshi, Y. Baba, Influences of electroosmotic flows in nanopillar chips on DNA separation: Experimental results and numerical simulations, *Israel Journal of Chemistry* **47** (2008) 161–169.

[52] J. Shi, A. P. Fang, L. Malaquin, A. Pépin, D. Decanini, J. L. Viovy, Y. Chen, Highly parallel mix-and-match fabrication of nanopillar arrays integrated in microfluidic channels for long DNA molecule separation, *Applied Physics Letters* **91** (2007) 153114.

[53] W. Hattori, H. Someya, M. Baba, H. Kawaura, Size-based continuous-flow directional control of DNA with a nano-pillar anisotropic array, *Journal of Chromatography A* **1051** (2004) 141–146.

[54] C. W. Kuo, K. H. Wei, C. H. Lin, J. Y. Shiu, P. Chen, Nanofluidic system for the studies of single DNA molecules, *Electrophoresis* **29** (2008) 2931–2938.

[55] S. W. Turner, A. M. Perez, A. Lopez, H. G. Craighead, Monolithic nanofluid sieving structures for DNA manipulation, *Journal of Vacuum Science and Technology B* **16** (1998) 3835–3840.

[56] O. B. Bakajin, T. A. J. Duke, C. F. Chou, S. S. Chan, R. H. Austin, E. C. Cox, Electrohydrodynamic stretching of DNA in confined environments, *Physical Review Letters* **80** (1998) 2737–2740.

[57] O. B. Bakajin, T. A. J. Duke, J. Tegenfeldt, C. F. Chou, S. S. Chan, R. H. Austin, E. C. Cox, Separation of 100-kilobase DNA molecules in 10 seconds, *Analytical Chemistry* **73** (2001) 6053–6056.

[58] J. Ou, J. Cho, D. Olson, K. Dorfman, DNA electrophoresis in a sparse ordered post array, *Physical Review E* **79** (2009) 61904.

[59] J. Ou, S. Carpenter, K. Dorfman, Onset of channeling during DNA electrophoresis in a sparse ordered post array, *Biomicrofluidics* **4** (2010) 013203.

[60] D. W. Olson, J. Ou, M. Tian, K. D. Dorfman, Continuous-time random walk models of DNA electrophoresis in a post array: Part I. Evaluation of existing models, *Electrophoresis* **32** (2011) 573–580.

[61] Y. C. Chan, Y. Zohar, Y. Lee, Effects of embedded sub-micron pillar arrays in microfluidic channels on large DNA electrophoresis, *Electrophoresis* **30** (2009) 3242–3249.

[62] J. Ou, M. N. Joswiak, S. J. Carpenter, K. D. Dorfman, Plasma thinned nanopost arrays for DNA electrophoresis, *Journal of Vacuum Science and Technology A* **29** (2011) 011025.

[63] S.-G. Park, D. W. Olson, K. D. Dorfman, DNA electrophoresis in a nanofence array, *Lab on a Chip* **12** (2012) 1463–1470.

[64] P. S. Doyle, J. Bibette, A. Bancaud, J. L. Viovy, Self-Assembled Magnetic Matrices for DNA Separation Chips, *Science* **295** (2002) 2237–2237.

[65] N. Minc, C. Futterer, K. D. Dorfman, A. Bancaud, C. Gosse, C. Goubault, J. L. Viovy, Quantitative microfluidic separation of DNA in self-assembled magnetic matrixes, *Analytical Chemistry* **76** (2004) 3770–3776.

[66] N. Minc, P. Bokov, K. B. Zeldovich, C. Futterer, J. L. Viovy, K. D. Dorfman, Motion of single long DNA molecules through arrays of magnetic columns, *Electrophoresis* **26** (2005) 362–375.

[67] R. Haghgooie, C. Li, P. S. Doyle, Experimental Study of Structure and Dynamics in a Monolayer of Paramagnetic Colloids Confined by Parallel Hard Walls, *Langmuir* **22** (2006) 3601–3605.

[68] R. Haghgooie, P. S. Doyle, Directed self-assembly of field-responsive fluids in confined geometries, *Soft Matter* **5** (2009) 1192–1197.

[69] A. E. Saliba, C. Gosse, N. Minc, C. Roblin, K. D. Dorfman, J.-L. Viovy, Ni pattern for guiding magnetic beads self-organization: Application to long DNA electrophoresis in dilute arrays, in: T. Kitamori, H. Fujita, S. Hasebe (Eds.), Proceedings of the 10th International Conference on Miniaturized Systems for Chemistry and Life Sciences, Tokyo, Japan, 2006, pp. 386–388.

[70] J. C. Giddings, *Unified Separation Science*, John Wiley & Sons, 1991.

[71] C. T. Culbertson, S. C. Jacobson, J. M. Ramsey, Dispersion Sources for Compact Geometries on Microchips, *Analytical Chemistry* **70** (1998) 3781–3789.

[72] J. I. Molho, A. E. Herr, B. P. Mosier, J. G. Santiago, T. W. Kenny, R. A. Brennen, G. B. Gordon, B. Mohammadi, Optimization of turn ge-

ometries for microchip electrophoresis, *Analytical Chemistry* **73** (2001) 1350–1360.

[73] B. M. Rush, K. D. Dorfman, H. Brenner, S. Kim, Dispersion by Pressure-Driven Flow in Serpentine Microfluidic Channels, *Industrial and Engineering Chemistry Research* **41** (2002) 4652–4662.

[74] E. Yariv, H. Brenner, S. Kim, Curvature-Induced Dispersion in Electro-Osmotic Serpentine Flows, *SIAM Journal on Applied Mathematics* **64** (2004) 1099–1124.

[75] A. Mohan, P. S. Doyle, Effect of disorder on DNA electrophoresis in a microfluidic array of obstacles, *Physical Review E* **76** (2007) 040903(R).

[76] P. D. Patel, E. S. G. Shaqfeh, A computational study of DNA separations in sparse disordered and periodic arrays of posts, *Journal of Chemical Physics* **118** (2003) 2941–2951.

[77] J. M. Deutsch, Theoretical studies of DNA during gel electrophoresis, *Science* **240** (1988) 922–924.

[78] J. M. Deutsch, T. L. Madden, Theoretical studies of DNA during gel electrophoresis, *Journal of Chemical Physics* **90** (1989) 2476–2485.

[79] S. Popelka, Z. Kabatek, J. L. Viovy, B. Gas, Peak dispersion due to geometration motion in gel electrophoresis of macromolecules, *Journal of Chromatography A* **838** (1999) 45–53.

[80] K. D. Dorfman, J. L. Viovy, Semiphenomenological model for the dispersion of DNA during electrophoresis in a microfluidic array of posts, *Physical Review E* **69** (2004) 11901.

[81] H. Scher, M. Lax, Stochastic transport in a disordered solid. I. Theory, *Physical Review B* **7** (1973) 4491–4502.

[82] K. D. Dorfman, DNA electrophoresis in microfluidic post arrays under moderate electric fields, *Physical Review E* **73** (2006) 061922.

[83] D. W. Olson, S. Dutta, N. Laachi, M. Tian, K. D. Dorfman, Continuous-time random walk models of DNA electrophoresis in a post array: Part II. Mobility and sources of band broadening, *Electrophoresis* **32** (2011) 581–587.

[84] T. A. J. Duke, R. H. Austin, E. C. Cox, S. S. Chan, Pulsed-field electrophoresis in microlithographic arrays, *Electrophoresis* **17** (1996) 1075–1079.

[85] M. R. Mohamadi, L. Mahmoudian, N. Kaji, M. Tokeshi, H. Chuman, Y. Baba, Nanotechnology for genomics and proteomics, *Nanotoday* **1** (2006) 38–45.

[86] G. W. Slater, S. Guillouzic, M. G. Gauthier, J.-F. Mercier, M. Kenward, L. C. McCormick, F. Tessier, Theory of DNA electrophoresis, *Electrophoresis* **23** (2002) 3791–3816.

[87] A. Mohan, P. Doyle, Stochastic modeling and simulation of DNA electrophoretic separation in a microfluidic obstacle array, *Macromolecules* **40** (2007) 8794–8806.

[88] D. C. Duffy, J. C. McDonald, O. J. A. Schueller, G. M. Whitesides, Rapid prototyping of microfluidic systems in Poly(dimethylsiloxane), *Analytical Chemistry* **70** (1998) 4974–4984.

[89] G. C. Randall, P. S. Doyle, Permeation-driven flow in poly(dimethylsiloxane) microfluidic devices, *Proceedings of the National Academy of Sciences* **102** (2005) 10813–10818.

[90] D. E. Smith, T. T. Perkins, S. Chu, Dynamical Scaling of DNA Diffusion Coefficients, *Macromolecules* **29** (1996) 1372–1373.

[91] C. T. Culbertson, S. C. Jacobson, J. M. Ramsey, Diffusion coefficient measurements in microfluidic devices, *Talanta* **56** (2002) 365–373.

[92] J. Cho, M. Kenward, K. D. Dorfman, A boundary element method/Brownian dynamics approach for simulating DNA electrophoresis in electrically insulating microfabricated devices, *Electrophoresis* **30** (2009) 1482–1489.

[93] J. F. Marko, E. D. Siggia, Stretching DNA, *Macromolecules* **28** (1995) 8759–8770.

[94] P. T. Underhill, P. S. Doyle, On the coarse-graining of polymers into bead-spring chains, *Journal of Non-Newtonian Fluid Mechanics* **122** (2004) 3–31.

[95] R. M. Jendrejack, J. J. De Pablo, M. D. Graham, Stochastic simulations of DNA in flow: Dynamics and the effects of hydrodynamic interactions, *The Journal of Chemical Physics* **116** (2002) 7752.

[96] D. M. Heyes, J. R. Melrose, Brownian dynamics simulations of model hard-sphere suspensions, *Journal of Non-Newtonian Fluid Mechanics* **46** (1993) 1–28.

[97] H. Igarashi, T. Honma, Strategies for the Accurate Computation of Potential Derivatives in Boundary Element Method: Application of Two-Dimensional Problems, *Journal of Computational Physics* **119** (1995) 244–251.

[98] J. M. Kim, P. S. Doyle, A Brownian dynamics-finite element method for simulating DNA electrophoresis in nonhomogeneous electric fields, *Journal of Chemical Physics* **125** (2006) 074906.

[99] M. J. Krawczyk, J. Dulak, K. Kułakowski, Mean free path and peak dispersion in the geometration motion in gel electrophoresis, *Electrophoresis* **23** (2002) 182–185.

[100] M. J. Krawczyk, J. Dulak, P. Pasciak, K. Kulakowski, Diffusion constant in gel electrophoresis at high fields, *Electrophoresis* **25** (2004) 785–789.

[101] K. D. Dorfman, Erratum: DNA electrophoresis in microfluidic post arrays under moderate electric fields [Phys. Rev. E **73**, 061922 (2006)], *Physical Review E* **77** (2008) 019901(E).

[102] O. A. Hickey, J. L. Harden, G. W. Slater, Molecular Dynamics Simulations of Optimal Dynamic Uncharged Polymer Coatings for Quenching Electro-osmotic Flow, *Physical Review Letters* **102** (2009) 108304.

[103] S. Gurrieri, K. Wells, I. Johnson, C. Bustamante, Direct visualization of individual DNA molecules by fluorescence microscopy: characterization of the factors affecting signal/background and optimization of imaging conditions using YOYO, *Analytical Biochemistry* **249** (1997) 44–53.

[104] B. Akerman, E. Tuite, Single- and double-strand photocleavage of DNA by YO, YOYO and TOTO, *Nucleic Acids Research* **24** (1996) 1080–1090.

[105] R. Kovacic, L. Comal, A. Bendich, Protection of megabase DNA from shearing, *Nucleic Acids Research* **23** (1995) 3999–4000.

[106] J. Bonis-O'Donnell, W. Reisner, D. Stein, Pressure-driven DNA transport across an artificial nanotopography, *New Journal of Physics* **11** (2009) 075032.

[107] J. Cho, S. Kumar, K. D. Dorfman, Electrophoretic collision of a DNA molecule with a small elliptical obstacle, *Electrophoresis* **31** (2010) 860–867.

[108] E. M. Sevick, D. R. M. Williams, Motion of a polyelectrolyte chain hooked around a post, *Physical Review E* **50** (1994) 3357–3360.

[109] E. Yarmola, P. P. Calabrese, A. Chrambach, G. H. Weiss, Interaction with the matrix: the dominant factor in macromolecular band spreading in gel electrophoresis, *Journal of Physical Chemistry B* **101** (1997) 2381–2387.

[110] G. Weiss, The two-state random walk, *Journal of Statistical Physics* **15** (1976) 157–165.

[111] G. Weiss, R. Rubin, Random walks: theory and selected applications, *Advances in Chemical Physics* **52** (1983) 363–505.

[112] S. P. Holleran, R. G. Larson, Multiple regimes of collision of an electrophoretically translating polymer chain against a thin post, *Macromolecules* **41** (2008) 5042–5054.

[113] J. J. Van Deemter, F. J. Zuiderweg, A. Klinkenberg, Longitudinal diffusion and resistance to mass transfer as causes of nonideality in chromatography, *Chemical Engineering Science* **5** (1956) 271–289.

[114] A. Mohan, P. S. Doyle, Unraveling of a tethered polymer chain in uniform solvent flow, *Macromolecules* **40** (2007) 4301–4312.

[115] F. Brochard-Wyart, Polymer chains under strong flows: stems and flowers, *Europhysics Letters* **30** (1995) 387.

[116] Y. C. Chan, M. Carles, N. J. Sucher, M. Wong, Y. Zohar, Design and fabrication of an integrated microsystem for microcapillary electrophoresis, *Journal of Micromechanics and Microengineering* **13** (2003) 914–921.

[117] G. B. Salieb-Beugelaar, K. D. Dorfman, A. van den Berg, J. C. T. Eijkel, Electrophoretic separation of DNA in gels and nanostructures, *Lab on a Chip* **9** (2009) 2508–2523.

[118] N. P. Teclemariam, V. A. Beck, E. S. G. Shaqfeh, S. J. Muller, Dynamics of DNA polymers in post arrays: Comparison of single molecule experiments and simulations, *Macromolecules* **40** (2007) 3848–3859.

[119] T. T. Perkins, D. E. Smith, R. G. Larson, S. Chu, Stretching of a single tethered polymer in a uniform flow, *Science* **268** (1995) 83–87.

[120] S. C. Jacobson, R. Hergenroder, L. B. Koutny, R. J. Warmack, J. M. Ramsey, Effects of Injection Schemes and Column Geometry on the Performance of Microchip Electrophoresis Devices, *Analytical Chemistry* **66** (1994) 1107–1113.

[121] R. C. Lo, V. M. Ugaz, Microchip DNA electrophoresis with automated whole-gel scanning detection, *Lab on a Chip* **8** (2008) 2135–2145.

[122] S. Landis, N. Chaix, C. Gourgon, C. Perret, T. Leveder, Stamp design effect on 100 nm feature size for 8 inch NanoImprint lithography, *Nanotechnology* **17** (2006) 2701–2709.

[123] A. Larsson, C. Carlsson, M. Jonsson, B. Albinsson, Characterization of the Binding of the Fluorescent Dyes YO and YOYO to DNA by Polarized Light Spectroscopy, *Journal of the American Chemical Society* **116** (1994) 8459–8465.

[124] R. S. Madabhushi, Separation of 4-color DNA sequencing extension products in noncovalently coated capillaries using low viscosity polymer solutions, *Electrophoresis* **19** (1998) 224–230.

[125] A. E. Nkodo, J. M. Garnier, B. Tinland, H. Ren, C. Desruisseaux, L. C. McCormick, G. Drouin, G. W. Slater, Diffusion coefficient of DNA molecules during free solution electrophoresis, *Electrophoresis* **22** (2001) 2424–2432.

[126] J. Mathé, J.-M. D. Meglio, B. Tinland, Electrophoretic separation of large DNAs using steric confinement, *Journal of Colloid and Interface*

Science **316** (2007) 831–835.

[127] N. C. Stellwagen, C. Gelfi, P. G. Righetti, The free solution mobility of DNA, *Biopolymers* **42** (1997) 687–703.

[128] E. Stellwagen, N. C. Stellwagen, Determining the electrophoretic mobility and translational diffusion coefficients of DNA molecules in free solution, *Electrophoresis* **23** (2002) 2794–2803.

[129] J. Billen, P. Gzil, N. Vervoort, G. V. Baron, G. Desmet, Influence of the packing heterogeneity on the performance of liquid chromatography supports, *Journal of Chromatography A* **1073** (2005) 53–61.

[130] M. DePra, W. T. Kok, J. G. E. Gardeniers, G. Desmet, S. Eeltink, J. W. van Nieuwasteele, P. J. Schoenmakers, Experimental Study on Band Dispersion in Channels Structured with Micropillars, *Analytical Chemistry* **78** (2006) 6519–6525.

[131] Y. Zeng, D. J. Harrison, Self-Assembled Colloidal Arrays as Three-Dimensional Nanofluidic Sieves for Separation of Biomolecules on Microchips, *Analytical Chemistry* **79** (2007) 2289–2295.

[132] N. Nazemifard, L. Wang, W. Ye, S. Bhattacharjee, J. H. Masliyah, D. J. Harrison, A systematic evaluation of the role of crystalline order in nanoporous materials on DNA separation, *Lab on a Chip* **12** (2012) 146–152.

[133] D. S. Malkin, B. Wei, A. J. Fogiel, S. L. Staats, M. J. Wirth, Submicrometer Plate Heights for Capillaries Packed with Silica Colloidal Crystals, *Analytical Chemistry* **82** (2010) 2175–2177.

Appendix A

Fabrication Protocols

This appendix discusses the steps used to build the devices used in this thesis. The experiments reported in chapter 3 were performed using a PDMS device. All other experiments were in oxidized silicon devices. Much of the fabrication work was accomplished in the University of Minnesota Nanofabrication Center.

A.1 PDMS Device

PDMS (polydimethylsiloxane) is a transparent elastomer commonly used in microfluidics research. It is delivered in two parts: the elastomer base and a curing agent. Once the two parts are mixed they will cure under the application of heat. The PDMS devices used here rely on a master mold containing the inverse geometry of the final device. PDMS is then poured over the master, cured, and packaged into a final device. The master can be used for multiple molds. The final PDMS device is relatively inexpensive.

Photoresist Mold Fabrication

1) Piranha clean 4 inch silicon wafer. Piranha is sulfuric acid and hydrogen peroxide heated to 120 °C (its boiling temperature). Leave wafer in this solution 15 to 20 minutes.

2) Rinse wafer with DI water. Use 3 cycles on the wet bench dump rinser and the rinser on the spin dryer. Ensure the wafer is dry by heating on a hot plate for 60 sec.

3) HMDS vapor treatment. This vapor increases photoresist adhesion. 3-5 minutes.

4) Spin coat photoresist. This should give a thin, uniform layer on the wafer. Choose the photoresist type and spin speed based on the thickness of the mold you want. For example, S1818 at 3000 RPM and 30 sec gives approximately 1.8 micron thick layer.

5) Soft bake. Use 105°C, 60 sec for Shipley series photoresists. This step removes the solvent from the photoresist. Different photoresists require different soft bake parameters.

6) Exposure. Transfer a pattern from a mask to the wafer by exposing the photoresist to change its solubility in photoresist developer. The best pattern transfer comes from using the exposure program 'Lo Vac' on the MA6 or MABA6 aligner. The exposure time must be tuned to account for the photoresist thickness and the intensity of the bulb in the mask aligner. For example, S1805 exposure times vary from 1.8 to 2.1 seconds. Under-exposed or over-exposed wafers are only apparent after developing.

7) Post Exposure Bake. Use 115°C, 60 sec for Shipley series photoresists. Cool wafer before developing.

8) Developing. Microposit 351 developer dissolves exposed Shipley series photoresists. This developer can be diluted with water to increase the devel-

oping time. The wafer is developed once all exposed photoresist is dissolved. This is best determined by watching any large exposed areas on the wafer. Developing time must be tuned based on the photoresist thickness, exposure dose, and developer reactivity. After developing, immediately rinse the wafer with DI water to stop developing.

9) Hard Bake. Use 120°C, 60 sec for Shipley series photoresists. Photoresist is very difficult to remove after a hard bake.

10) Silanization. Place a few drops of tridecafluoro-1,1,2,2-tetrahydrooctyl)-1-trichlorosilane in a medicine cup inside a vacuum chamber with the wafer master. Apply vacuum forcing the silane into the vapor phase. Allow the silane vapor to coat the master wafer for 60 to 90 minutes.

Silicon Mold Fabrication

1) Transfer pattern to photoresist. Perform steps 1-9 in the **Photoresist Mold Fabrication** section.

2) Reactive Ion Etch. 'fastpoly.set' on the STS etcher uses sulfur hexafluoride (SF_6) ions to selectively etch silicon. Any bare areas of the wafer will be etched. This etching method can be transport limited. In this case, large open areas with no photoresist will etch faster than small holes or narrow lines. The resulting etch may not be to a uniform depth. Measure depth using P16 profilometer or an AFM.

3) Photoresist Removal. Rinse wafer with chemicals in the following order: Acetone, Methanol, Iso-Propanol, Water. Any residual photoresist should be removed by oxygen plasma or by a piranha clean.

4) Silanization. Place a few drops of tridecafluoro-1,1,2,2-tetrahydrooctyl)-1-trichlorosilane in a medicine cup inside a vacuum chamber with the wafer master. Apply vacuum, forcing the silane into the vapor phase. Allow the

silane vapor to coat the master wafer for 60 to 90 minutes.

PDMS Molding

1) Mix. For clear PDMS (Sylgard 184), thoroughly mix 1 part curing agent with 10 parts base. For h-PDMS (Sylgard 170) mix equal parts of both parts.

2) Degas. Place under vacuum until all bubbles are gone (∼45 minutes).

3) Pour. Pour on mold. The PDMS will flow off of the mold. Any air bubbles should be removed by placing under vacuum again.

4) Cure. Recommend elevated temperature (50°C to 70°C) overnight. PDMS will partially cure overnight at room temperature requiring ∼30 minutes at elevated temperature to fully cure.

5) Device Assembly. PDMS can be cut with a razor blade or hobby knife. Punch reservoirs into the PDMS using a sharpened metal tube. Large reservoir areas can collapse, so punch the reservoirs so that they intersect with the microfluidic channel. Dust-free PDMS will conformally bond to any flat surface giving a water-tight, reversible seal. PDMS can be permanently bonded to silicon or glass by oxygen plasma treatment of the PDMS prior to bring the silicon/glass into contact with the PDMS. Oxygen plasma treatment causes nano-fissures on the PDMS surface.

6) Fill Device with Fluid. Fill one reservoir at a time, allowing air to escape through unfilled reservoirs. Filling with ethanol is sometimes more effective than filling with DI water; however, ethanol must be completely removed from the device before performing electrophoresis experiments. Placing the entire device under vacuum increases air transport through the filling fluid and out of the device.

A.2 Oxidized Silicon Device

An alternative to using PDMS devices is to build the device in silicon. Because of the conductive nature of silicon, the device must be coated with an insulating layer to prevent electron transport through the device itself. We found oxidizing the surface of the silicon to be effective, although silicon nitride should work as well. See figure 6.2 for a schematic of the fabrication process.

1) Transfer pattern to photoresist. Perform steps 1-9 in the **Photoresist Mold Fabrication** section. The exposure step described above is for the MA6/MABA6 mask aligners where the transfered pattern is the same size as the mask. The NFC has a projection lithography system (Canon Stepper) that transfers the pattern of the mask to the wafer shrunk by 5 times. Masks for use in the Canon Stepper require alignment marks that must be added to the mask design. The Canon Stepper is designed for the SPR 995 series of photoresists. The typical smallest feature on the MA6/MABA6 is 1 μm while on the Canon Stepper it is 500 nm.

2) Reactive Ion Etch. 'fastpoly.set' on the STS etcher uses sulfur hexafluoride (SF_6) ions to selectively etch silicon. Any bare areas of the wafer will be etched. This etching method can be transport limited. In this case, large open areas with no photoresist will etch faster than small holes or narrow lines. The resulting etch may not be to a uniform depth. Measure depth using P16 profilometer or an AFM.

The deep trench etcher uses a Bosch process for high aspect ratio etching with perpendicular side walls. These times vary with the masking material and from day-to-day. There are two types of recipes: continuous time recipes and looped recipes. Continuous time recipes may be stopped at any time. Looped recipes must be stopped after a discrete number of loops. Approximate etch depths are: '6Watt', 18 loops = 11.6 μm; '6Watt', 20 loops = 12.7 μm;

'shallow', 10 loops = 1.8 μm; 'shallow', 15 loops = 2.9 μm.

3) Photoresist Removal. Rinse wafer with chemicals in the following order: Acetone, Methanol, Iso-Propanol, Water. Any residual photoresist should be removed by oxygen plasma or by a piranha clean.

4) Nitride Coating. Coat both sides of the wafer with a silicon nitride layer which will act as a mask during KOH etching. Piranha clean the wafers and rinse with DI water. Place in low pressure chemical vapor deposition (LPCVD) tube for low stress nitride deposition. Running the recipe 'LSN-31' for 80 minutes results in a ∼200 nm thick nitride layer. Layer thickness was measured by ellipsometry.

5) KOH Etching. Potassium hydroxide (KOH) selectively etches the 100 crystal plane of silicon. This is a wet etch in ∼30% KOH at elevated temperature (60°C to 90°C) to etch fluid reservoirs through the wafer. Remove the nitride masking layer from the reservoir using a scratch pen. Only the outline of the reservoirs needs to be removed. I found it easiest to draw a rectangle in the reservoir. The KOH etch leaves a hole with sidewalls at a 55°angle.

6) Nitride Removal. Remove the nitride masking layer in 85% Phosphoric Acid (H_3PO_4) at 265°C. When the nitride layer is only a few nanometers thick, it does not alter the color of the silicon wafer. Silicon nitride is more hydrophilic than bare silicon, and the hydrophobicity of the surface can be used to determine when the nitride layer has been completely removed. The removal of a 200 nm nitride layer takes several hours.

7) Oxidation. KOH etched wafers are not allowed to be processed in the Tylan oxidation tubes. We are allowed to grow an oxide layer in the Mini-Brute tube in NFC area 1. Use an O_2 flow rate of 2 L/min; temperature of 1100°C; time at temperature of 5 to 6 hours resulting in a 250 nm to 300 nm silicon oxide layer. Place the wafers in the tube under N_2 gas, then ramp

up the temperature for $\sim$ 90 minutes. Once at the running temperature is reached, switch the gas line to O_2 for 5 to 6 hours. After the run is completed, switch back to N_2 and power down the heater. There is no cooling on the Mini-Brute, so it takes several hours to return to room temperature.

8) SEM characterization. This is not always required as light microscopy may provide enough detail. However, the scanning electron microscope cannot penetrate glass, so finish all SEM imaging before bonding the wafer irreversibly.

9) Anodic Bonding. Wafer cleanliness is important for bonding. The thickness of the glass plate is determined by the application of the device. 500 μm thick glass is easy to work with, but is too thick for imaging with the oil immersion objectives in the Dorfman lab. 100 μm and 200 μm thick glass is more delicate and more expensive, but allows imaging with the oil immersion objectives. The SB6 wafer bonder processes whole 4 inch wafers only. 'anodvac_1800' applies a potential of 1800 V across the glass and silicon wafer. This high electric potential is believed to cause ions in the glass to migrate to the glass-oxidized silicon interface and form covalent bonds across the two materials resulting in an irreversible bond. Because the ions in the glass are necessary, the glass should be BOROFLOAT or Pyrex (same material, different manufacturers).

10) Wafer Dicing. Wafers can be precisely diced with the NFC wafer saw. Alternatively, you can crack the wafer into individual devices along a crystal plane. Crystal planes run parallel and perpendicular to the wafer flat. Score the wafer with a scratch pen along the crystal plane, then slowly apply pressure until the wafer cracks.

11) Device Assembly. We have to add large fluid reservoirs to the device. This has been accomplished in two ways: (i) polycarbonate chip holders; and (ii) Upchurch fluidic reservoirs. The polycarbonate chip holders were built by the ME machine shop according to our drawings. The device is

clamped between a bottom support plate and a top plate which provides fluid reservoirs. The fluid reservoirs are designed to attach to a syringe pump.

Usually there is a drilled glass microscope slide between the device and the Upchurch reservoirs; while this makes handling the device easier, it is not necessary. We have used both the optical adhesive NOA 81 and epoxy to attach the glass slides and plastic reservoirs. NOA 81 is applied to the surfaces, then quickly cured by exposure to UV light. NOA 81 reaches full bonding strength after several hours at elevated temperature. NOA 81 can be dissolved by Methylene Dichloride (Dichloromethane), and thus allows us to reuse the reservoirs and devices. However, once the NOA 81 gets into the microfluidic channels I have never been able to remove it. Epoxy is not as easily dissolved, but it is much more viscous. Its increased viscosity prevents it from flowing into the microfluidic channels.

A.3 Filling the Device with Fluid

Microfluidic devices have large surface area and can generate large capillary forces. However, filling a device with fluid is not always easy. Here are some tips and tricks that should get the job done.

Ethanol is less viscous than water, and we have seen that it more easily wets our devices. After wetting with ethanol, be sure to completely flush it from the device before performing any experiments.

Air bubbles are common after the chip is mostly filled. To prevent air bubbles from forming, degas the filling fluid prior to device filling. PDMS is permeable to air. You can degas PDMS before filling with fluid; this will allow the PDMS layer to absorb air bubbles. If air bubbles persist, it is helpful to store the device under vacuum overnight.

After filling the device with fluid, do not let it dry. Store the device under DI water, or under the running buffer.